Measurement of the p(e, e' π+)n reaction with the short-orbit spectrometer at Q2 = 0.078 (GeV/c)2

Friščić, Ivica

Doctoral thesis / Disertacija

2015

Degree Grantor / Ustanova koja je dodijelila akademski / stručni stupanj: **University of Zagreb, Faculty of Science / Sveučilište u Zagrebu, Prirodoslovno-matematički fakultet**

Permanent link / Trajna poveznica: https://urn.nsk.hr/urn:nbn:hr:217:476141

Rights / Prava: In copyright/Zaštićeno autorskim pravom.

Download date / Datum preuzimanja: **2024-07-16**

University of Zagreb
Faculty of Science
Department of Physics

Ivica Friščić

MEASUREMENT OF THE $p(e,e'\pi^{+})n$ REACTION WITH THE SHORT-ORBIT SPECTROMETER AT $Q^2 = 0.078$ (GeV/c)^2

DOCTORAL THESIS

Zagreb, 2015

University of Zagreb
Faculty of Science
Department of Physics

Ivica Friščić

MEASUREMENT OF THE p(e,e′π^+)n REACTION WITH THE SHORT-ORBIT SPECTROMETER AT Q^2 = 0.078 (GeV/c)^2

DOCTORAL THESIS

Supervisor: Prof. dr. sc. Damir Bosnar

Zagreb, 2015

Sveučilište u Zagrebu
Prirodoslovno-matematički fakultet
Fizički odsjek

Ivica Friščić

MJERENJE REAKCIJE p(e,e′π⁺)n SPEKTROMETROM KRATKE ORBITE NA Q² = 0.078 (GeV/c)²

DOKTORSKI RAD

Mentor: prof. dr. sc. Damir Bosnar

Zagreb, 2015

BASIC DOCUMENTATION CARD

Measurement of the $p(e, e'\pi^+)n$ reaction with the short-orbit spectrometer at $Q^2 = 0.078$ (GeV/c)^2

Ivica Friščić

Faculty of Science, Zagreb

The precise measurement of the cross section for the $p(e, e'\pi^+)n$ reaction at certain kinematics, allows one to separate the cross section into quantities at a given four-momentum transfer Q^2, which carry the information about the nucleon structure. Since the data at low Q^2 are not known with an intended precision, a new measurement of the $p(e, e'\pi^+)n$ reaction was performed at $Q^2 = 0.078$ (GeV/c)^2 and at an invariant mass of $W = 1094$ MeV - approximately 15 MeV above the reaction threshold. The experimental work was accomplished by the A1 collaboration at the Institute for Nuclear Physics at the Johannes Gutenberg University of Mainz, Germany. The high quality electron beam was provided by the MAMI B accelerator with the energy range from 180 to 855 MeV. The produced charged pion was detected in the short-orbit spectrometer (SOS), which was constructed for a detection of the low-energy pions. The scattered electron was detected in the standard spectrometer A. For the first time, the complete analysis of the $p(e, e'\pi^+)n$ reaction data measured with the SOS was performed. New SOS-specific correction methods were developed to ensure a consistent data analysis. Some of the most important methods are the procedure of pion decay correction, the simulation for the determination of the muon contamination in the SOS data. The measurement was done and the analysis was carried out for five different kinematical settings. The relative total errors of the obtained $p(e, e'\pi^+)n$ cross sections were between 3.1% and 3.7%. Three cross sections were measured in a parallel kinematics at the virtual photon polarizations $\epsilon = 0.897$, 0.591 and 0.306. In case of the parallel kinematics only the transverse and the longitudinal terms appear in the measured cross section. These terms were separated using the Rosenbluth method. For the highest $\epsilon = 0.897$ value two measurements were performed with the SOS offsets

at $+18.7°$ and $-18.7°$ (in the centre-of-mass frame), or in other words to the left and to the right from the parallel kinematics direction of the pion. In this way it was possible to determine the transversal-longitudinal interference term of the cross section. The relative total errors of the transverse, the longitudinal and the interference term were 6.7%, 14.7% and 10.5%, respectively. The results for the cross section terms, which contain the information about the nucleon structure, were compared with predictions of the selected theoretical models.

Mjerenje reakcije $p(e, e'\pi^+)n$ spektrometrom kratke orbite na $Q^2 = 0.078(\text{GeV/c})^2$

Ivica Friščić

Prirodoslovno-matematički fakultet, Zagreb

Precizno mjerenje udarnog presjeka reakcije $p(e,e'\pi^+)n$ na pažljivo biranim kinematikama, omogućava nam, da na danom prijenosu četveroimpulsa Q^2, udarni presjek možemo separirati na veličine, koje u sebi nose informacije o strukturi nukleona. Kako na niskim vrijednostima Q^2 nema podataka zadovoljavajuće preciznosti, napravljeno je novo mjerenje $p(e,e'\pi^+)n$ reakcije na $Q^2 = 0.078$ (GeV/c)^2 i na invarijantnoj masi $W = 1094$ MeV – otprilike 15 MeV iznad praga reakcije. Eksperiment je proveden u okviru A1 kolaboracije na Institutu za nuklearnu fiziku Johannes Gutenberg Sveučilišta u Mainzu, Njemačka. Visoko kvalitetni snop elektrona davao je MAMI B akcelerator koji omogućava energije u rasponu od 180 do 855 MeV. Producirani nabijeni pion detektiran je u spektrometru kratke orbite (SOS), koji je specijaliziran za detekciju niskoenergijskih piona. Raspršeni elektron detektiran je u standardnom spektrometru A. Po prvi puta napravljena je kompletna analiza podataka mjerenja $p(e,e'\pi^+)n$ reakcije koji su dobiveni koristeći SOS. Kako bi analiza bila valjana, razvijene su nove korekcijske metode specifične za SOS. Neke od najvažnijih metoda su postupak za određivanje korekcije zbog raspada piona, simulacija za određivanje mionske kontaminacije u SOS-ovim podacima itd. Analiza je provedena za pet različitih kinematika. Relativne ukupne greške dobivenih udarnih presjeka $p(e,e'\pi^+)n$ reakcije bile su između 3.1% i 3.7%. Tri udarna presjeka mjerena su u paralelnoj kinematici za iznose polarizacije virtualnog fotona $\epsilon = 0.897, 0.591$ i 0.306. U slučaju paralelne kinematike u mjerenom udarnom presjeku pojavljuju se samo transverzalni i longitudinalni članovi. Njih smo izdvojili pomoću Rosenbluth-ove metode. Za najveću $\epsilon = 0.897$ vrijednost napravljena su dva mjerenja za pomake SOS-a od $+18.7°$ i $-18.7°$ (u

sustav centra mase), ili drugim riječima lijevo i desno u odnosu na smjer piona u paralelnoj kinematici. Na taj je način bilo moguće odrediti transverzalno-longitudinalni interferencijski član udarnog presjeka. Relativne ukupne greške transverzalnog, longitudinalnog i interferencijskog člana iznosile su redom 6.7%, 14.7% i 10.5%. Sami članovi udarnog presjeka sadrže informaciju o strukturi nukleona, stoga su dobiveni rezultati uspoređeni sa predviđanjima odabranih teorijskih modela.

Ključne riječi: elektroprodukcija nabijenih piona, magnetski spektrometar, SOS, raspad piona, mionska kontaminacija, udarni presjek

(134 stranica, 53 literaturnih navoda, 54 slika, 18 tablica, izvornik na engleskom jeziku)

Mentor: prof. dr. sc. Damir Bosnar, Sveučilište u Zagrebu

Povjerenstvo za obranu:

1. izv. prof. dr. sc. Matko Milin, Sveučilište u Zagrebu
2. izv. prof. dr. sc. Tamara Nikšić, Sveučilište u Zagrebu
3. dr. sc. Neven Soić, znanstveni savjetnik, Institut Ruđer Bošković, Zagreb
4. dr. sc. Ulrich Müller, viši znanstveni suradnik, Johannes Gutenberg Sveučilište u Mainzu, Njemačka
5. prof. dr. sc. Damir Bosnar, Sveučilište u Zagrebu

Rad prihvaćen: 2015

This work is dedicated to
my parents Marija and Vjekoslav,
for their 50th marriage anniversary.

Acknowledgments

Table of Contents

1

Introduction

During the last several decades a great progress has been made in understanding of the structure of the nucleon, but some quantities, essential to describe the structure of the nucleon, are still not known with an intended precision. The nucleon is an extended object and has a composite structure. Most of the high precision data about the nucleon size and its structure was obtained from the electron scattering experiments. At the low four-momentum transfer Q^2, the interaction of the electron and the target nucleon can be approximated with an exchange of one virtual photon. Since this interaction is purely electromagnetic, it is simple and very well-known in terms of the quantum electrodynamics (QED). The energy and the momentum of the virtual photon can be varied independently and they are well-defined by the energy and momentum of the incident and scattered electron. For a fixed energy and only varying the momentum of the virtual photon it is possible to map out the so-called form factors. In the Breit frame, fixed by the zero-energy transfer to the nucleon, the form factors (at low Q^2) can be interpreted as the three-dimensional Fourier transform of the charge, current and transition densities. The inverse Fourier transforms of the form factors then give the spatial distributions of those densities inside a nucleon [1, 2].

In a precise measurement of the cross section for the charged pion electroproduction on protons $(p(e, e'\pi^+)n)$ near threshold one part of the nucleon structure is getting accessible. Since the state of the initial nucleon is changed by an emission of the charged pion, this process is sensitive to the weak axial vector part of the nucleon structure and corresponding form factors: the axial form factor and the induced pseudoscalar form factor [3]. The axial form factor is related to the spin-isospin distribution of the nucleon [4] and the induced pseudoscalar form factor is related to the pion pole.

The virtual photon carries both a transversal ϵ and a longitudinal $\epsilon_L^\star$ polarization. That results in an appearance of the transversal T, longitudinal L and different interference terms (TL and TT) in a cross section which describes the interaction of the virtual

photons with the target proton. In case of an unpolarized electron beam and target this cross section can be factorized as [5, 6]:

$$\frac{d\sigma_\nu}{d\Omega_\pi^\star} = \frac{d\sigma_T}{d\Omega_\pi^\star} + \epsilon_L^\star \frac{d\sigma_L}{d\Omega_\pi^\star} + \sqrt{2\epsilon_L^\star(1+\epsilon)}\frac{d\sigma_{TL}}{d\Omega_\pi^\star}\cos\phi_\pi + \epsilon\frac{d\sigma_{TT}}{d\Omega_\pi^\star}\cos 2\phi_\pi \qquad (1.1)$$

where $\phi_\pi = \phi_\pi^\star$ is the angle between the plane defined by momenta of the incoming and the outgoing electron and the plane defined by the virtual photon and pion momenta, "$\star$" denotes quantities evaluated in the centre-of-mass frame. The most important terms related to the nucleon structure are the T and the L terms. The T term is only sensitive to the axial form factor and the L term contains the induced pseudoscalar form factor as one of the contributions.

The T and the L cross section terms can be experimentally separated. The measurement has to be performed in the so-called parallel kinematics, in which the produced pion is detected in a direction of the virtual photon (the pion production angle $\theta_\pi = \theta_\pi^\star = 0°$). Since the interference terms have an explicit dependence in form of $d\sigma_{TL} \sim sin\theta_\pi^*$ and $d\sigma_{TT} \sim sin^2\theta_\pi^\star$, they vanish in the parallel kinematics and the cross section now contains only the T and the L terms [5, 6]. The idea is to repeat the cross section measurement for the fixed values of the invariant mass W and four-momentum transfer Q^2, and only vary the virtual photon polarization ϵ ($\epsilon_L^\star$), which can be accurately controlled by means of the electron kinematics. The T and the L terms now act as coefficients in the equation of a straight line, which can be easily determined via straight-line fit. This procedure is also known as the Rosenbluth separation [7].

It is also relatively easy to experimentally separate the TL interference term. Two measurements of the cross section at fixed values of W, Q^2 and ϵ are needed. One measurement has to be performed at $\theta_\pi^\star \neq 0$ and $\phi_\pi = 0°$, and the other measurement for the same $\theta_\pi^\star$ angle, but $\phi_\pi = 180°$ (the plane defined by the virtual photon and the pion momenta is flipped upside-down), or it is custom to say that measurements have to be performed to the left and to the right for the same pion angle with respect to the virtual photon direction [6]. In those two kinematical situations the T, L and TT terms have same values, which cancel out when subtracting the measured left and right cross section and the TL term can be extracted from this difference.

Knowing the precise values of the experimental T, L and TL cross section terms at given W and Q^2 allows one to test theoretical predictions of these quantities, which are based on various models of the nucleon structure.

First measurements of the charged pion electroproduction near threshold and the separation of the T and L cross section terms in a subsequent data analysis started during the seventies of the last century in Frascati, Saclay, Hamburg (DESY), Daresbury, Kharkov (see [5] and related references). The obtained data was used to extract the ax-

ial form factor from the Q^2-dependence of the T term (the procedure will be described in the next chapter). The problem with these results was that they were accompanied by large statistical and systematic errors.

A series of recent experiments have been carried out in the framework of A1 collaboration, using the Mainz Microtron (MAMI) electron accelerator, at the Institute for Nuclear Physics at the Johannes Gutenberg University of Mainz, Germany. Measurements of the cross section for the positive pion-on-proton electroproduction were performed at the invariant mass of $W = 1125$ MeV, which is approximately 46 MeV above the threshold for the production of charged pions, at the four-momentum transfer of $Q^2 = 0.117$ (GeV/c)^2 [8, 9], $Q^2 = 0.195$ (GeV/c)^2, and $Q^2 = 0.273$ (GeV/c)^2 [10, 11]. Statistical uncertainties of the measured cross section in the $p(e, e'\pi^+)n$ reaction were between 0.7% and 2.3%, the corresponding systematic uncertainties were between 1.6% and 3.7% [11]. The Rosenbluth separation was done for each Q^2-point, thus allowing the extraction of the axial form factor. The measurement at $Q^2 = 0.058$ (GeV/c)^2 was later performed [12], with an aim of studying the behavior of the T and L cross section terms at the lower four-momentum transfer.

Since a measurement closer to the $p(e, e'\pi^+)n$ reaction threshold ($W = 1079.14$ MeV) would allow an access to even lower four-momentum transfers, in this thesis we present the measurement and the analysis of the $p(e, e'\pi^+)n$ coincidence experiment only $\simeq 15$ MeV above the threshold. The experiment was performed by the A1 Collaboration using the continuous electron beam provided by MAMI at the Institute for Nuclear Physics, University of Mainz. The scattered electron was detected in spectrometer A, while the produced pion was detected in the short-orbit spectrometer (SOS). The invariant mass W was fixed at 1094 MeV and the virtual photon four-momentum transfer Q^2 at 0.078 (GeV/c)^2. In total, measurement of five different kinematical settings was performed. Three of them, with the virtual photon polarization values of $\epsilon = 0.897$, 0.591 and 0.306, were measured in the parallel kinematics in order to separate the T and the L cross section terms via Rosenbluth separation. In the last two measurements at $\epsilon = 0.897$, the pion was detected at $-18.7°$ and $+18.7°$ (in the centre-of-mass frame) offset from the parallel kinematics. In this way it was possible to determine the TL interference term of the cross section.

Detecting the low-energy pions is an experimental challenge. Pions are unstable particles decaying dominantly to a muon and a muon neutrino, with a lifetime of 26.033 ns [13]. The lengths of particle trajectories in each of three standard spectrometers of A1 collaboration are in the order of 10 m and approaching the reaction threshold, due to the pion decay, the number of pions passing through the detector package is reduced and to obtain an acceptable statistical error the measurement time has to be increased. At the same time, a fraction of muons, which are created in direction of

pions is increased. Such muons will be also detected and they can not be distinguished from the pions, causing an increase of the systematic error of the measurement. The muon contamination has to be determined via simulation. The SOS was built to overcome these problems, providing the particle flight path of approximately 1.6 m from the target to the detector package. The design, assembling and calibration of the SOS detector system was done in the framework of the diploma and doctoral thesis of Dagmar Baumann [12, 14] and Matthias Ding [15, 16]. Taking into account the new value of the flight path the fraction of the detected pions is greatly increased, while the muon contamination is significantly reduced.

Prior to this thesis, the analysis of the data obtained from the measurement of the $p(e, e'\pi^+)n$ reaction with SOS was never performed. Therefore, a big effort was invested to develop different correction methods needed for a consistent data analysis, such as the determination of the SOS drift chamber efficiencies, calculation of the pion decay correction and the development of the Monte Carlo simulation for the estimation of a muon contamination in the SOS data. Using the new-developed correction methods the $p(e, e'\pi^+)n$ cross section was determined for all five kinematical settings, subsequently the physical goal of this thesis was fulfilled by extracting the values of the T, L and TL cross section terms at $W = 1094$ MeV and $Q^2 = 0.078$ (GeV/c)^2.

The thesis is divided into 7 chapters. In chapter 2 the underlying theoretical formalism of the charged pion electroproduction will be briefly explained. The definition of the differential cross section, electromagnetic and weak form factors will be given, as well as methods for extracting of these quantities from the experimental data. In chapter 3 the electron accelerator MAMI and the standard three spectrometer setup of the A1 collaboration will be described. The SOS will be described in a separate chapter 4. This spectrometer is not part of the standard setup – it was build especially for the detection of the low-energy pions. The performed experiment and the selected kinematical settings will be presented in chapter 5. All steps of the analysis will be discussed in detail in chapter 6. The thesis ends with chapter 7, where the experimental results are presented and compared with predictions of the selected models, and finally at the end an outlook for the further research and data analysis improvements is given.

2

Theoretical Background

In the following chapter an introduction into the theory of the unpolarized electron scattering on nucleon will be presented. Particular emphasis will be given to charged pion production and to kinematic conditions under which particular quantities of the nucleon weak interaction can be experimentally accessed.

2.1 Pion electroproduction kinematics

The kinematical variables of the charged pion electroproduction on nucleons are presented on Fig. 2.1. The motion of each particle in a reaction is completely described by a four-momentum (energy E, momentum $\vec{p}$). The reaction of the charged pion electro-
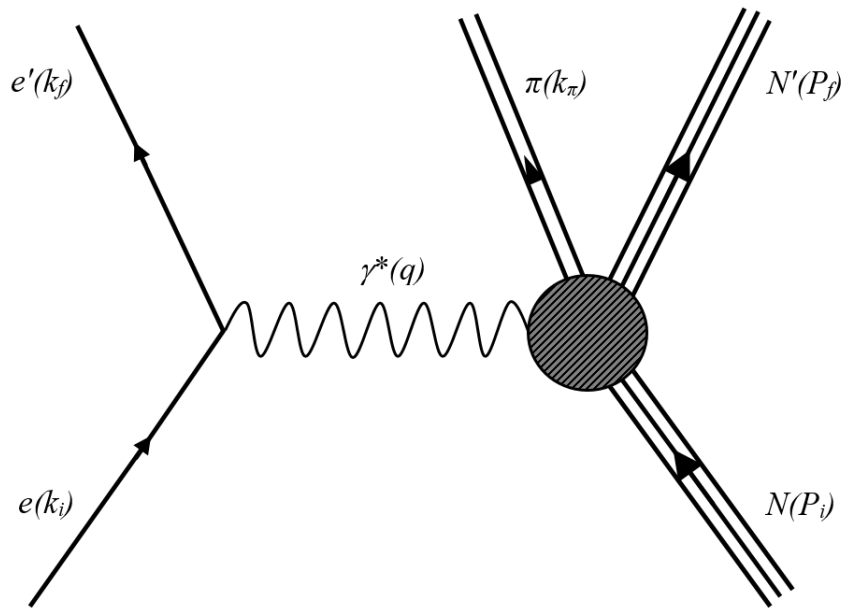
Figure 2.1 — Reaction of the charged pion electroproduction on nucleon in the plane-wave Born approximation of one photon exchange.

production on nucleon can be written as:

$$e(k_i) + N(P_i) \rightarrow e'(k_f) + N'(P_f) + \pi(k_\pi) \tag{2.1}$$

where $P_i = (E_i, \vec{P}_i)$ and $P_f = (E_f, \vec{P}_f)$ are four-momenta of the initial and of the final nucleon, $k_i = (\epsilon_i, \vec{k}_i)$ and $k_f = (\epsilon_f, \vec{k}_f)$ of the incident and of the scattered electron, and $k_\pi = (\omega_\pi, \vec{k}_\pi)$ is the four-momentum of the produced charged pion. The electron-nucleon interaction is purely electromagnetic. The coupling constant ($\alpha = e^2/(4\pi) \approx 1/137$) is small, allowing the description of the process in the so-called one photon exchange approximation (Fig. 2.1). In this approximation, the four-momentum of exchanged photon $q = (\omega, \vec{q})$ is well defined by four-momenta of the incident and of the scattered electron $q = k_i - k_f$. Therefore, the pion electroproduction can be further simplified to:

$$\gamma^*(q) + N(P_i) \rightarrow N'(P_f) + \pi(k_\pi) \tag{2.2}$$

where γ^* refers to a virtual photon. Having $q^2 < 0$ for the virtual photon ($q^2 = 0$ for real photon), it is common to introduce a positive scalar $Q^2 = -q^2$.

The above statements are valid for charged pion electroproduction both on protons and on neutrons, but experimentally it is more convenient to measure positively charged pion electroproduction on proton (free neutron is unstable), i. e. from now on we consider the $p(e, e'\pi^+)n$ reaction or in terms of one photon exchange $p(\gamma^*, \pi^+)n$. In the laboratory frame, scattering occurs on a stationary proton and the proton four-momentum is $P_i = (m_p, \vec{0})$, where $m_p = 938.27$ MeV/c^2 is the proton mass. The four-momentum of the produced neutron P_f is not detected, but can be derived from the energy and momentum conservation laws. The threshold energy for this reaction equals to the masses' sum of reaction products: $m_n c^2 + m_\pi c^2 = 1079.14$ MeV. The Mandelstam variables are defined as [17]:

$$s = W^2 = (P_i + q)^2 = (P_f + k_\pi)^2$$
$$t = (q - k_\pi)^2 = (P_i + P_f)^2 \tag{2.3}$$
$$u = (P_f - q)^2 = (P_i - k_\pi)^2$$

and they fulfill:

$$s + t + u = q^2 + m_p^2 + m_n^2 + m_\pi^2 = 2m_p^2 + m_\pi^2 - Q^2 \tag{2.4}$$

Neglecting the electron mass, the total energy in the centre-of-mass frame of the pion neutron system W and four-momentum transfer Q^2 are:

$$W^2 = (P_i + q)^2 = m_p^2 - Q^2 + 2m_p\omega$$
$$Q^2 = -q^2 = 4\epsilon_i\epsilon_f \sin^2\frac{\theta_e}{2} \tag{2.5}$$

Fig. 2.2 illustrates used spatial coordinate systems. The scattering plain is defined by momenta vectors of the incident and of the scattered electron, $\vec{k}_i$ and $\vec{k}_f$ respectively. The pion momentum vector $\vec{k}_\pi$ and the virtual photon momentum vector $\vec{q}$ define the reaction plane.
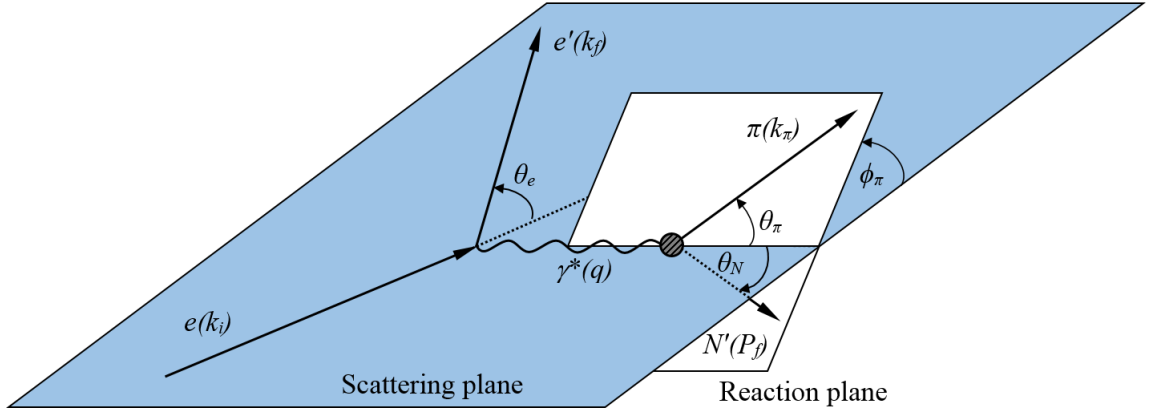
Figure 2.2 — Definition of spatial variables used for describing the $p(e, e'\pi^+)n$ reaction.

By varying quantities in the laboratory frame: electron scattering angle θ_e, incident electron energy ϵ_i and scattered electron energy ϵ_f; it is possible to set W and Q^2 to a wanted combination. The exchanged virtual photon can be polarized transversally as well as longitudinally. The transversal polarization is described by polarization parameter ϵ:

$$\epsilon = \left(1 + \frac{2|\vec{q}|^2}{q^2} \tan^2 \frac{\theta_e}{2}\right)^{-1} \tag{2.6}$$

ϵ can be set by choosing appropriate electron scattering angle θ_e. The range of ϵ values lies between 0 for backscattering and 1 for forward-scattering. The longitudinal polarization parameter $\epsilon_L^\star$ can be also expressed as:

$$\epsilon_L^\star = \frac{Q^2}{\omega^{\star 2}} \epsilon \tag{2.7}$$

2.2 Cross section

The differential cross section of exclusive π^+-electroproduction in one photon exchange, with phase space expressed in the laboratory frame, can be written as [6]:

$$d\sigma = \frac{\epsilon_i}{|\vec{k}_i|} \frac{m_e}{\epsilon_i} \frac{m_i}{E_i} \frac{m_e}{\epsilon_f} \frac{d^3k_f}{(2\pi)^3} \frac{1}{2\omega_\pi} \frac{d^3k_\pi}{(2\pi)^3} \frac{m_f}{E_f} \frac{d^3P_f}{(2\pi)^3} (2\pi)^4 \delta^{(4)}(P_i + q - k_\pi - P_f)$$
$$\times |\langle P_f, k_\pi| J^\mu |P_i\rangle q^{-2} \langle k_f| j_\mu |k_i\rangle|^2 \tag{2.8}$$

As mentioned above, the interaction of the electron-nucleon system is purely electromagnetic and the structure of this process can be described by the electron current j_μ and the current of the hadronic system J^μ. The square of the transition matrix elements can be represented as a product of the leptonic tensor $\eta_{\mu\nu}$ and the hadronic tensor $W_{\mu\nu}$, which are both second order Lorentz-tensors:

$$| \langle P_f, k_\pi | J^\mu | P_i \rangle q^{-2} \langle k_f | j_\mu | k_i \rangle |^2 = W_{\mu\nu} \eta^{\mu\nu} \tag{2.9}$$

The leptonic tensor describes the electron vertex and it can be written as:

$$\eta_{\mu\nu} = \sum_{s_f} (\bar{u}(k_f, s_f) e \gamma_\mu u(k_i, s_i))(\bar{u}(k_f, s_f) e \gamma_\mu u(k_i, s_i))^*$$
$$= \frac{e^2}{2m_e^2}(2K_\mu K_\nu + \frac{1}{2}q^2 g_{\mu\nu} - \frac{1}{2}g_\mu g_\nu + ih\epsilon_{\mu\nu\alpha\beta}q^\alpha K^\beta) \tag{2.10}$$

whereby $K = \frac{1}{2}(k_i + k_f)$, $h = \vec{\sigma} \cdot \hat{k}_i = \pm 1$ is the helicity of an incident electron, $g_{\mu\nu}$ is the metric tensor and $\epsilon_{\mu\nu\alpha\beta}$ is the totally antisymmetric tensor ($\epsilon_{0123} = 1$). The definition of the hadronic tensor is:

$$W_{\mu\nu} = (\frac{m}{4\pi W})^2 \langle \chi_f | J_\mu | \chi_i \rangle \langle \chi_f | J_\nu | \chi_i \rangle^* \tag{2.11}$$

where $|\chi_i\rangle$ and $|\chi_f\rangle$ are nucleon spinors in the initial and the final states. $J^\mu = (\rho, \vec{J})$ is a transition current operator between the hadronic initial and the final states. Using CGLN (Chew, Goldberger, Low, Nambu) amplitudes $F_i (i = 1, ..., 8)$ and substitutions $\widetilde{\sigma} = \vec{\sigma} - (\vec{\sigma} \cdot \hat{q})\hat{q}$ and $\widetilde{k}_\pi = \vec{k}_\pi - (\vec{k}_\pi \cdot \hat{q})\hat{q}$, components of the transition current operator can be written as [6]:

$$\vec{J} = \frac{4\pi W}{M}(i\widetilde{\sigma}F_1 + (\vec{\sigma} \cdot \hat{k}_\pi)(\vec{\sigma} \times \hat{q})F_2 + i\widetilde{k}_\pi(\vec{\sigma} \cdot \hat{q})F_3$$
$$+ i\widetilde{k}_\pi(\vec{\sigma} \cdot \hat{k}_\pi)F_4 + i\hat{q}(\vec{\sigma} \cdot \hat{q})F_5 + i\hat{q}(\vec{\sigma} \cdot \hat{k}_\pi)F_6)$$
$$\rho = \frac{4\pi W}{M}(i(\vec{\sigma} \cdot \hat{k}_\pi)F_7 + i(\vec{\sigma} \cdot \hat{q})F_8) = \frac{\vec{q} \cdot \vec{J}}{\omega} \tag{2.12}$$

The structure functions $F_{1,...,4}$ describe the transversal current, where F_5 and F_6 describe the longitudinal current. Because of the gauge invariance the charge can be replaced with the longitudinal current and vice versa [6]. The coincidence cross section can be expressed via six structure functions, which describe the transition current. The last two structural functions can be written as:

$$|\vec{q}|F_5 = \omega F_8, \qquad |\vec{q}|F_6 = \omega F_7 \tag{2.13}$$

To evaluate the differential cross section 2.8, an average over the unobserved spin

degrees of freedom of the initial state and a sum over the final states need to be done. According to [5] the triple differential cross section can then be written as:

$$\frac{d\sigma}{d\Omega_f d\epsilon_f d\Omega_\pi^\star} = \Gamma \frac{d\sigma_v}{d\Omega_\pi^\star} \tag{2.14}$$

Γ is the virtual photon flux and it is determined only by quantities in the laboratory frame ("$\star$" denotes quantities evaluated in the centre-of-mass frame):

$$\Gamma = \frac{\alpha}{2\pi^2} \frac{\epsilon_f}{\epsilon_i} \frac{k_\gamma}{Q^2} \frac{1}{1-\epsilon} \tag{2.15}$$

$k_\gamma = (W^2 - m_i^2)/2m_i$ is the so-called "photon equivalent energy". This is an energy in the laboratory frame, which a real photon needs to have, in order to excite the hadronic system to the centre-of-mass energy W.

Using the transition current operator 2.12 and the hadronic tensor 2.11, the virtual photon cross section $d\sigma_v/d\Omega_\pi^\star$ can be written as:

$$\frac{d\sigma_v}{d\Omega_\pi^\star} = \frac{|\vec{k}_\pi|}{k_\gamma^{CM}} \left(\frac{W_{xx} + W_{yy}}{2} + \epsilon_L^\star W_{zz} - \sqrt{2\epsilon_L^\star(1+\epsilon)} \operatorname{Re}(W_{xz}) + \epsilon \frac{W_{xx} - W_{yy}}{2} \right.$$
$$\left. + h\sqrt{2\epsilon_L^\star(1-\epsilon)} \operatorname{Im}(W_{yz}) + h\sqrt{1-\epsilon^2} \operatorname{Im}(W_{xy}) \right) \tag{2.16}$$

$k_\gamma^{CM} = (m_i/W)k_\gamma$ is the photon equivalent energy in the hadronic centre-of-mass frame. By setting the z-axis of the coordinate system to be in direction of the momentum transfer, it is possible to relate individual terms of the hadronic tensor with the longitudinal and the transversal components of the nucleon current. If the dependency on the angle between the reaction and the scattering plane $\phi_\pi = \phi_\pi^\star$ is expressed explicitly, it is possible to define six response functions, which are functions of three independent variables $Q^2, \omega_\pi^\star$ and $\theta_\pi^\star$ [6]:

$$R_T = \frac{1}{2}(W_{xx} + W_{yy}) \qquad R_L = W_{zz} \qquad \cos\phi_\pi R_{TL} = -\operatorname{Re} W_{xz}$$
$$\sin\phi_\pi R_{TL'} = \operatorname{Im} W_{yz} \qquad \cos 2\phi_\pi R_{TT} = \frac{1}{2}(W_{xx} - W_{yy}) \qquad R_{TT'} = \operatorname{Im} W_{xy} \tag{2.17}$$

With the help of 2.17, the virtual photon cross section can be expressed as:

$$\frac{d\sigma_v}{d\Omega_\pi^\star} = \frac{|\vec{k}_\pi|}{k_\gamma^{CM}} \left(R_T + \epsilon_L^\star R_L + \sqrt{2\epsilon_L^\star(1+\epsilon)} R_{TL} \cos\phi_\pi + \epsilon R_{TT} \cos 2\phi_\pi + \right.$$
$$\left. + h\sqrt{2\epsilon_L^\star(1-\epsilon)} R_{TL'} \sin\phi_\pi + h\sqrt{1-\epsilon^2} R_{TT'} \right) \tag{2.18}$$

It is possible to experimentally separate particular response functions and interpret them as a reaction cross section for the particular combination of the polarization of the virtual photon ϵ, the helicity of the electron h, and the angle ϕ_π [5, 6]:

$$
\begin{aligned}
\frac{d\sigma_v}{d\Omega_\pi^\star} =&\frac{d\sigma_T}{d\Omega_\pi^\star} + \epsilon_L^\star\frac{d\sigma_L}{d\Omega_\pi^\star} + \sqrt{2\epsilon_L^\star(1+\epsilon)}\frac{d\sigma_{TL}}{d\Omega_\pi^\star}\cos\phi_\pi + \epsilon\frac{d\sigma_{TT}}{d\Omega_\pi^\star}\cos 2\phi_\pi + \\
&+ h\sqrt{2\epsilon_L^\star(1-\epsilon)}\frac{d\sigma_{TL'}}{d\Omega_\pi^\star}\sin\phi_\pi + h\sqrt{1-\epsilon^2}\frac{d\sigma_{TT'}}{d\Omega_\pi^\star}
\end{aligned}
\tag{2.19}
$$

The first two terms from the left in 2.19 are the transversal T and the longitudinal L cross sections. It is possible to decompose them into a multipole series of $\cos\theta_\pi^\star$ and they do not depend on the angle ϕ_π. The third and the fifth terms are the transversal-longitudinal interference cross sections (TL and TL'). They depend on $\cos\phi_\pi$ and $\sin\phi_\pi$, and therefore they must have an explicit factor $\sin\theta_\pi^\star$, i. e. they vanish along the direction of the virtual photon transfer. The same applies to the fourth term, the transverse-transverse interference cross section TT, because of the $\sin^2\theta_\pi^\star$ proportionality.

In case of an unpolarized electron beam and an unpolarized target, only the first four terms in 2.19 (T, L, TL and TT) contribute to the virtual photon cross section $d\sigma_v/d\Omega_\pi^\star$. The contribution of the fifth term (TL') arises only if the incident electron beam is polarized and the last term (TT') appears for the simultaneously polarized target and the electron beam or in the case of a measurement of the recoil polarization.

The experiment which will be presented in this thesis was performed with the unpolarized electron beam and the unpolarized target. Hence, the fifth and the sixth term in 2.19 can be neglected. For the first set of kinematical settings the pion was detected in a direction of the virtual photon transfer (so-called "parallel kinematics" $\theta_\pi^\star = 0$). All terms in 2.19 which are proportional to $\sin\theta_\pi^\star$ vanish, so in the end only two terms remain:

$$
\begin{aligned}
\frac{d\sigma_v}{d\Omega_\pi^\star}\bigg|_{\theta_\pi=0} &= \frac{|\vec{k}_\pi|}{k_\gamma^{CM}}(R_T + \epsilon_L^\star R_L) \\
&= \frac{d\sigma_T}{d\Omega_\pi^\star} + \epsilon_L^\star\frac{d\sigma_L}{d\Omega_\pi^\star}
\end{aligned}
\tag{2.20}
$$

The transversal T and the longitudinal L cross sections can be separated by measuring the virtual photon cross section for various values of the photon polarization ϵ (and thereby $\epsilon_L^\star$) at fixed values of the four-momentum transfer Q^2 and the centre-of-mass energy W. Using a linear regression on a given data, according to the equation 2.20, the slope can be identified as the longitudinal L and the y-axis intercept as the transversal T cross section. The stated procedure is called the Rosenbluth separation.

The used experimental setup, which will be described in detail in subsequent sections, also allows a separation of the transversal-longitudinal interference term TL. The idea is to make two cross section measurements at $\phi_\pi = 0°$ and $\phi_\pi = 180°$ (or in other words "to the left" and "to the right" from the virtual photon direction $\vec{q}$). For those measurements values of ϵ, Q^2 and W should be fixed. In order to save a measurement time, the measurements should be performed for a large value of the ϵ (at the same time the cross section is also larger).

Because of the cosine dependence of the TL term, the "left" and the "right" TL terms will differ in a sign, but other terms (T and L) will stay the same:

$$\frac{d\sigma_{TL}}{d\Omega_\pi^\star} = \frac{\left.\dfrac{d\sigma_\nu}{d\Omega_\pi^\star}\right|_{\phi_\pi=0°} - \left.\dfrac{d\sigma_\nu}{d\Omega_\pi^\star}\right|_{\phi_\pi=180°}}{2\sqrt{2\epsilon_L^\star(1+\epsilon)}} \tag{2.21}$$

There is also another way to determine the TL term. Due to a high angular resolution of the spectrometers, it is possible to measure the virtual photon cross sections as a function of the polar angle θ_π and then the TL term can be extracted using a fit on the cross section's sine dependence. The ϵ, the Q^2 and the W should be fixed.

The TT interference term can be determined in an "out-of-plane" measurement, that is $\phi_\pi \neq 0°, 180°$. At present, it is not possible to perform the out-of-plane measurements with the SOS, this will be explained in chapter 4.

2.2.1 Partial wave analysis

For a near-threshold electroproduction of charged pions (in this experiment pions are produced around 15 MeV above the threshold) contributions of inelastic channels are negligible. This makes it one of those situations, where it is convenient to apply the Fermi-Watson theorem: for each multipole the electroproduction amplitude is a complex quantity whose phase is equal to the corresponding pion-nucleon phase shift [5]. Using this theorem it is possible to write each partial wave component (α) of the structure functions $F_i, i = 1, ..., 8$ as a product of a real function of the kinematic variables R_i^α and a phase shift for the elastic pion-nucleon scattering $\delta_\alpha = \delta_\alpha(\omega_\pi^\star)$ of the channel α, defined by the orbital angular momentum $l = 0, 1, 2, ...$, the total spin $J = |l \pm 1/2|$, and the total isospin I (1/2 or 3/2) of the pion-nucleon system [6]:

$$F_i^\alpha = e^{i\delta_\alpha} R_i^\alpha \tag{2.22}$$

The angular momentum decomposition has to be done in the initial as well as in the final state. In the initial state the virtual photon is described by wave functions carrying

the spin 1 and having the orbital momentum $\tilde{l}$ relative to the target nucleon. Using the vector spherical harmonics the photon wave functions can be written as:

$$\mathbf{Y}_{\tilde{l}LM} = \sum_{\nu} C(1\lambda, \tilde{l}\nu|LM)\hat{e}_{\lambda}Y_{\tilde{l}\nu}(\hat{r}) \tag{2.23}$$

the transverse polarizations $\lambda = \pm 1$ are leading to the electric and the magnetic multipole transitions, the longitudinal polarization $\lambda = 0$ leads to the longitudinal or the Coulomb transitions [6].

On the other hand, the final state is characterized by the pion orbital momentum l relative to the recoiling nucleon. Along with the intrinsic parity of the pion, the parity of the final state is $(-1)^{l+1}$. The final and the initial states have the same total spin J:

$$J = |l \pm \frac{1}{2}| = |L \pm \frac{1}{2}| \tag{2.24}$$

The parity arguments lead to:

$$\begin{array}{llll} coulomb, electric: & (-1)^L & = (-1)^{l+1} \rightarrow & |L - l| = 1 \\ magnetic: & (-1)^{L+1} & = (-1)^{l+1} \rightarrow & L = l \end{array} \tag{2.25}$$

Table 2.1 — Pion electroproduction amplitudes [6]. The notation is explained in the text.

γN-system		πN-system		
L	Multipol	J	l	Multipol
0	C0	1/2	1	L_{1-}
1	E1/C1	1/2	0	E_{0+}/L_{0+}
		3/2	2	E_{2-}/L_{2-}
	M1	1/2	1	M_{1-}
		3/2	1	M_{1+}
2	E2/C2	3/2	1	E_{1+}/L_{1+}
		5/2	3	E_{3-}/L_{3-}
	M2	3/2	2	M_{2-}
		5/2	2	M_{2+}

Table 2.1 contains the lowest electromagnetic excitation modes and the corresponding pion-nucleon states. The first two columns of the table 2.1 denote well-known electromagnetic multipoles, the third and the fourth columns contain the spin and the orbital momentum of the pion-nucleon system. The last column contains the pion production multipole in which the first index is the orbital momentum, the sign represent the orientation of the spin and the nucleon orbital momentum (sign "+" means that they are parallel $J = l + 1/2$).

The CGLN-amplitudes, which were introduced in subsection 2.3, can be decomposed into a multipole series [5] of derivatives of the Legendre polynomials P_l:

$$F_1 = \sum_{l \geq 0} \left\{ (lM_{l+} + E_{l+})P'_{l+1} + [(l+1)M_{l-} + E_{l-}]P'_{l-1} \right\}$$

$$F_2 = \sum_{l \geq 1} \left[(l+1)M_{l+} + lM_{l-} \right] P'_l$$

$$F_3 = \sum_{l \geq 1} \left[(E_{l+} - M_{l+})P''_{l+1} + (E_{l-} + M_{l-})P''_{l-1} \right]$$

$$F_4 = \sum_{l \geq 2} \left(M_{l+} - E_{l+} - M_{l-} - E_{l-} \right) P''_l \qquad (2.26)$$

$$F_5 = \sum_{l \geq 0} \left[(l+1)L_{l+}P'_{l+1} - lL_{l-}P'_{l-1} \right]$$

$$F_6 = \sum_{l \geq 1} \left[lL_{l-} - (l+1)L_{l+} \right] P'_l$$

The multipoles depend on the energy W and the momentum transfer Q^2, and the Legendre polynomials are functions of the polar angle of the pion in the centre-of-mass frame $\theta_\pi^\star$ [6].

The multipole decomposition of the CGLN amplitudes can be used to express response functions via multipoles. The decomposition of the response functions up to $l = 1$ follows:

$$\begin{aligned} R_T =\ & |E_{0+}|^2 + 0.5|2M_{1+} + M_{1-}|^2 + 0.5|3E_{1+} - M_{1+} + M_{1-}|^2 \\ & + 2\cos\theta_\pi^\star \operatorname{Re}\left\{ E_{0+}^*(3E_{1+} + M_{1+} - M_{1-}) \right\} \\ & + \cos^2\theta_\pi^\star \left(|3E_{1+} + M_{1+} - M_{1-}|^2 - 0.5|2M_{1+} + M_{1-}|^2 \right. \\ & \left. - 0.5|3E_{1+} - M_{1+} + M_{1-}|^2 \right) \end{aligned}$$

$$\begin{aligned} R_L =\ & |L_{0+}|^2 + 4|L_{1+}|^2 - 4\operatorname{Re}\left\{ L_{1+}^* L_{1-} \right\} + 2\cos\theta_\pi^\star \operatorname{Re}\left\{ L_{0+}^*(4L_{1+} + L_{1-}) \right\} \\ & + 12\cos^2\theta_\pi^\star \left(|L_{1+}|^2 + \operatorname{Re}\left\{ L_{1+}^* L_{1-}^* \right\} \right) \end{aligned} \qquad (2.27)$$

$$\begin{aligned} R_{TL} =\ & -\sin\theta_\pi^\star \operatorname{Re}\left(L_{0+}^*(3E_{1+} - M_{1+} + M_{1-}) - (2L_{1+}^* - L_{1-}^*)E_{0+} \right. \\ & \left. + 6\cos\theta_\pi^\star \left(L_{1+}^*(E_{1+} - M_{1+} + M_{1-}) + L_{1-}^* E_{1+} \right) \right) \end{aligned}$$

$$R_{TT} = 3\sin^2\theta_\pi^\star \left(\frac{3}{2}|E_{1+}|^2 - 0.5|M_{1+}|^2 - \operatorname{Re}\left\{ E_{1+}^*(M_{1+} - M_{1-}) + M_{1+}^* M_{1-} \right\} \right)$$

In vicinity of the threshold only S partial waves remain, so that the E_{+0} multipole contributes only to the T cross section term and the L_{+0} multipole to the L cross section term:

$$\frac{d\sigma_T}{d\Omega_\pi^\star} = \frac{|\vec{k}_\pi|}{k_\gamma^{CM}}|E_{0+}|^2 \qquad\qquad \frac{d\sigma_L}{d\Omega_\pi^\star} = \frac{|\vec{k}_\pi|}{k_\gamma^{CM}}|L_{0+}|^2 \qquad (2.28)$$

2.2.2   Electromagnetic vector form factors

By respecting the charge conservation, the Lorentz invariance and spatial symmetries the most general vector current matrix element of a nucleon is given by equation 2.29. It gives a full description of the transition probability for the elastic electron scattering on nucleon from the initial state $|N(P_i)\rangle$ to the final state $|N(P_f)\rangle$:

$$\langle N(P_f)| J^\mu(0) |N(P_i)\rangle = \bar{u}(P_f)\left\{ eF_1(Q^2)\gamma^\mu + \frac{ie}{2M}F_2(Q^2)\sigma^{\mu\nu}q_\nu \right\}u(P_i) \qquad (2.29)$$

where M is the nucleon mass, $J^\mu(x)$ is the electromagnetic current operator, F_1 is the helicity-non-flip Dirac form factor and F_2 is the helicity-flip Pauli form factor, $u(P)$ is the nucleon Dirac spinor. $\gamma^\mu = (\gamma^0, \gamma^1, \gamma^2, \gamma^3)$ are Dirac γ matrices, $\sigma^{\mu\nu} = i/2[\gamma^\mu, \gamma^\nu] = i/2(\gamma^\mu\gamma^\nu - \gamma^\nu\gamma^\mu)$ is the antisymmetric traceless combination of γ-s and $q^\mu = (P' - P)^\mu$ is the four-momentum of the virtual photon [16, 18, 19].

In the one photon approximation, the elastic differential cross section in the laboratory frame for the unpolarized electron scattering on a nucleon with the internal structure is:

$$\left.\frac{d\sigma}{d\Omega}\right|_{Lab} = \left.\frac{d\sigma}{d\Omega}\right|_{Mott} \cdot \frac{E'}{E}\left\{ F_1^2(Q^2) + \tau F_2^2(Q^2) + 2\tau\left(F_1(Q^2) + F_2(Q^2)\right)^2 \tan^2\frac{\theta_e}{2} \right\} \quad (2.30)$$

where $\tau = Q^2/(4M^2)$ is the dimensionless quantity, θ_e is the electron scattering angle, E is the incident and E' is the final electron energy. The Mott cross section describes scattering of a spin $1/2$ particle on a point-like target. In order to avoid the mixed form factor term in 2.30, it is convenient to use the so-called electric G_E and the magnetic G_M Sachs form factors:

$$G_M = F_1 + F_2, \qquad\qquad G_E = F_1 - \tau F_2 \qquad\qquad (2.31)$$

In the Breit frame, defined by $q^\mu = (0, \vec{q})$, the energy of the virtual photon vanishes and the Sachs form factors become functions of $\vec{q}$. Now the G_E and the G_M can be interpreted as a 3-dimensional Fourier transform of the spatial distribution of the electric charge and the magnetization densities, respectively [20].

In terms of the Sachs form factors, the differential cross section is now:

$$\left.\frac{d\sigma}{d\Omega}\right|_{Lab} = \left.\frac{d\sigma}{d\Omega}\right|_{Mott} \cdot \frac{E'}{E}\left\{ \frac{G_E^2(Q^2) + \tau G_M^2(Q^2)}{1 + \tau} + 2\tau G_M^2(Q^2) \tan^2\frac{\theta}{2} \right\} \qquad (2.32)$$

The Sachs form factors can be extracted from the measured cross section using the Rosenbluth method. For fixed Q^2 the measured cross section should behave as a linear function of $\tan^2\frac{\theta}{2}$. Now $2\tau G_M^2(Q^2)$ can be interpreted as a slope of this linear function, while G_E can be determined by extrapolating to $\tau = 0$ [20].

2.2.3 Weak axial-vector form factors

The use of the Lorentz, the parity and the isospin invariance, and the Dirac equation permits one to write the most general axial vector current matrix element of a nucleon, in the absence of second-class currents, as:

$$\langle N(P_f)| A^{\mu,a}(0) |N(P_i)\rangle = \bar{u}(P_f)\left\{G_A(Q^2)\gamma^\mu\gamma_5 + G_P(Q^2)\frac{q_\nu\gamma_5}{2M}\right\}\frac{\tau^a}{2}u(P_i) \qquad (2.33)$$

here $A^{\mu,a}(x)$ is the axial vector current operator, a denotes the isospin component, $\gamma_5 = i\gamma_0\gamma_1\gamma_2\gamma_3$ is the important traceless product of γ matrices, τ^a are Pauli matrices in the isospin space, $G_A(Q^2)$ is the axial-vector form factor, and $G_P(Q^2)$ is the induced pseudoscalar form factor.

The hadron vertex in the charged pion electroproduction near the threshold in the one photon exchange approximation can be split, as shown on Fig. 2.3, into a sum of individual processes. Only none-resonant Born terms are shown here, since the contributions from resonant Born terms and vector-meson exchange terms can be neglected near the threshold. It is also indicated, which form factor is associated with the particular Born term. If a kinematical setting is chosen appropriately, the contribution of the particular Born term to the overall cross section can be enhanced, and the corresponding form factor can be extracted from those data.
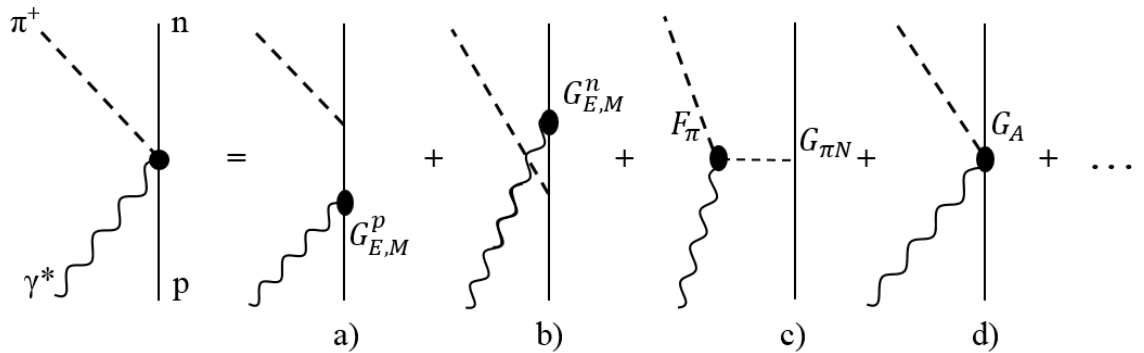
Figure 2.3 — Decomposition of the charged pion electroproduction hadron vertex into non-resonant Born terms: a) *s*-channel term, b) *u*-channel term, c) *t*-channel or pion pole term, d) contact or seagull term. Contribution of the resonant Born terms and vector-meson exchange terms near threshold can be neglected. The full circles represent corresponding form factors [10, 12, 16].

In the first two Born terms a photon is directly coupled to the nucleon, a) via *s*-channel to the proton or b) via *u*-channel to the neutron, represented as the direct and the crossed nucleon pole. The form factors associated with those terms are the electric

G_E and the magnetic G_M Sachs form factors of a) proton and b) neutron. They can be determined in the elastic electron scattering experiments.

The third term is the t-channel term or the pion pole term where the pion form factor F_π and the induced pseudoscalar form factor G_P play a significant role. The pion form factor F_π is of a monopole type $1/(1 + Q^2/\Lambda_\pi^2)$ with $\Lambda_\pi \approx 0.735$ GeV [9]. For the pion electroproduction near the threshold most important is the fourth contact term (also called the seagull or the Kroll-Rundemann term) closely related to the axial form factor G_A, which is of a dipole type, parameterized as:

$$G_A(Q^2) = \frac{G_A(0)}{\left(1 + \dfrac{Q^2}{M_A^2}\right)^2} \tag{2.34}$$

The $G_A(0) = g_A = 1.2701$ [13] is the axial coupling constant. M_A is the axial mass, which is directly connected to a mean square of the axial radius $\langle r_A^2 \rangle^{1/2} = \sqrt{12}/M_A$.

If one assumes the pion pole dominance of the induced pseudoscalar coupling, G_A and G_P are related by [6]:

$$G_P(Q^2) = \frac{4M^2}{m_\pi^2 + Q^2} G_A(Q^2) \tag{2.35}$$

In the pion pole term the virtual photon is coupled to the pion emitted from the nucleon, and because of this, the G_P is particularly sensitive to the pion cloud [21].

In the limit $Q \to 0$ and by using the partially conserved axial-vector current (PCAC) hypothesis, which states that the axial current is only conserved in the chiral limit ($m_\pi \to 0$) and without the presence of the electromagnetic field, it is possible to obtain the so-called Goldberger Treiman relation [22]. The importance of this relation is in providing the simple connection between the pion-nucleon coupling constant $g_{\pi N}$ of the strong interaction with the pion decay constant f_π and the axial coupling constant g_A of the weak interaction:

$$\frac{g_{\pi N}}{M} = \frac{g_A}{f_\pi} \tag{2.36}$$

where $M = 938.9$ MeV is the nucleon mass, $g_{\pi N} = 14.11$ [23], $f_\pi = 92.21$ MeV [13]. Using the 2.35 and the Goldberger Treiman relation 2.36 it is possible to relate the pseudoscalar form factor G_P with $g_{\pi N}$ and f_π:

$$G_P(Q^2) \simeq \frac{4M f_\pi g_{\pi N}}{m_\pi^2 + Q^2} \tag{2.37}$$

Within the framework of the quantum chromodynamics (QCD) coupled to external fields, starting from the most general effective chiral Lagrangian up to and including

$\mathcal{O}(q^3)$ in the baryonic sector (so-called Lorentz-invariant or relativistic formulation of chiral perturbation theory - RChPT) the results for the G_A and the G_P are [24]:

$$G_A(Q^2) = g_A \left(1 + \frac{1}{6}\langle r_A^2 \rangle Q^2\right) \tag{2.38}$$

$$G_P(Q^2) = 4M^2 \left(\frac{f_\pi g_{\pi N}}{M} \frac{1}{m_\pi^2 + Q^2} - \frac{1}{6} g_A \langle r_A^2 \rangle\right) \tag{2.39}$$

where

$$g_A = G_A(0) = \mathring{g}_A + \frac{b_{17} m_\pi^2}{4\pi^2 f_\pi^2} \tag{2.40}$$

$$\langle r_A^2 \rangle = \frac{6}{G_A(0)} \frac{dG_A(Q^2)}{dQ^2}\bigg|_{Q^2=0} = -\frac{6}{g_A} \frac{b_{23}}{4\pi f_\pi^2} \tag{2.41}$$

b_{17} in 2.40 and b_{23} in 2.41 are low energy constants from the tree-level approximation. The constant b_{17} provides correction to the axial coupling constant in the chiral limit $\mathring{g}_A$, and b_{23} is related to the axial radius $\langle r_A^2 \rangle$, which makes this term very important, since it is responsible for the Q^2 dependence of the axial form factor G_A [17].

2.2.4 Extraction of the axial form factor G_A from experimental data

The axial form factor G_A and the axial mass M_A are experimentally accessible in two different types of reactions: the quasi-elastic scattering of (anti-)neutrinos on various targets and the near threshold positive pion-on-proton electroproduction.

In experiments based on the quasi-elastic (anti-)neutrino scattering the axial form factor is extracted from the Q^2 dependence of the quasi-elastic (anti-)neutrino-nucleon cross section:

$$\frac{d\sigma_{\nu(\bar{\nu})}}{dQ^2} \propto \left[A \pm \frac{s-u}{M^2} B + \frac{(s-u)^2}{M^4} C\right] \tag{2.42}$$

where s and u are Mandelstam variables, M is the mass of the nucleon and most important A, B and C are bilinear forms of the electromagnetic nucleon form factors and the axial nucleon form factor. The exact expressions for the A, B and C can be found in [3]. Since the electromagnetic form factors are known, the only unknown which can be extracted from the cross section is the axial form factor together with the axial mass. Older experiments (summarized on left Fig. 2.4), affected by the relatively large statistical and systematic uncertainties, provide the weight averaged axial mass $M_A = 1.026 \pm 0.017$ GeV, or the scaled-error [13] averaged axial mass $M_A = 1.026 \pm 0.021$ GeV [11].

Contrary to that, almost all recent high statistics experiments (except the NOMAD

experiment) report even larger axial mass values, table 2.2. There are different ideas on the cause of this discrepancy [25, 26]. One of the possible explanations is usage of light nuclei as targets in the recent experiments, while in the older experiments the deuterium was predominantly used as the target. Therefore, it is not possible to exclude the influence of the nuclear medium on the axial mass [26]. But the real cause of this discrepancy still remains an open question.
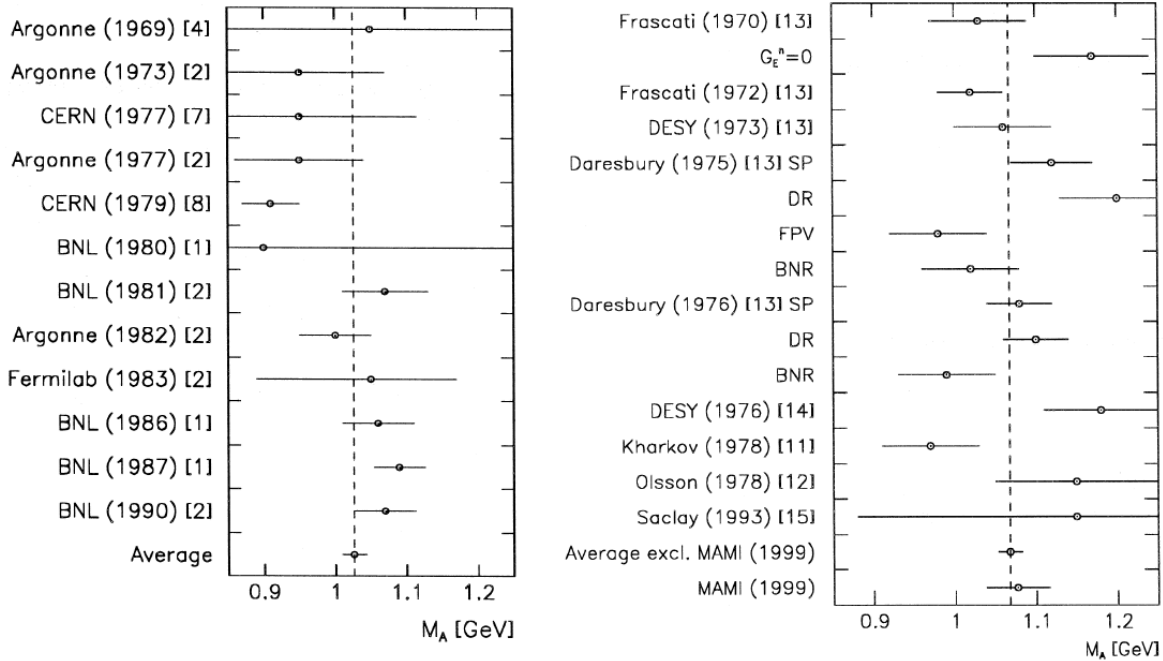
Figure 2.4 — Compilation of the axial mass data: the left figure refers to older neutrino scattering experiments, the right figure refers to data obtained in the pion electroproduction experiments. Figures and references indicated on them are from [11].

Table 2.2 — M_A values from recent experiments. Table from [25].

Experiment	Target	Cut in Q^2 (GeV/c)^2	M_A (GeV)
K2K	oxygen	$Q^2 > 0.2$	1.20 ± 0.12 [27]
	carbon	$Q^2 > 0.2$	1.14 ± 0.11 [28]
MINOS	iron	no cut	1.19 ± 0.17 [29]
	iron	$Q^2 > 0.2$	1.26 ± 0.17 [29]
MiniBooNE	carbon	no cut	1.35 ± 0.17 [30]
	carbon	$Q^2 > 0.2$	1.27 ± 0.14 [30]
NOMAD	carbon	no cut	1.07 ± 0.14 [31]

For the charged pion electroproduction near the threshold, the T and the L cross section terms are well-described only with the s-wave multipoles 2.28. In the case of

the $p(e, e'\pi^+)n$ reaction this are $E_{+0}^{(-)}$ and $L_{+0}^{(-)}$ multipoles. Nambu, Lurié and Shrauner calculated the electric dipole amplitude $E_{+0}^{(-)}$ for the virtual photons at the threshold in the limit of massless pions:

$$E_{+0}^{(-)}(m_\pi = 0, q^2) = \sqrt{1 - \frac{q^2}{4M^2}} \frac{eG_A(0)}{8\pi f_\pi} \left[G_A(q^2) + \frac{q^2}{4M^2 - 2q^2} G_M(q^2) \right] \qquad (2.43)$$

This equation can be expanded to the q^2 order:

$$E_{+0}^{(-)}(m_\pi = 0, q^2) = \frac{eG_A(0)}{8\pi f_\pi} \left[1 + \frac{q^2}{6} \langle r_A \rangle + \frac{q^2}{4m} \left(\kappa_v + \frac{1}{2} \right) + \mathcal{O}(q^3) \right] \qquad (2.44)$$

κ_v is the anomalous magnetic moment of the nucleon. The equations 2.43 and 2.44 are valid for the massless pion with the zero three-momentum and they have to be extrapolated to the physical region with the finite pion mass and the finite pion momentum. There are several model-dependent procedures to do this and the model-independent procedure based on the chiral perturbation theory (χPT), an overview of this topic can be found in [10]. Now it is possible to extract the axial radius r_A from the q^2-slope of the T cross section term and determine the axial mass $M_A = \sqrt{12/\langle r_A^2 \rangle}$.

The results for the axial mass M_A determined in electroproduction experiments are summarized on the right Fig. 2.4. The weighted scaled-error average of the axial mass from many earlier experiments amounts to $M_A = 1.069 \pm 0.016$ GeV [11]. In the most recent experiment, carried out in the framework of the A1 collaboration at MAMI, the extracted axial mass was determined to be 1.077 ± 0.039 GeV [11].

The axial mass discrepancy between the old (anti-)neutrino and the pion electroproduction experiments can be explained in the framework of χPT [4], but this does not hold for the new (anti-)neutrino experiments.

When using the pion electroproduction to determine the M_A (or r_A) from the q^2-dependence of the T cross section term, one also obtains the q^2-dependence of the L cross section term (or of the $L_{+0}^{(-)}$ multipole 2.28), from which it is possible to extract the induced pseudoscalar form factor G_P. The extraction procedure is more complicated, since the $L_{+0}^{(-)}$ multipole also contains contributions from the pion form factor F_π and the pion-nucleon form factor $G_{\pi N}$. The full expression for the $L_{+0}^{(-)}$ multipole can be found in [5], the expression evaluated in framework of the χPT can be found in [4]. The L cross section term has to be determined for pions with kinetic energy less than 35 MeV [12] to ensure the domination of the s-wave multipoles in the L term. The T term is well-described by the s-wave multipole even for higher pion kinetic energies.

<div align="right">

3

</div>

Experimental Facility

In this chapter, the description of the MAMI electron accelerator and the standard three spectrometer setup of the A1 collaboration together with their main components will be given. Since the SOS is a nonstandard spectrometer, its description will be given in the following chapter.

3.1 Mainz Microtron - MAMI

The Mainz Microtron (MAMI) is a so-called continuous wave electron accelerator. The beam is divided into electron bunches with a repetition frequency of 2.45 GHz. Because of the high frequency, the detectors used by the experimentalists groups can not register each bunch separately, therefore it seems as if the beam was continuous. The machine can deliver beam currents from 10 pA up to 100 µA and energies between 180 MeV and 1.6 GeV. Due to the synchrotron radiation, the root mean square energy spread of the beam is 30 keV at 855 MeV and 110 keV at 1.5 GeV. At present, there are five successive stages: a linear injector accelerator, three consecutive race-track microtrons (RTM) and a harmonic double-sided microtron (HDSM) [32, 33]. A floor plan with schematics is shown on Fig. 3.1.

The RTMs consist of a linear accelerator placed between two high precision dipole magnets, which bend the beam path for 180° and enable the beam recirculation. The HDSM consists of two anti-parallel linear accelerators. One of the linear accelerators is operated on a double frequency to suppress beam instabilities. The beam is recirculated by four magnets, each bending the beam for 90°.

The accelerator can provide two types of the electron beam: unpolarized and polarized. For the unpolarized beam a thermionic source is used. A beam current up to 100 µA can be reached with this source. Polarized electrons are produced by a photoelec-

tric effect of a polarized laser light on the *GaAs* crystals. The polarization of the beam is around 80%. The 100 μA beam current can be also achieved [33], but in order to prevent the damage and prolong the lifetime of the *GaAs* crystals the maximum current of the polarized beam is usually limited to 20 μA.
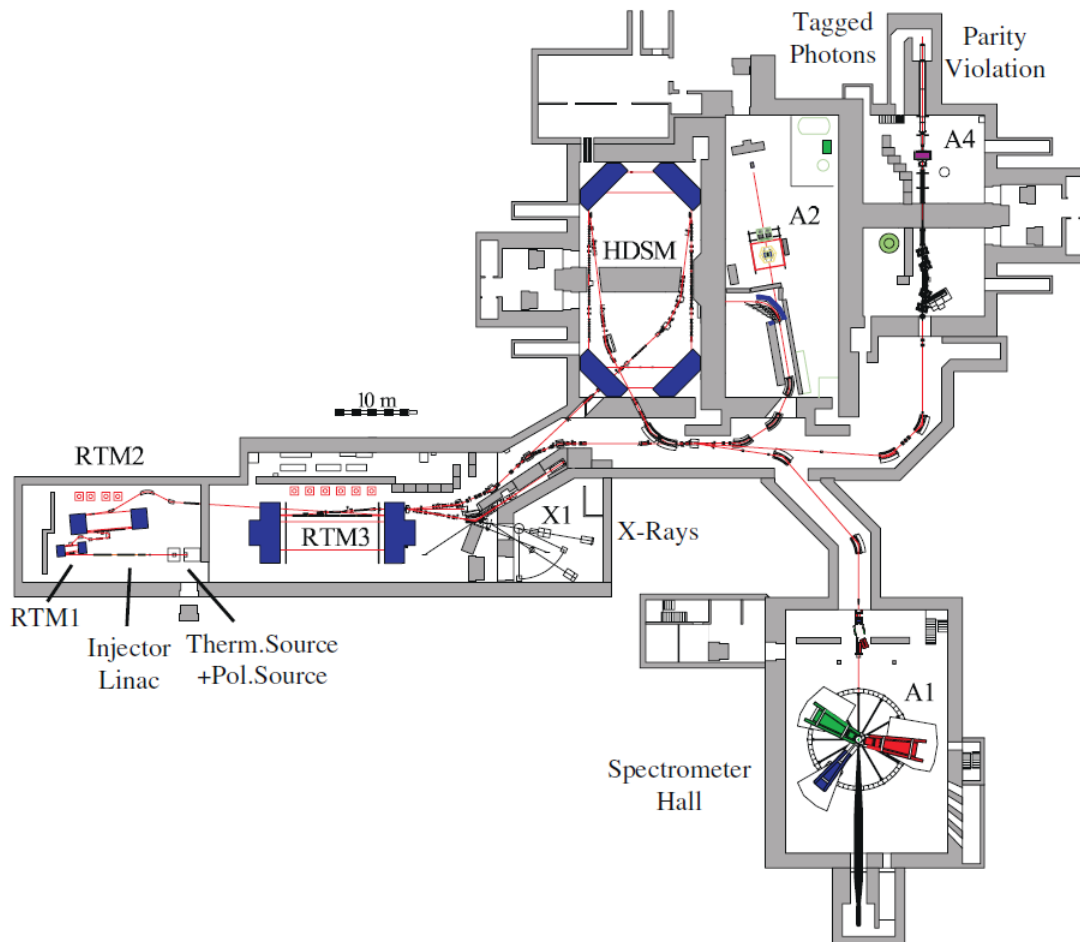
Figure 3.1 — Floor plan of MAMI accelerator and experimental halls. Figure form [32].

After the source, the beam is accelerated to 3.5 MeV by the linac accelerator and injected into the first RTM. Here, the beam is recirculated 18 times, thereby increasing the beam energy to 14.9 MeV. The second RTM is known as MAMI-A. After the 51 turns the beam energy is raised to 180 MeV, which is the minimal energy for which the MAMI accelerator provides a stable beam. At this point the rest of the MAMI stages can be bypassed and the beam can be directed to different experimental halls. The third RTM, called MAMI-B, accelerates the beam after 90 turns up to 855 MeV. This stage is equipped with a kicker magnet and by selecting appropriate recirculation path, it can extract beam energies in 15 MeV steps. The final HDSM stage, called MAMI-C, gives in 43 turns the maximum beam energy of 1.6 GeV [33].

3.2 Target system

The target system is placed inside the vacuum scattering chamber, which is located in the centre of the spectrometers rotation axis. A target ladder can be equipped with several solid state materials of various thickness, such as polyethylene, graphite, tantalum, copper etc. For each experiment the ladder holds a luminescent screen (chromium doped Al_2O_3 plate with a cross hair printed on), which is used for the beam position calibration. The desired material is selected by moving the ladder in a vertical direction. This is controlled remotely and can be done during the beam-time.

There are two different upper lids for the scattering chamber, one for a high-pressure gas target (helium) and the other for the cryogenic liquid target (hydrogen or deuterium).

The cryogenic liquid target system consists of two cooling loops. In the outer loop the hydrogen is liquefied at the Philips compressor and then transported via transfer pipe to a heat exchanger inside the scattering chamber. The liquid hydrogen is cooling the heat exchanger and the warmed up gas then returns to the Philips compressor, closing the outer loop.
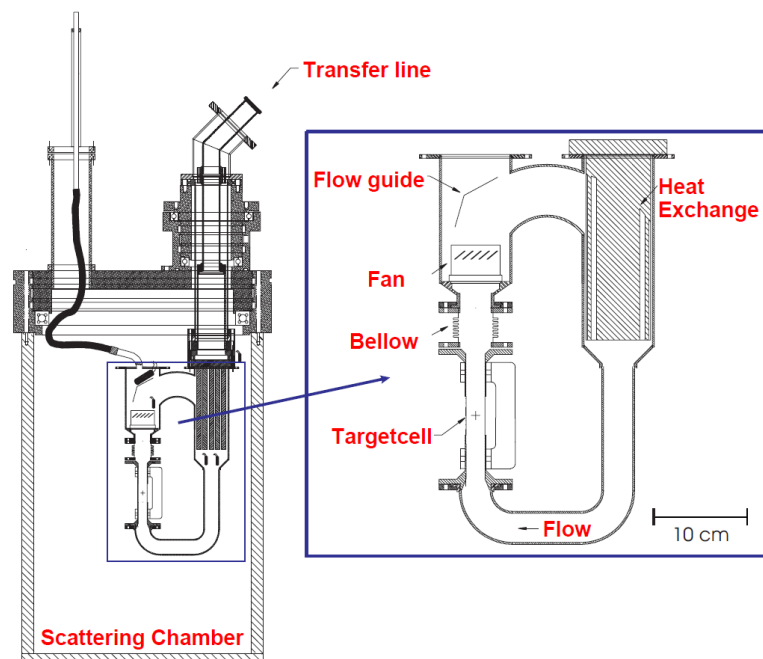
Figure 3.2 — Scattering chamber and hydrogen cryo target inner loop. The + sign in the zoomed image represents the central point of the electron beam. Figure form [10].

The heat exchanger is also coupled to the inner loop Fig. 3.2 (called Basel-loop), which contains the target gas. Before the beginning of each experiment the target gas is liquefied. The inner loop can be equipped with two target cells: the cylindrical cell with

a diameter of 2 cm made of the 50 μm thick Havar foil and the cigar-like cell with the length of 4.95 cm, the width of 1.15 cm and the height of 1 cm made of the 10 μm thick Havar foil. The target liquid is under-cooled and recirculated by a ventilator, in order to prevent a local overheating by the electron beam and a creation of gas bubbles in the target cell. For higher beam currents the effective heat deposition by the electron beam has to be further reduced. Therefore, the beam is additionally rastered in transverse directions at a frequency of several kHz and an amplitude of few mm. The temperature and the pressure inside the inner loop are monitored during the experiment, enabling the determination of the liquid target density. The stable density of the liquid target is essential for a precise calculation of the luminosity.

3.3 The three spectrometer facility

The main experimental setup of the A1-collaboration at the Institute for Nuclear Physics in Mainz, consists of three high resolution magnetic spectrometers, which are labelled A, B and C. The spectrometers can be operated in a single, double or triple coincidence mode. All three spectrometers can be rotated around the target in the centre for the detection of charged particles at different scattering angles. Using the deflection of the particles in the magnetic field and the trajectory measurement in vertical drift chambers it is possible to determine the particle momenta. The information from the scintillator planes and the Čerenkov detectors enables the particle identification. The A1 experimental hall with the spectrometers is shown on the Fig. 3.3. In the following text a summary of their optical properties and a brief description of the detector packages will be given. The detailed description of the facility can be found in [34].

3.3.1 Optical properties of spectrometers

The magnets of spectrometers A and C are arranged in a quadrupole-sextupole-dipole-dipole (QSDD) configuration. Magnetic field of the quadrupole magnet simultaneously influences the particles in two ways. By focusing the particles in a non-dispersive direction, the quadrupole magnet consequently enlarges the scattering angle acceptance and by defocusing in a dispersive direction, it increases the intrinsic momentum resolution of the spectrometer. The role of the sextupole magnet is to correct second-order imaging errors, or the so-called spherical aberration. The two dipole magnets are bending the particle trajectories towards the detector packages. Such magnet configuration enables the high resolution measurement of the particle angle and momentum at a relatively large acceptance (28 msr). Spectrometer C is a down-scaled version of spectrometer A, the scaling factor is 11/14.

Figure 3.3 — The experimental hall of A1 collaboration. The name of the spectrometers, from left to the right, are A (red), B (blue) and C (green). In the middle of the photo is the SOS, placed in front of the target. The electron beam pipe is coming from the right side.
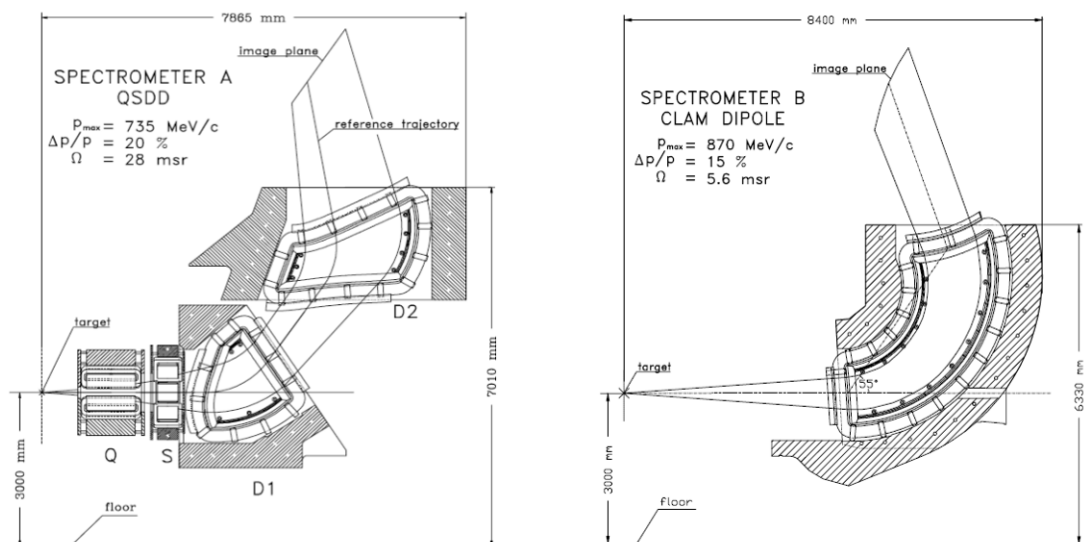

Figure 3.4 — Arrangement of the magnets and the dimensions of spectrometers A (left) and B (right). Figure from [34].

Spectrometer B has only one dipole magnet in a clamshell configuration. Because of this, spectrometer B is of a slimmer design in comparison with other two spectrometers, and can reach scattering angles down to 7°. The inclination of the pole shoes in the clamshell configuration creates a double focusing inhomogeneous field, thus enabling the point-to-point focusing in the dispersive as well as in the non-dispersive plane [34]. The spatial resolution is therefore higher, but the acceptance is smaller (5.6 msr). This spectrometer can also be tilted up to 10° for the out-of-plane measurements. The main properties of the spectrometers are summarized in table 3.1, and the lay-outs of spectrometer A and B are shown on Fig. 3.4.

Table 3.1 — Properties of the spectrometers. All information are design values for A, B and C from [34] and for SOS from [14]. The SOS dispersion and the SOS angular resolution at the target, were measured for the SOS at 54 cm distance from the target [16]. Missing entries could not be determined. About the configuration: * Clamshell magnet, ** Browne-Buechner magnet, $(\| \to \cdot)$ = Parallel to Point imaging, $(\cdot \to \cdot)$ = Point to Point imaging [35].

Spectrometer		A	B	C	SOS
Configuration		QSDD	D*	QSDD	D**
Imaging mode					
Dispersive plane		$\cdot \to \cdot$	$\cdot \to \cdot$	$\cdot \to \cdot$	-
Non dispersive plane		$\| \to \cdot$	$\cdot \to \cdot$	$\| \to \cdot$	-
Maximum momentum	[MeV/c]	735	870	551	147
Reference trajectory momentum	[MeV/c]	630	810	459	–
Central trajectory momentum	[MeV/c]	660	810	490	–
Momentum acceptance	[%]	20	15	25	21
Angle acceptances					
Dispersive plane	[mrad]	±70	±70	±70	±80
Non dispersive plane	[mrad]	±100	±20	±100	±14.8
$\Rightarrow$ Solid angle	[msr]	28	5.6	28	4.8
Scattering angle range	[°]	18 - 160	7 - 62	18 - 160	15 - 62
Angle of focal plane	[°]	45	47	45	53
Length of the central trajectory	[m]	10.75	12.03	8.53	1.54
Dispersion (central trajectory)	[cm/%]	5.77	8.22	4.52	$\simeq 1.0$
Magnification (central trajectory)		0.53	0.85	0.51	-
Dispersion/Magnification	[cm/%]	10.83	9.64	8.81	-
Momentum resolving power		$\leq 10^{-4}$	$\leq 10^{-4}$	$\leq 10^{-4}$	$1.3 \cdot 10^{-3}$
Angular resolution at the target	[mrad]	≤ 3	≤ 3	≤ 3	5.3 (θ)
					33.7 (ϕ)
Spatial resolution at the target	[mm]	3 - 5	≤ 1	3 - 5	-

The spectrometers central magnetic field and thereby the central momentum, is determined and monitored with Hall and NMR probes. The Hall probes measure rough values of the magnetic field, and the NMR probes give very precise values for the fine adjustment of the central momentum.

3.3.2 Detector systems

The standard detector packages of all three spectrometers are similar. They consist of four vertical drift chambers, two scintillator planes and a gas Čerenkov detector, see Fig. 3.5. The VDCs are used for reconstruction of particle trajectories, the scintillator planes for triggering, and both planes can be used for differentiating between protons and lighter particles (charged pions, electrons and positrons). The scintillator planes are not suitable for discrimination between electrons (positrons) and charged pions, for this purpose the gas Čerenkov detector is used. Additionally, the gas Čerenkov detector in spectrometer A can be replaced with a proton polarimeter.
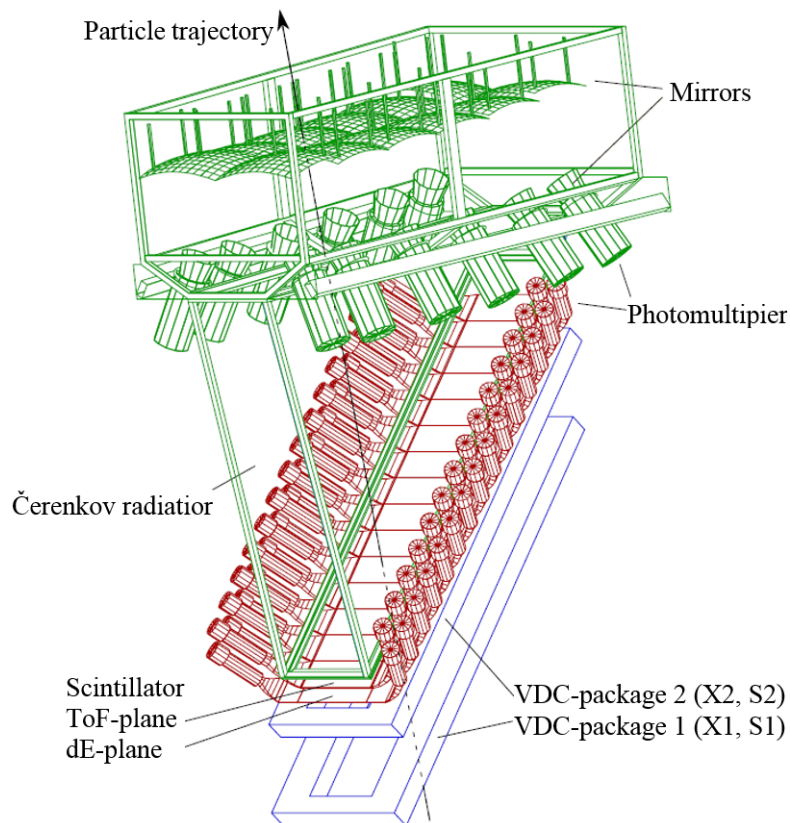
Figure 3.5 — Illustration of the standard detector package of the spectrometers. The incoming particles first pass through the vertical drift chambers (blue), two scintillator planes (red) and a gas Čerenkov detector (green). This version of the figure is from [36], the original in black and white is from [34].

3.3.2.1 Vertical drift chambers

After passing the magnets, particles are going through two pairs of vertical drift chambers (VDC). Each pair consists of two individual VDC planes called x- and s-plane, see Fig. 3.6. X-wires of the first VDC plane are perpendicular to the dispersive plane and they measure particle trajectory in the dispersive direction. In the second VDC plane,

s-wires are rotated for 40° with respect to x-wires and they measure particle trajectory in the non-dispersive direction. The first x-plane is always placed inside the focal plane.
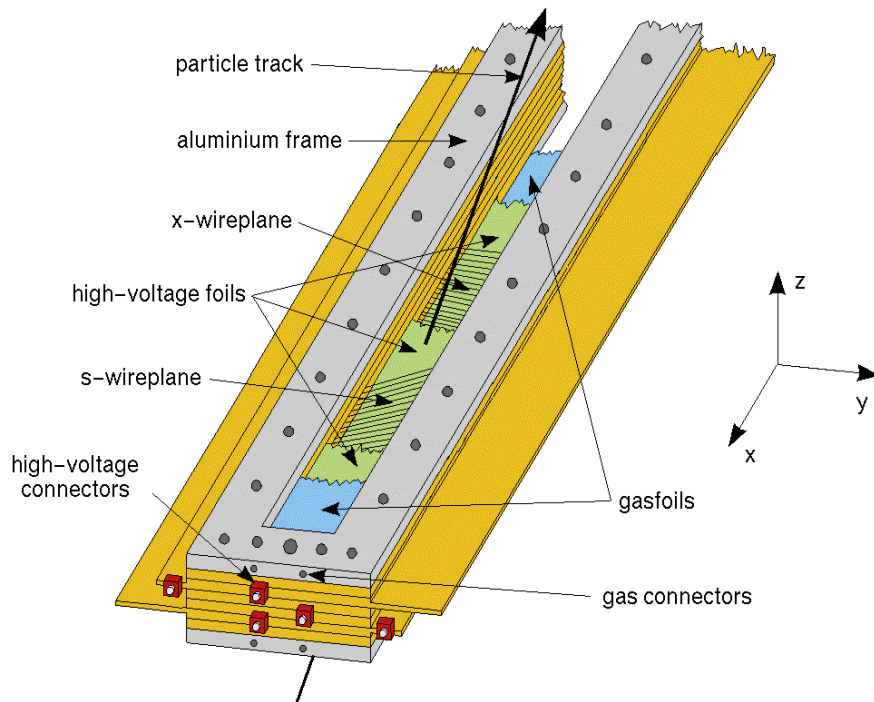
Figure 3.6 — Schematics of a VDC. The s-wires are rotated for 40° relative to the x-wires [34].

Each VDC wire plane consists of alternating signal and potential wires, placed between cathode foils, Fig. 3.7. The distance between the wires is 2.5 mm and the distance between wire plane and cathode foils is 12 mm. The potential wires are grounded directly and the signal wires are held on 0 V via preamplifier. The foils are set at a negative potential of $5600 - 6500$ V. The volume of the VDC is filled with a mixture of argon and isobutane gas with a 1.5% admixture of the pure ethanol to minimize aging.
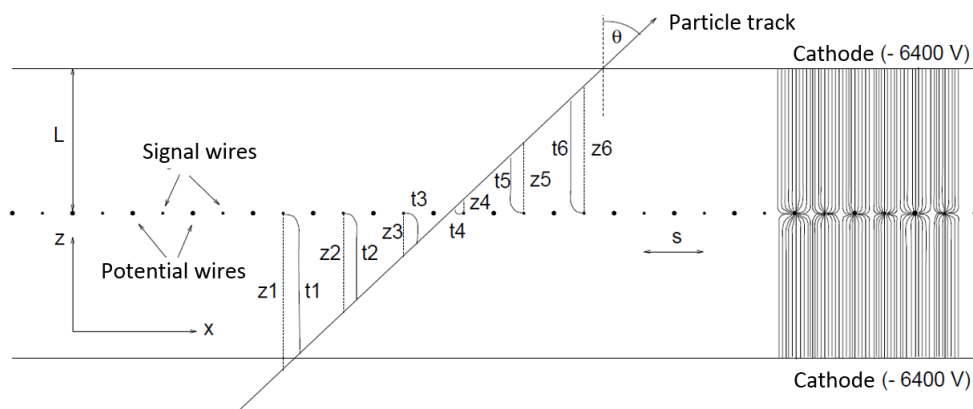
Figure 3.7 — Longitudinal section of the VDC: illustration of the VDC operational principle (left) and illustration of the electric field distribution (right). Figure from [34].

A charged particle passing through the gas will produce electron-ion-pairs along its trajectory. The ions will drift towards the cathode foils, while the primary and the secondary electrons will drift with a known velocity towards the wires. All signal wires work in a common stop mode: a signal from a wire starts the time measurement and the delayed signal from the scintillators is a common stop. The time measurement for each wire is translated into the distance from the particle trajectory to the wire. The information from at least three wires is needed for good particle trajectory reconstruction. The distance between the VDC pairs is 20 cm, which allows achieving a spatial resolution ≤ 200 µm in the dispersive and ≤ 400 µm in the non-dispersive direction. The VDCs measure the particles' focal-plane coordinates: dispersive (x_{fp}, θ_{fp}) and non-dispersive (y_{fp}, ϕ_{fp}). Additional details about the VDCs can be found in [37].

3.3.2.2 Scintillators

In each spectrometer two layers of segmented plastic scintillator planes are used as trigger detectors, Fig. 3.8. The scintillator planes in spectrometer A and C are made of 15 paddles and in spectrometer B of 14 paddles. The paddles in A and C are 45 cm long and read out is performed in coincidence from both sides. The length of paddles in spectrometer B is only 14 cm, and read out is made from one side. The segmentation increases the rate capacity of the entire detector package, improves the time resolution due to shorter propagation time of the light, and gives a rough position of the particle trajectory.
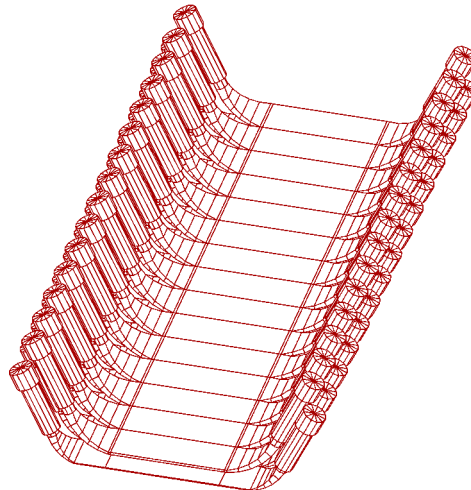
Figure 3.8 — Two segmented plastic scintillator planes of spectrometer A. The ToF layer measures the time of flight and the dE layer is used to differentiate protons from minimum ionizing particles. Figure from [34].

The bottom plane (dE-plane) is 3 mm thick and the upper plane (ToF-plane) is 10 mm thick. The scintillator material and the corresponding photomultiplier tubes of

dE-plane are selected to have better energy resolution, and of ToF plane to have better time resolution [34]. Normally, the dE-plane gives the energy loss information of the passing particle and only in case of slow particles, such as protons or deuterons, also provides the timing. For all other situations, ToF-plane defines the timing. This signal is used for coincidence determination between spectrometers as well as the common stop signal for the VDCs. The energy loss information from both plans can be used to differentiate heavier (protons, deuterons) from minimum ionizing particles (charged pions, electrons or positrons).

3.3.2.3 Čerenkov detector

The volume of the Čerenkov detector, Fig. 3.5, is filled by C_4F_{10} gas with refraction index of 1.0013. Passing through electrons or positrons with energies larger than 10 MeV will produce Čerenkov light in this media. A system of mirrors reflects the Čerenkov photons towards the array of photomultiplier tubes. Only pions with energies larger than 2.7 GeV will create the Čerenkov light. Since it is not possible to produce such pions even with maximum electron beam energy of 1.6 GeV, the Čerenkov detector can differentiate between electrons or positrons and heavier particles.

3.3.2.4 Trigger electronics and data acquisition

All three spectrometers are equipped with independent electronics. The purpose of those electronics is signal amplification and analog-to-digital conversion, as well as generation of the trigger signal for data acquisition. The minimum condition for generation of the trigger signal is fulfilled, if a hit in the scintillator paddle crates a signal, which is larger than a certain threshold. This minimum trigger condition can be also extended to have signal in: dE and ToF plane (coincidence condition), dE or ToF plane, only dE plane, only ToF plane. The scintillator signals can be also put in coincidence or anti-coincidence with the Čerenkov detector. During the beam time this conditions can be selected via programmable logic unit (PLU) [34].

The PLU signals from all three spectrometers are sent to a universal logic module (ULM) equipped with a field programmable gate array (FPGA). It is possible to change the width of incoming signals, delay them and scale down their rate via prescalers depending on the kinematical configuration and the measured physical reaction. During the beam time FPGA can be set to following logical conditions: singles A, singles B, singles C, coincidence AB, coincidence BC and coincidence ABC [38]. When the ULM accepts an event it distributes the gate signals back to electronics of spectrometers to start the analog-to-digital conversion of the time and energy information from differ-

ent scintillators. At the same time an interrupt signal is sent to front-end computers to read out all the data. During the analog-to-digital conversion and data read-out, a busy signal is generated by a micro busy module to prevent further data taking. The time at which the system can accept events and the total measurement time is later used for the dead time determination. Each spectrometer is read-out asynchronously and an event-builder module is used for synchronization of multi-arm events. This module assigns an unique number to each event and enables merging of single-arm events. A more detailed description of the trigger system can be found in [38].

<div style="text-align: right; font-size: 4em; color: gray;">4</div>

Short-Orbit Spectrometer (SOS)

In this chapter an advantage of the short-orbit spectrometer over the A1 standard spectrometers in detection of the low-energy pions will be explained. Optical properties of the magnet and the choice of collimators associated with those properties will be discussed, as well as the choice of the detector package.

4.1 Need for another spectrometer

The goal of the experiment is to measure the charged pion electroproduction as near the reaction threshold as possible. Major difficulty in detecting charged pions arises from the fact that pions are unstable particles, with $\tau_\pi = 26.033$ ns lifetime in the pion rest frame. The decay is described by the simple decay law:

$$N_\pi(s) = N_{0,\pi} \cdot e^{-\frac{s}{l_\pi}} = N_{0,\pi} \cdot e^{-\frac{s m_\pi c}{E_\pi \tau_\pi \beta_\pi}} = N_{0,\pi} \cdot e^{-\frac{s m_\pi}{p_\pi \tau_\pi}} \tag{4.1}$$

where l_π is the pion decay length or the average path length traversed by the pion of the momentum p_π before decaying.

The trajectory length from the target to the detector package in a standard A1 spectrometer is in order of 10 m. In case of the pions with the momentum of 113 MeV/c, only 20.6% will survive this path. Charged pions dominantly decay into muons and neutrinos (99.9877% [13]). Due to their longer life 2.197 μs most of the muons will reach the detector package before they decay. Most muons will have different trajectories with respect to pions and their reconstructed momentum will differ very much from that of the decayed pion. But for a certain fraction of muons, which are created near the detector package or in direction of the decayed pion, the reconstructed momentum will be very similar to that of the pion and such muon will contaminate the data. This fraction has to be determined via simulation.

In past experiments [10–12] muon contamination was one of major contributions to the systematic error. This contribution can be decreased by reducing the pion path from the target to the detector package. Therefore, a new spectrometer was designed with a central trajectory length of about 1.6 m, and because of that it has been called short-orbit spectrometer (SOS), see Fig. 4.1. In SOS 77.6% of pions with momentum of 113 MeV/c will survive the path length of 1.6 m.

Furthermore, in every tracking detector a certain probability of multiple scattering exists, which worsens the detector resolution. As the particle kinetic energy decreases the probability of the multiple scattering increases. The effective thickness of the SOS tracking detector was optimized to minimize energy loss and multiple scattering, hence it is smaller than in case of the standard spectrometers. This was achieved by choice of a volume type drift chamber as a tracking detector, which has less number of foils and no air between the chambers [15].
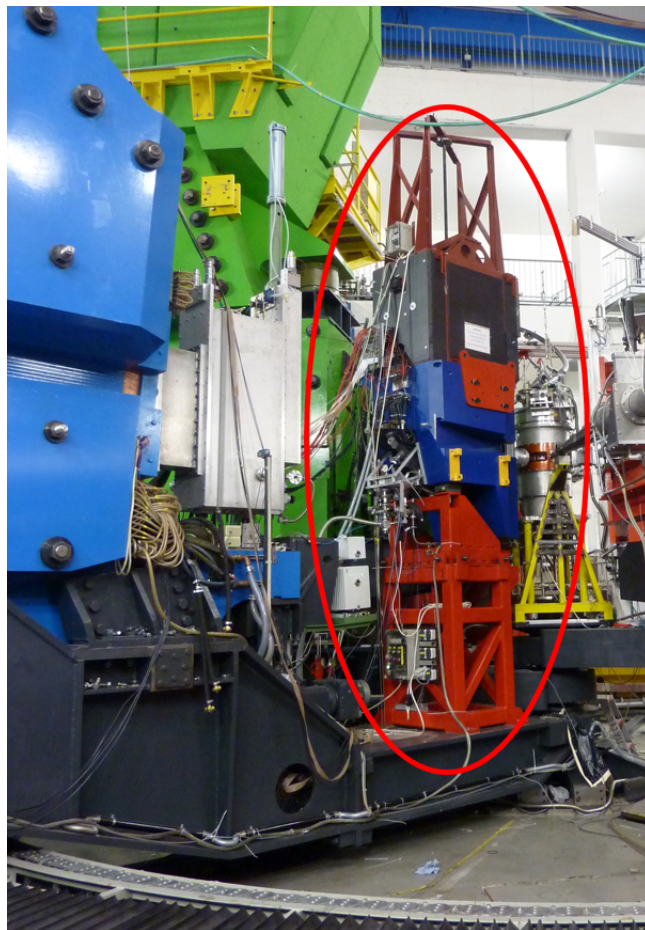
Figure 4.1 — Photo of a short-orbit spectrometer (inside a red ellipse) mounted in front spectrometer B (blue) on its support.

When SOS is used in an experiment, it is mounted in front of spectrometer B on its support, see Fig. 4.1. The current support is not designed for out-of-plane lifting

of the SOS [14]. Two options are available: 54 or 66 cm from the SOS magnet yoke to the target centre. For a given kinematic setting, when using the Rosenbluth method, it is important to cover a largest possible range of variation of the variable ϵ. To reach the large value of ϵ, the relative angle between SOS and spectrometer A has to be as small as possible. And to measure the small value of the ϵ, SOS has to be placed on the smallest possible forward angle. This range was maximized by milling off the SOS magnet yoke. At the distance of 66 cm from SOS to the target centre the smallest relative angle between SOS and spectrometers A and C is 55° and the smallest forward angle is 15.4°. The distance of 54 cm limits the forward angle to 22°, but allows larger solid angle acceptance.

4.2 Magnet

The magnet of the SOS spectrometer is an Browne-Buechner type dipole magnet [39]. The pole pieces have a circular form with uniform magnetic field radius of 350 mm. Maximal possible central momentum is 147 MeV/c for a magnetic field of 1.4 T. The momentum acceptance is interval from −13% to 16% [16].
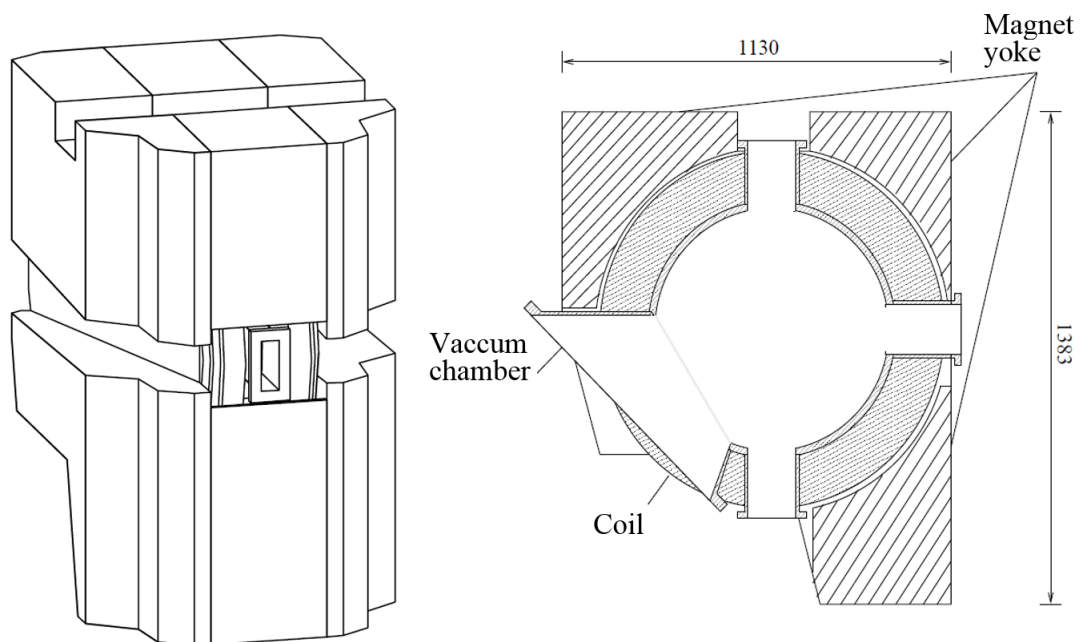
Figure 4.2 — Browne-Buechner type dipole magnet of the SOS. Figure from [40].

Altogether SOS has three focal planes. Two of them can be used for the particles which trajectories are deflected for +90° or −90° and which momenta do not exceed 150 MeV/c. One of these focal planes is located above, and the other one is located under the pole shoes. These two focal planes allow simultaneous detection of both

positive and negative charged particles. The third focal plane can be used for particles with momenta from 150 up to 300 MeV/c, which are then deflected with smaller angle. This focal plane is located in the rear lower part of the spectrometer. At the present only the upper focal plane is equipped with detectors.

The shape of the magnet yoke is shown on fig 4.2. The front side of the yoke was narrowed in order to minimize the angle relative to spectrometers A and C. The side recesses were made in height of the beam dump in order to access smaller forward angle. The impact of the milling of the yoke on the homogeneity of the magnetic field was first checked with a simulation. The maps of the magnetic field were measured after the milling, for several strengths of the field [12].
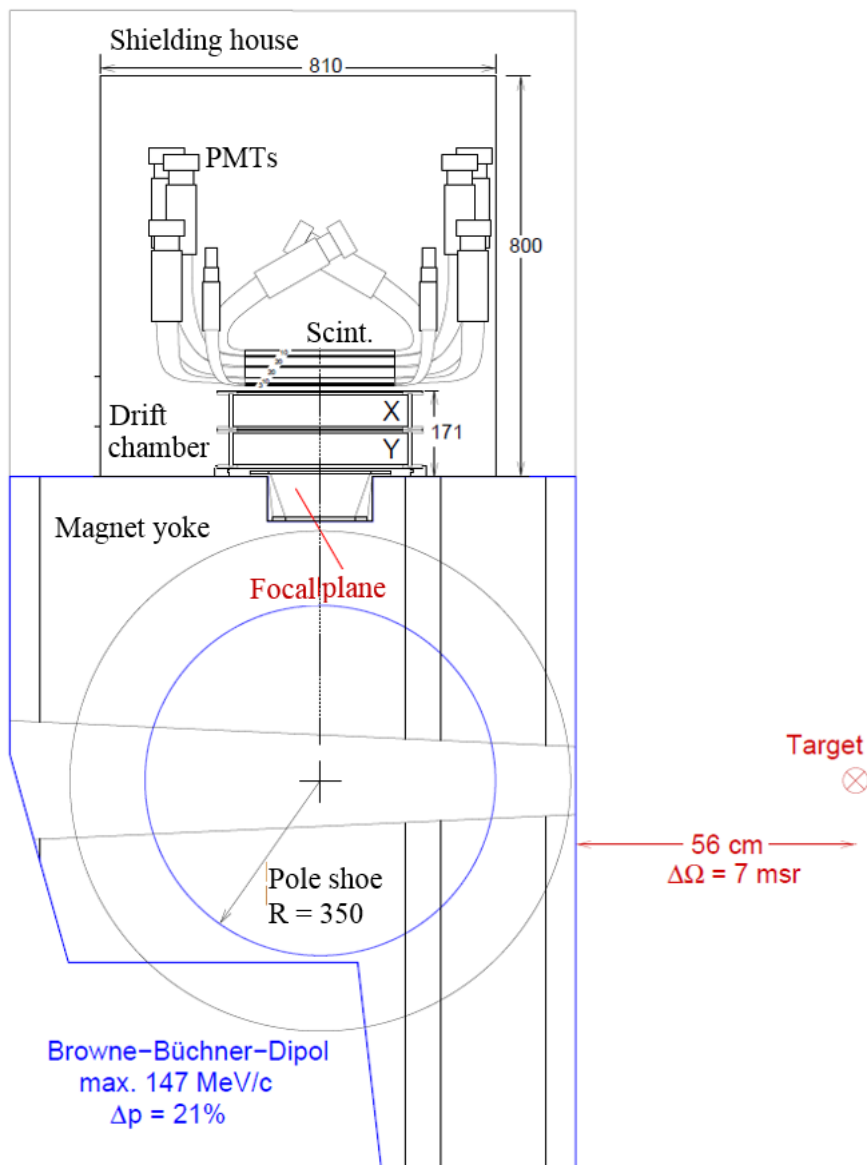
Figure 4.3 — Lateral profile of the SOS. The upper part of the figure shows the detector system inside a shielding house. The focal plane (red) of the dipole magnet (down, blue) is located under the detector system, it is tilted by about 50° with respect to the vertical. Figure from [16].

4.3   Detector system

The detector system of the SOS consists of two horizontal drift chambers and five layers of scintillators, Fig. 4.3. The drift chambers were designed, assembled and tested within the diploma and doctoral thesis of Matthias Ding [15, 16], and the scintillator range telescope was developed within the diploma work of Dagmar Baumann [14], assembled and tested as part of her doctoral thesis [12]. The detector system is placed inside a shielding house of borated polyethylene to block neutrons and lead to block other radiation.

4.3.1   Drift chambers

Contrary to the drift chambers of the spectrometers A, B and C, the drift chambers (Fig. 4.4 and table 4.1) of the SOS were developed for the trajectory determination of low-energy pions. As one of the SOS collimator do not exclude particles hitting the magnet walls, spatial and angular resolutions have to be as good as possible in order to be able to discriminate those particles. Such particles are excluded with the cut on reconstructed target coordinates.
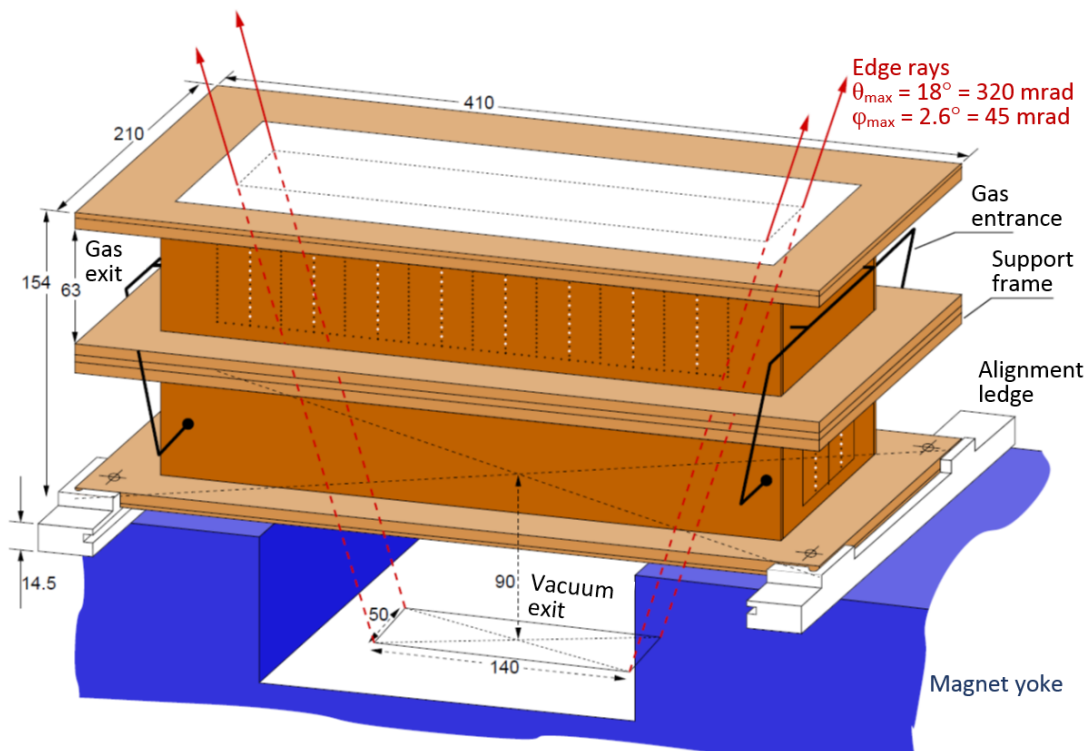
Figure 4.4 — The SOS drift chambers in a build-in position. The bottom chamber is used for reconstruction of non-dispersive coordinates, and the upper chamber for dispersive coordinates. Positions of the signal wires are marked with white points. Edge rays were determined with help of RAYTRACE simulation. Figure from [16].

Whenever a heavy charged particle passes through a material, it will lose energy and it can be deflected from its incident direction. For low-energy pions the energy loss is dominantly caused by inelastic collisions with atomic electrons and elastic scattering from nuclei, other effects (nuclear reactions, bremsstrahlung) can be neglected [41]. The small angle deflection is mostly caused by Coulomb scattering from nuclei. Since this process happens many times it is called multiple Coulomb scattering and it worsens the spatial and angular resolutions. For the pions with kinetic energy less than 30 MeV, the standard deviation of scattering angle σ_θ can be written as:

$$
\begin{aligned}
\sigma_\theta &= 13.6 MeV \cdot \frac{E}{p^2 c^2} \sqrt{\frac{x}{X_0}} \{1 + 0.038 \ln \frac{x}{X_0}\} \\
&\propto 1/E_{kin} \quad for \quad E_{kin} \ll m_\pi
\end{aligned}
\tag{4.2}
$$

where E is the energy and p is the momentum of the pion, $\frac{x}{X_0}$ is the thickness of the scattering material in radiation length [13, 16]. The standard deviation of scattering angle increases with loss of kinetic energy as the pion passes through material. Therefore, to achieve the best possible spatial and angular resolutions, the energy loss has to be minimized with the selection of a gas and a chamber foil material with appropriate radiation length. It is known that materials with small atomic number Z have large radiation lengths. Hence, helium was chosen as a counting gas because of small Z and ethane as a quencher because of its better performance than methane at necessary high voltage. Due to almost constant value of the drift velocity (4 cm/µs for broad range around the working electric field value ≈ 3 kV/cm), mixture with ratio 1 : 1 is used in measurement [16]. Before entering the chamber, gas mixture is enriched with the ethanol, in order to prevent the aging effects of the wires.

Table 4.1 — Properties of the SOS drift chambers. Adapted from [16].

Outer dimensions of the double chamber	410 x 210 x 156 mm^3
Active surface	294.4 x 73.6 mm^2
Drift cell length x width	18.4 x 5.08 mm^2
Horizontal offset of the signal wires	± 100 µm
Number of signal wires in X-/Y-chamber	64/16
Number of potential wires in X-/Y-chamber	355/103
Signal wires: $\varnothing$ 15 µm Au-coated Tungsten-Rhenium	
Potential wires: $\varnothing$ 80 µm Ag-coated Aluminium	
Gas: 50% Helium + 50% Ethan	

Due to SOS compact design, the focal plane (4.3) of the SOS magnet lies inside the influence of the magnetic fringe fields. Because of that, a drift chamber can not be placed in the focal plane as it was done for x1 wire layer in spectrometers A, B and C [9]. Under these circumstances decision was made to use a volume drift chamber. As
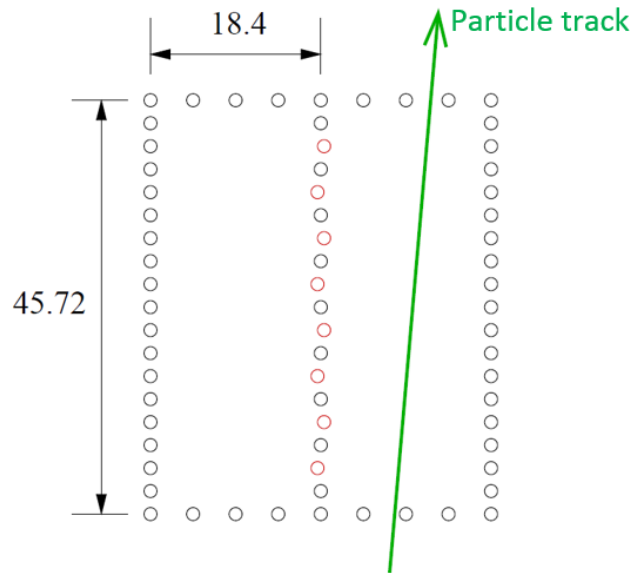
Figure 4.5 — Lateral profile of the SOS drift cell. Black profiles represent potential wires and the red ones represent signal wires, which are alternating shifted left and right. In order to make the signal wire shifts visible on this figure, they are exaggerated. Figure form [16].

shown in a Fig. 4.5, the particle trajectory is determined in a drift cell, which consists of eight vertically arranged signal wires. Potential wires are placed between signal wires and they also define the boundaries of the drift cell forming the shape of the electric field inside the cell. The signal wires are not placed on a straight line above each other, they are alternating shifted left and right for 100 μm in order to distinguish, if the particle has passed the signal wire on the left or on the right side. Each of the two drift chambers measures only one spatial coordinate and one angle. The first chamber from the magnet is the Y-chamber and it measures the non-dispersive coordinate y_{ch} and the non-dispersive angle ϕ_{ch}. The Y-chamber consists of 2 drift cells. The second chamber is the X-chamber. It has 8 drift cells, which are perpendicular to the 2 cells of the Y-chamber. The X-chamber measures the dispersive coordinate x_{ch} and the dispersive angle θ_{ch}. These two chambers are separated only with a grounded foil, thus preventing mixing of electric fields at the junction of the two chambers. Due to multiple scattering, the resolution of the X-chamber will be lower in comparison with the Y-chamber. Since a good vertex resolution is important to discriminate particles scattered at the magnet edges and to estimate energy loss when using round target, priority was given to Y-chamber.

4.3.2 Scintillator range telescope

A range telescope consists of five layers of plastic scintillators (type Bicron BC 408). The width and the length of each layer are 80 mm and 300 mm, respectively. How-

ever, layers differ in thickness, so that in direction of particles passage thickness of the layer is respectively 3, 10, 20, 20 and 10 mm, see Fig. 4.6. In data acquisition and analysis programs the layers are labelled as 0, 1, 2, 3, and 4 respectively. Read-out of the scintillators is performed in coincidence of both lateral sides, in order to suppress background signals. To minimize loss of light, PMTs with window area similar to the area of the scintillator readout surface were chosen. For the thinnest bottom layer only one PMT Philips XP 2910 is used, and for the four upper layers Philips XP 2262B PMTs are used.
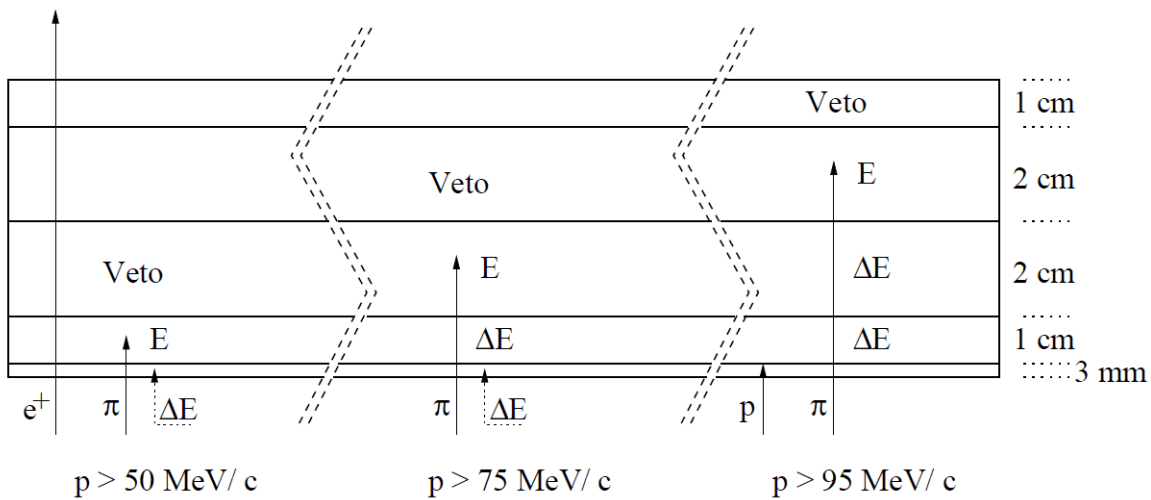
Figure 4.6 — Illustration of the particle identification in the scintillator range telescope. Protons are stopped in the bottom scintillator, positrons pass through all layers, pions are stopped in a certain layer depending one their momentum. In order to enter the second scintillator the pions need to have momenta larger than 50 MeV/c and so on [12].

Light from the scintillators is directed to the PMTs through a light guide made out of Plexiglas. The light guide is made out of individual strips which were glued together after the bending (so-called "twisted-strip"). In this case it is important that all strips have same length, to ensure that light from every single strip arrives to the PMT at the same time. But, because of lack of space and in order not to cross the critical bending radius, the lengths of the strips differ less than 2 cm in length. That is still acceptable. The light guides are glued to the scintillators with optical cement Bicron BC-600 and to the PMTs with silicon glue Wackler Elastosil in order to easily replace a defect PMT. The PMTs were mounted on aluminium holding frame and protected from the influence of magnetic field with μ-metal shield.

Foils of the chambers are not completely helium leak-proof. Little amount of helium gas will always diffuse into volume of the shielding house, and from there it can also diffuse into PMTs. In order to protect the PMTs from the helium contamination the volume of the shielding house is separated with plastic plates in the chamber part and in the scintillator part. The chamber part and the upper rear wall of the shielding

house are connected with an exhaust tube, and a ventilator at the end of the exhaust tube under-pressurizes the chamber part, preventing the diffusion of the helium gas into the scintillator part of the shielding house.

The role of the range telescope is to provide timing signals (the trigger signal and the common stop signal for the SOS drift chambers) and to measure the range and energy loss of the through going particle. This way it makes it possible to differentiate between the pion signal and the proton and positron background, see Fig. 4.6.

4.4 Collimators

The collimators of a spectrometer have multiple tasks. The size of the aperture defines the magnitude of the solid angle acceptance. Furthermore, it allows only these particles to enter the spectrometer, which will not be scattered by internal components of the spectrometer.

In the case of the point target and a given collimator, the reduction of the the distance between the spectrometer and the target will cause an increase of the solid angle acceptance. However, for an extended target, in the same situation, another effect increases too: not only particles from electroproduction enter spectrometers, but also particles which were scattered inside the extended target. Therefore, the size of aperture and the distance to the target has to be optimized to maximize the solid angle acceptance and to minimize the amount of internal scattered particles.

One collimator was designed to be used when SOS is mounted at 66 cm from the target centre. In the development of this collimator special attention was given to the fact that when using a target cell with diameter of 2 cm, all particle trajectories will undisturbed pass throughout the magnet. The solid angle of this collimator is 1.8 msr [12].

For some kinematic settings it is not essential to reach the smallest possible forward angle and the smallest relative angle between the spectrometers. Therefore, SOS can be placed closer to the target. Two benefits arise from this fact. Firstly, the particle trajectory length is shorter, leading to smaller muon contamination. And additionally, the solid angle is larger, thus more particles will enter the spectrometer and measurement time can be reduced. Distance of 54 cm from the SOS and the target centre was considered to be an optimal solution. But the development of the appropriate collimator, which would exclude particles hitting the magnet poles, was not possible and this has to be taken into account during the analysis. The solid angle of the collimator aperture is 7 msr, but the magnet allows approximately 4 msr [12].

The third collimator is a sieve collimator, which is used for a (inverse) transfer matrix determination. It consist of a metal plate with an irregular array of holes. The full coverage of the aperture edges of the two above mentioned collimators is achieved by placing the sieve collimator at two different positions. In those two positions none of the holes cover each other, so that the number of coordinates used in determination of the transfer matrix is doubled. In the target coordinate system (the z-axis points to the spectrometer, the x-axis points to the floor) positions of the holes are defined by the dispersive angle θ_0 and the non-dispersive angle ϕ_0. Additionally, in the dispersive xz-plane we also have the difference from the central momentum $\delta p_0 = \Delta p / p$ and in the non-dispersive yz-plane we have the vertex coordinate y_0 in direction of the beam. By using the drift chamber measurements, the position of each hole can be determined and mapped in terms of the chamber coordinates $(\theta_{ch}, x_{ch}, \phi_{ch}, y_{ch})$. Now it is possible to write the dispersive target coordinates θ_0 and δp_0 as functions of the dispersive chamber coordinates (θ_{ch}, x_{ch}) and the non-dispersive target coordinates ϕ_0 and y_0 as functions of (ϕ_{ch}, y_{ch}). The coefficients of these functions form the transfer matrix.

Each collimator is made of tungsten-cooper alloy ("Densimet 18" by Plansee). The sieve collimator is 5 mm thick and the other two collimators are 45 mm thick.

4.5 Trigger electronics and data acquisition

The SOS uses similar electronics and has a similar trigger logic system as the standard magnetic spectrometers of A1 collaboration. The trigger signal is generated if a signal in a scintillator layer is larger than a specified threshold. The individual trigger signals can be put in a different logical condition. When the SOS is used in a coincidence experiment with another spectrometer, it replaces the spectrometer B in the universal logic module.

5

The Experiment

The experiment took place from April, 19 to May, 2 2011, and was performed on the basis of the proposal $A1 - 1/98$ [40]. This proposal planned a measurement of the $p(e, e'\pi^+)n$ reaction at $Q^2 = 0.035, 0.078$ and $0.156 \, (\text{GeV}/c)^2$ and $W = 1084 \, \text{MeV}$, which is only about 5 MeV above the threshold for charged pion electroproduction. The requested time for this experiment was only enough to measure one four-momentum transfer value. A decision was made to measure at $Q^2 = 0.078 \, (\text{GeV}/c)^2$. Contrary to the proposal $A1 - 1/98$, the invariant mass in this experiment was chosen to be $W = 1094 \, \text{MeV}$, because the SOS was a relatively new spectrometer at this time and no complete analysis of the pion electroproduction data had been done before. For these W and Q^2 values, the momentum of the pion in the parallel kinematics was 113 MeV/c. In order to perform a good longitudinal-transverse separation via the Rosenbluth method, it is important to have a lever arm in ϵ as large as possible. The boundary ϵ values are limited by angles accessible to the spectrometers. In this experiment the upper ϵ value was 0.897 and the lower $\epsilon = 0.306$. The third $\epsilon = 0.591$ was in between these boundaries. For the determination of the longitudinal-transversal interference term, two measurements were performed for $\epsilon = 0.897$ at $\pm 18.7°$ offset with respect to the virtual photon direction. Before the end of the beam time, the highest ϵ setting in parallel kinematics was measured again to have a reference point between the start and the end of the experiment. The short control measurements of the elastic electron scattering from liquid hydrogen target were performed with the spectrometer A to monitor its performance during the experiment.

The kinematical settings listed in table 5.1 are taken in the following order: axialFF_987, axialFF_306, axialFF_591, axialFF_987L, axialFF_987R and axialFF_987a. After each of the first three kinematics two elastic electron scattering settings were measured in the order as listed in table 5.2.

Table 5.1 — Summarized details of the kinematical settings: starting with name of the setting, E is the energy of the beam, E' is the energy of the scattered electron, θ_e is the angle of scattered electron, ϵ is the transversal polarization of the virtual photon, p_π is the momentum of the pion, $\theta_\pi^\star$ is the pion production angle in the centre-of-mass frame and θ_π is the pion production angle in the laboratory frame.

Setting	E (MeV)	E' (MeV)	θ_e (°)	ϵ	p_π (MeV/c)	$\theta_\pi^\star$ (°)	θ_π (°)
axialFF_987	855	644.8	22.5	0.8970			42.94
axialFF_306	345	134.8	80.7	0.3065	113	0	22.40
axialFF_591	450	239.8	50.3	0.5913			31.79
axialFF_987a	855	644.8	22.5	0.8970			42.94
axialFF_987L	855	644.8	22.5	0.8970	110	+18.7	32.8
axialFF_987R						-18.7	53.1

Table 5.2 — Summarized details of the kinematical settings for elastic electron scattering measured with spectrometer A: starting with the name of the setting, E is the beam energy, E' is the energy of the scattered electron and θ_e is the angle of the scattered electron.

Setting	E (MeV)	E' (MeV)	θ_e (°)
elastic_855a	855	644.65	48
elastic_855b			52
elastic_345a	354	266	80.7
elastic_345b		261	
elastic_450a	450	386	50.3
elastic_450b		381	
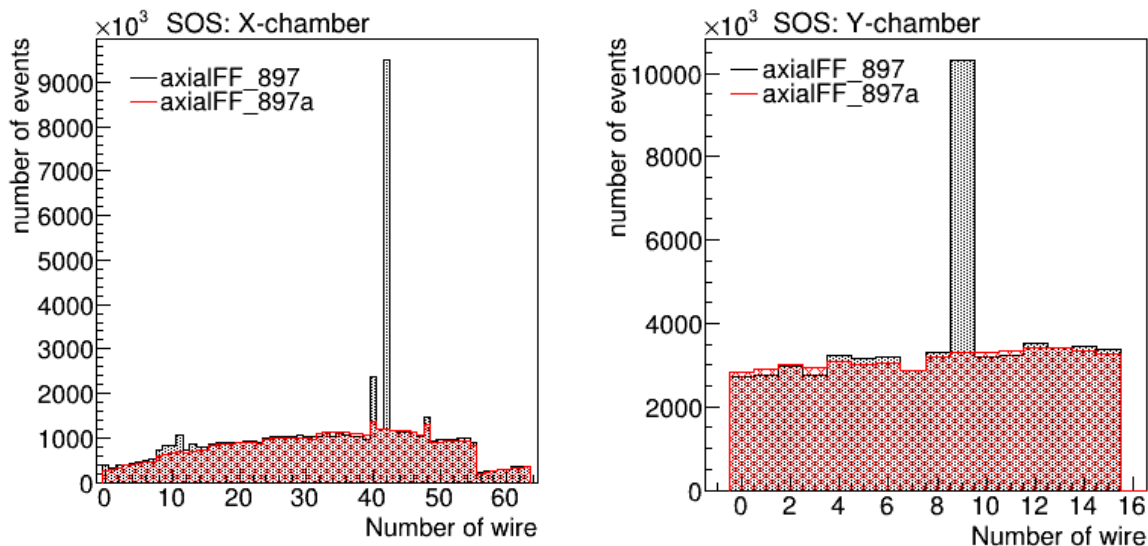
Figure 5.1 — The number of wires histogram for the SOS X-chamber (left) and the Y-chamber (right). The data of the axialFF_987 setting is shaded grey and the data belonging to the axialFF_987a setting is shaded red. In both chambers for the axialFF_987 setting noisy wires can be observed.

During the data analysis, which will be described in detail in the following chapter, a big mismatch between the axialFF_987 and the axialFF_987a cross section was obtained. After an inspection of the relevant histograms, some discrepancies in histograms of the SOS chambers were found. The Fig. 5.1 shows the "Number of wires" histograms for both chambers. Each bin of these histograms corresponds to a particular signal wire of the SOS drift chambers. The axialFF_987 data, shaded grey, contain noisy wires (40, 42, and 48 for the X-chamber and the wire 9 for the Y-chamber) in comparison with the data belonging to the axialFF_987a setting, shaded red. The unexplained data in noisy bins causes a loss of events, which can easily be seen on the Fig. 5.2.
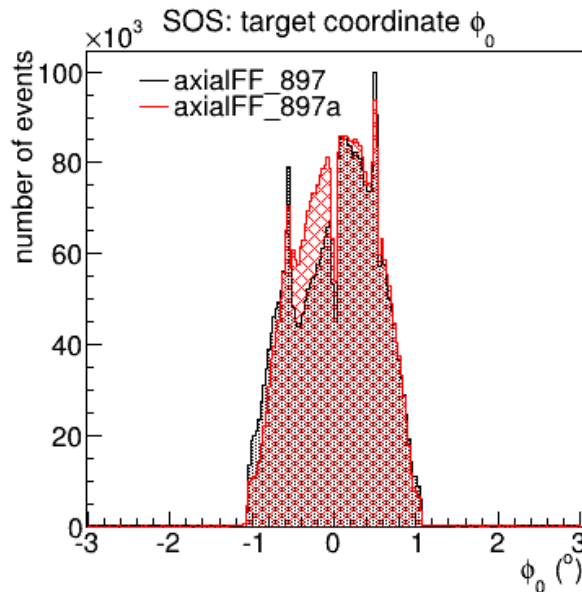
Figure 5.2 — The SOS ϕ_0 target coordinate histogram, raw events. The data of the axialFF_987a setting is shaded red and the data belonging to the axialFF_987 setting is shaded grey. The missing events in the axialFF_987a data are due to the malfunctioning TDC module.

A big effort was invested, to solve this problem somehow. Similar to spectrometer A VDCs, a possibility to exclude a chamber wire from the analysis was added also to the SOS chamber system. But the exclusion of noisy wires from the analysis did not help. After the detailed checking of the logbook, we found that at the end of the axialFF_987 setting two TDC 2001 modules were replaced by properly working ones. The replaced TDC modules were part of the SOS drift chamber electronics. After the replacement, no more issues referring to the SOS TDC modules were reported in the logbook and the raw histograms of the SOS chambers no longer showed anomalies. It seems that, the problematic modules were not working properly during the measurement of the axialFF_987 setting, causing the loss of some data. Therefore, the axialFF_987 setting was thrown out from the further analysis.

<div style="text-align: right; font-size: 4em; color: #999;">6</div>

Data Analysis

In this chapter we present the analysis of the data for the $p(e,e'\pi^+)n$ reaction, measured at $Q^2 = 0.078$ (GeV/c)^2 and $W = 1094$ MeV. We will start the chapter with the definition of the experimental cross section. Then we will continue with an introduction of methods for a separation of the relevant data from the background events, which were also registered during the measurement. The relevant data have to be corrected for the total efficiency of the setup and for the pion decay. Some of the background (muon contamination) cannot be removed with the experimentally obtained quantities, it needs to be determined via simulation instead. The total error of the measurement is dominated by the total systematic error, which has many contributions. Each contribution will be determined separately. At the end of the chapter we will briefly present the results of the elastic control measurements with spectrometer A.

6.1 The $p(e,e'\pi^+)n$ cross section

The experimental cross section for the $p(e,e'\pi^+)n$ reaction is defined with:

$$\frac{d\sigma}{d\Omega_\pi} = \frac{N_{mm} - (f_W \cdot N_{back})}{L \cdot \Phi} \cdot K_{decay} \cdot K_{muon} \cdot \epsilon_{total} \tag{6.1}$$

N_{mm} is the number of events in the missing mass peak, N_{back} is the number of events in the corresponding background spectrum, f_W is the weight factor for the background subtraction (this is a ratio of the coincidence time cut width and the width of the random background cut in the coincidence time histogram). The numerator in 6.1 represents the number of determined true events. L is the integrated luminosity corrected for a dead time, Φ is the accepted phase space, K_{decay} is the pion decay correction factor, K_{muon} is the muon contamination correction factor and ϵ_{total} is the total efficiency correction factor. Mentioned quantities will be defined and explained in the text below.

6.1.1 Coincidence time

The difference between times of flight of a particle in one spectrometer and a particle in the other spectrometer, which originate from the same reaction, can be used for separating the true coincidence events from the random coincidences (background). The time difference is measured by the coincidence TDC. The event in the scintillator ToF plane of the spectrometer A gives a start signal and the event in SOS second scintillator gives a stop signal to the TDC module. The principle is the following: if the scattered electron and the produced pion belong to the same $p(e, e'\pi^+)n$ reaction their time of flight difference should have a constant value. For all other uncorrelated events the values of the time of flight differences should be equally distributed inside the width of the TDC's coincidence gate. The raw coincidence time histogram from the coincidence TDC module can be seen on Fig. 6.1.
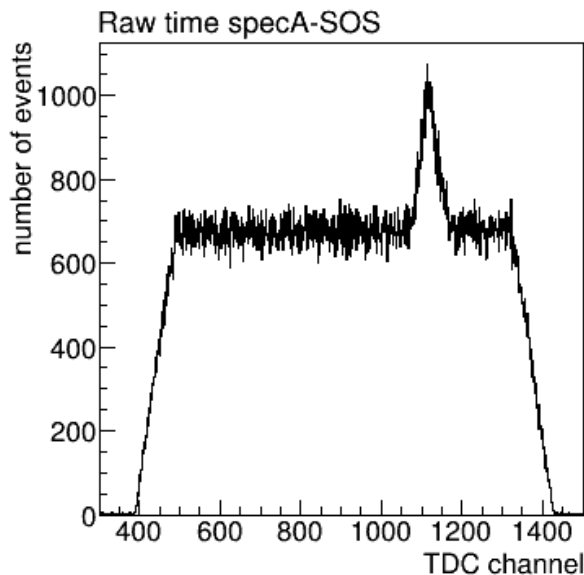
Figure 6.1 — The raw coincidence time TDC histogram for the axialFF_591 kinematics. The channel width is 100 ps. The width of the distribution corresponds to the width of the coincidence gate, which is around 100 ns. The FWHM of the raw coincidence peak is 14.4 ns.

The width of the raw coincidence time peak is very large and the true events are only inside the coincidence time peak which is lying on a background of random coincidences. A better time resolution would allow a narrower cut on the coincidence time peak and consequently less random coincidence events would be taken into the further analysis. The time resolution can be improved by following software corrections.

Since the spectrometers accept particles within a certain momentum and angular range, the trajectory length and the velocity of those particles will differ and consequently their time of flights will differ too. These time differences are causing a broad-

ening of the raw coincidence time peak. For example, in spectrometer A the trajectory length differences with respect to the central trajectory can be in the range of ± 1.5 m. Using the drift chamber data the trajectory and the momentum of the particle can be reconstructed. Using this information it is possible to calculate the time of flight and correct the raw coincidence time spectrum with the time difference relative to the central trajectory. The same procedure can also be done for the SOS.
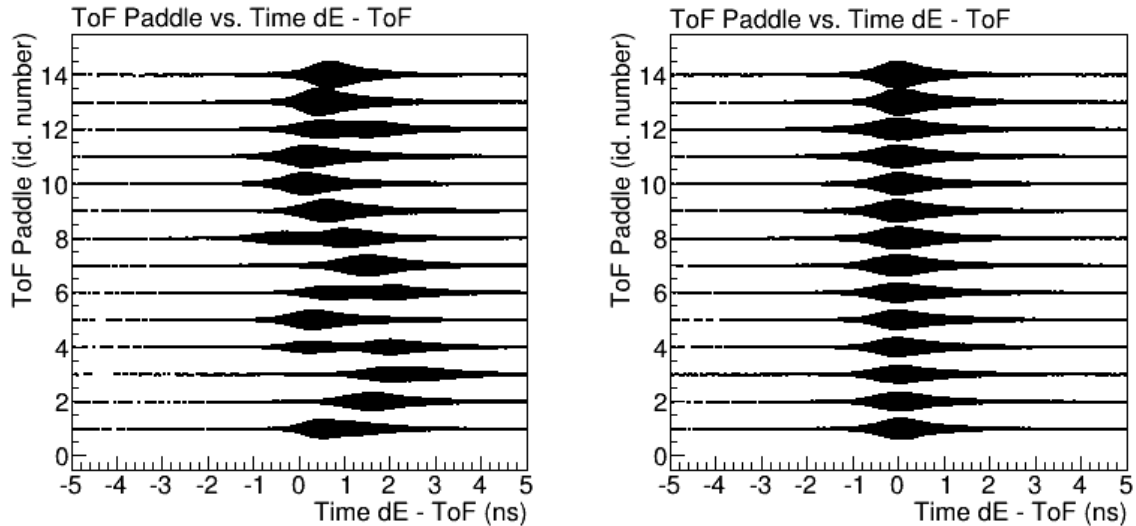
Figure 6.2 — The ToF scintillator paddles vs. time difference $dE - ToF$ in spectrometer A, without the time offset correction (left) and with the time offset correction (right). After the correction, signals in the dE paddles and the corresponding ToF paddles "seem" as if they are produced at the same time, since the time differences are centred at bin 0.

The scintillator planes in spectrometer A are segmented. The scintillator segments are equipped with PMTs which have somewhat different cable lengths. This fact can be counteracted by implementing different time offsets for each scintillator bar, as shown on Fig. 6.2.

After corrections, the time resolution of the coincidence peak is now reduced to only 2.8 ns (FWHM), Fig. 6.3. This is the intrinsic time resolution of the setup, which includes the cumulative contributions from the statistical processes in the scintillators, the PMTs and the effects in detector electronics.

The improvement of the coincidence time resolution is essential to keep the ratio between the true and the random coincidences as high as possible. With a better time resolution, this ratio is higher and a better separation between the true and the random coincidences can be achieved. This is especially important in a measurement of a reaction with a small cross section. If this would not be fulfilled, the desired reaction could not be reliably isolated from the background events. As we shall see, the narrow cut on the coincidence peak enables us to make an accurate separation between the true and the random coincidences. Of course, the random coincidence evens which
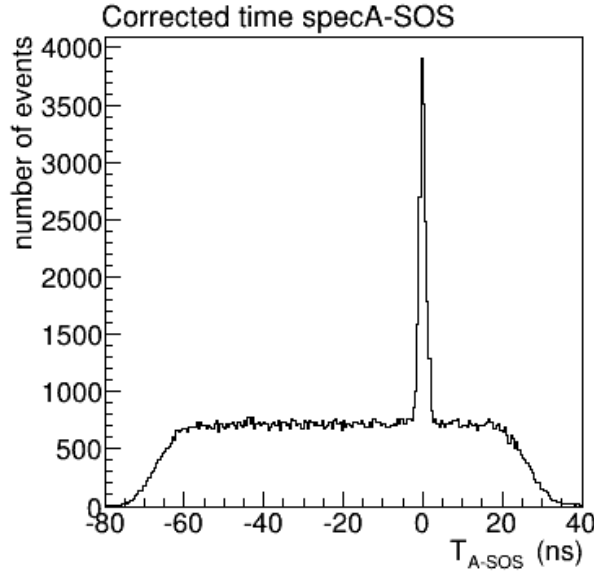
Figure 6.3 — The corrected coincidence time spectrum, the axialFF_591 setting. The FWHM of the coincidence peak is 2.8 ns.

are located below the coincidence peak can not be separated by a simple cut in the time histogram. It is assumed, that the random coincidences are uniformly distributed in the coincidence time histogram. Therefore, they can be subtracted.

6.1.2 Missing mass

Another way to identify the true coincidences is a missing mass spectrum. In reactions such as $p(e, e'\pi^+)n$, four-momenta of the scattered electron e' and the produced charged pion π^+ are measured, but the four-momentum of the produced neutron n is not measured. Hence, the term "missing" refers to the observables of the particle which is not detected. Following the naming convention from the chapter 2, the momentum and the energy conservation laws for the $p(e, e'\pi^+)n$ reaction can be written as:

$$\vec{k}_i + \vec{P}_i = \vec{k}_f + \vec{k}_\pi + \vec{P}_{miss}$$
$$\epsilon_i + E_i = \epsilon_f + \omega_\pi + E_{miss}$$

(6.2)

If we assume the case of the stationary target $\vec{P}_i = 0$, the missing momentum $\vec{P}_{miss}$ and the missing energy E_{miss} can be written as:

$$\vec{P}_{miss} = \vec{k}_i - \vec{k}_f - \vec{k}_\pi = \vec{q} - \vec{k}_\pi$$
$$E_{miss} = \epsilon_i + m_p - \epsilon_f - \omega_\pi = \omega + m_p - \omega_\pi$$

(6.3)

The four-momentum of the missing particle, or in this case of the neutron, is now completely determined by the observables of the measured particles (e' and π^+):

$$P_{miss} = (E_{miss}, \vec{P}_{miss}) = (\omega + m_p - \omega_\pi, \vec{q} - \vec{k}_\pi) \qquad (6.4)$$

Finally, the missing mass m_{miss} is now:

$$m_{miss} = \sqrt{(E^2_{miss} - \vec{P}^2_{miss})} \qquad (6.5)$$

To conclude, if we measure the scattered electron e' and the charged pion π^+ which originate from the same reaction, the mass of the missing particle, which is calculated from these data, should be the mass of a neutron.
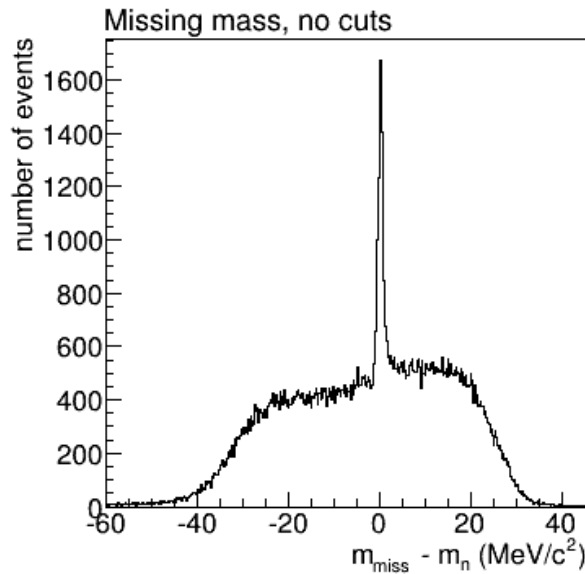
Figure 6.4 — The missing mass spectrum for the axialFF_591 setting, no cut on the coincidence time.

If we calculate missing masses for all events which were registered as coincidences, we will obtain the so-called missing mass spectrum. Additionally, the neutron mass is subtracted for each event and the neutron peak is then centred around the bin 0. From now on, wherever the missing mass spectrum will be mentioned, one refers to the spectrum from which the neutron mass was subtracted. This has practical reasons, because it is easier to detect a possible position shift of the missing mass peak with respect to the bin 0, than with respect to the bin corresponding to the neutron mass (939.565 MeV/c^2). Fig. 6.4 shows the missing mass spectrum of the axialFF_591 kinematics without the cut on the coincidence time. The signal to background ratio is about $13 : 4$.
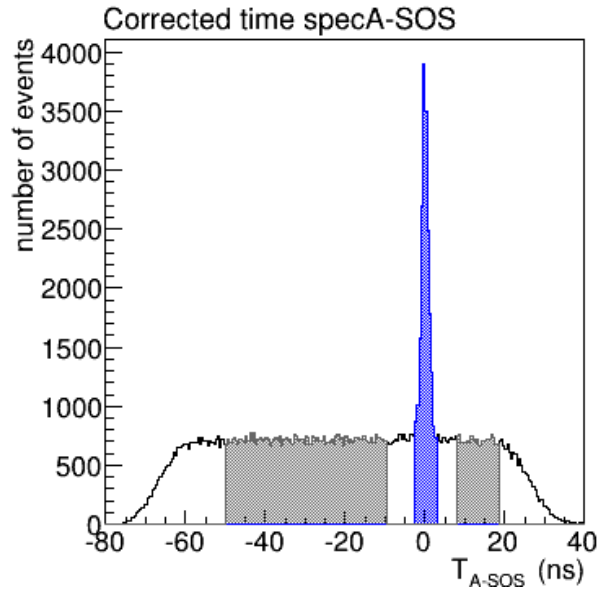
Figure 6.5 — The axialFF_591 corrected coincidence time histogram. The cut on the coincidence peak $(-2.0 \text{ ns} \leq T_{A-SOS} \leq 2.5 \text{ ns})$ is shaded blue. The cut on the random background $(-50.0 \text{ ns} \leq T_{A-SOS} \leq -10 \text{ ns})$ and $(7.0 \text{ ns} \leq T_{A-SOS} \leq 18.0 \text{ ns})$ is shaded grey.
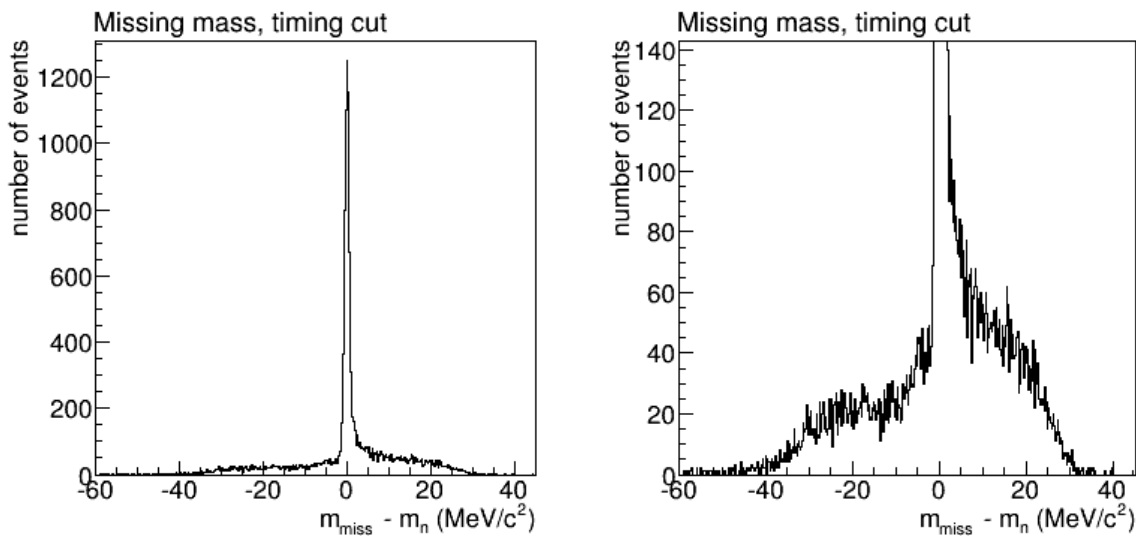
Figure 6.6 — The missing mass spectrum for the axialFF_591 setting with the cut on the coincidence peak. The left figure shows the full data range. The right figure shows the same spectrum, but zoomed.

If a cut on the coincidence peak is applied, Fig. 6.5, this ratio is improved significantly. The background under the missing mass peak is reduced approximately by the factor 10, see Fig. 6.6. The goal of the analysis at this point is a further reduction of the residual background (random coincidences) by imposing cuts on different observables. But it is important that those cuts do not remove the true events. The background which remains after this procedure should finally be subtracted.

Earlier in the text we have assumed that the events outside of the coincidence time peak do not contain any true events. This can be verified by producing a missing mass histogram only out of random coincidence events. Fig. 6.7 shows the missing mass distribution of two random coincidence intervals: -50.0 ns $\leq T_{A-SOS} \leq -10$ ns and 7.0 ns $\leq T_{A-SOS} \leq 18.0$ ns (see Fig. 6.5). Since the missing mass peak does not show up in the obtained missing mass distribution, it is clear that both random coincidence intervals do not have any true events.
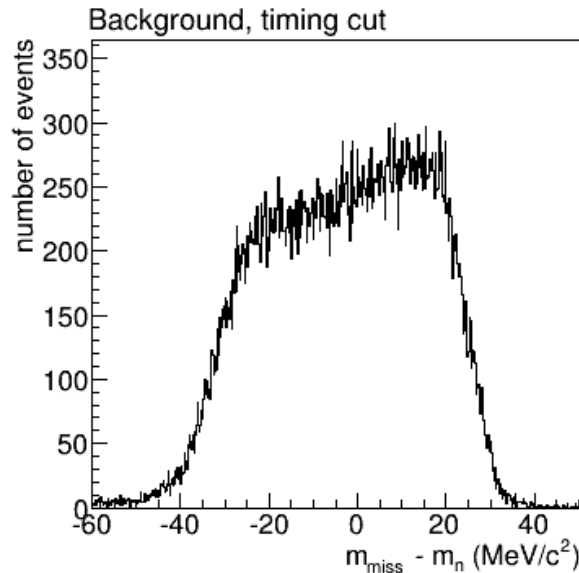
Figure 6.7 — The missing mass spectrum for the axialFF_591 setting with the timing cut on the random background.

6.1.3   Background subtraction

As mentioned before, not all of the random coincidence background can be excluded with applied cuts. One part of random event pairs has such combinations of observable values, that their calculated missing mass is placed lower than the left edge of the missing mass peak. And this part of the random coincidences can be removed by the cut on the left side of the missing mass peak. But some combinations of observable values will produce missing masses, whose values will be placed beneath the missing mass peak of the true events.

The amount of random coincidence events beneath the missing mass peak can be determined by a cut on the uniform part of the coincidence time spectrum, Fig. 6.5. The random coincidence events from both sides of the coincidence time peak are used to produce a background missing mass histogram. For all kinematical settings the total width of the cut on random coincidences was 51 ns. The missing mass peak consist-

ing of the true events and of the residual background is obtained from the 4.5 ns wide cut on the coincidence time peak. The widths of the cuts differ and the corresponding missing mass histograms contain different amounts of the background (random coincidence) events. Hence, the background missing mass histogram has to be normalized with the $f_W = 4.5/51$ weight factor. The resulting histogram can then be subtracted from the coincidence missing mass histogram.
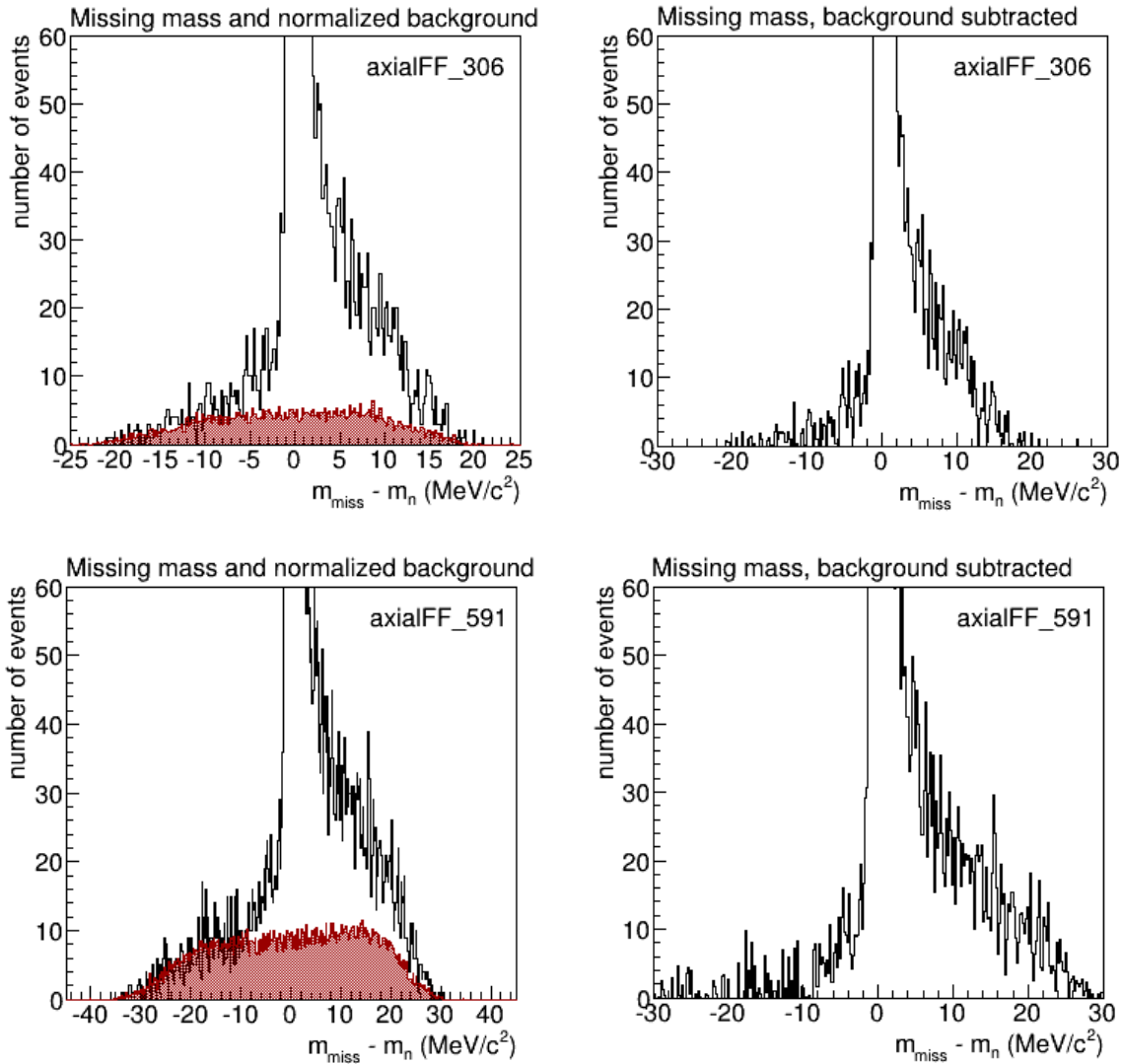
Figure 6.8 — The missing mass distributions for the timing cut (black) and the corresponding normalized background (red) are shown on the left side and the result of the background subtraction is shown on the right side for a given value of the virtual photon polarization ϵ.

The missing mass histograms with the cut on the coincidence time peak (black), the corresponding normalized backgrounds (red) and the results of the background subtraction for the axialFF_306, axialFF_591 and axialFF_897a setting are presented on the Fig. 6.8 and 6.9. For a particular kinematical setting the black and the red missing mass distributions have the same width. The width of the distributions increases with

increasing of the virtual photon polarization ϵ. The corresponding histograms for the axialFF_897R and axialFF_897L setting are not shown since they are very similar to the histograms of the axialFF_897a setting.
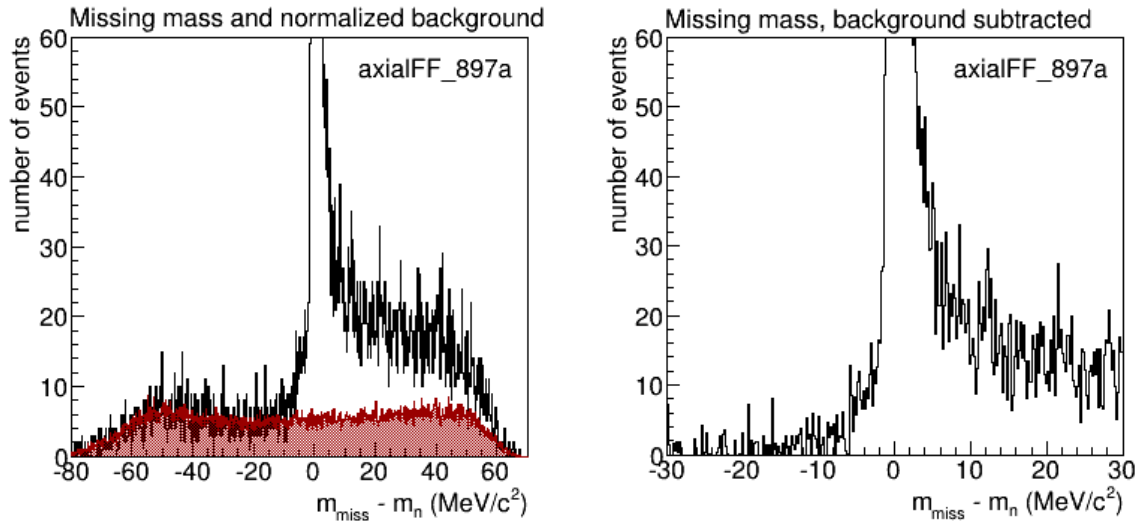
Figure 6.9 — The missing mass distributions for the timing cut (black) and corresponding normalized background (red) are shown on the left side and the result of the background subtraction is shown on the right side a given value of the virtual photon polarization ϵ.

6.1.4   Radiation loss corrections

As can be seen, the missing mass spectrum has an asymmetric form with a gauss-like left edge and a slow falling right edge. The right edge is called radiative tail, due to radiation losses. There are two processes involved in these losses: the external and the internal bremsstrahlung.

The internal bremsstrahlung or the Schwinger radiation is a process in which the electrons radiate real or virtual photons in the vicinity of the target proton/protons. In case of $p(e, e'\pi^+)n$ reaction, this process gives the largest contribution to the radiation losses. The external bremsstrahlung includes all processes in which charged particles emit photons either before or after reaction in the field of other nuclei. The probability that the bremsstrahlung will occur is inversely proportional to the square of the particle mass. In case of charged pions this effect is negligible and it only needs to be taken into account for electrons. Since the bremsstrahlung photons are not directly measured the individual data events can not be corrected for the radiation losses. Instead, the radiative processes are modelled via computer simulation to obtain a good agreement with the measurement. The procedure is in detail explained in [10] appendix D.

6.1.5 Energy loss corrections

Without energy loss corrections the actual missing mass peak would be displaced to the positive values, instead of being centred around the bin 0. This occurs because of the energy loss of the reaction products when they travel through the target material, target walls, snow on the target walls, air between the scattering chamber and the spectrometer entrance, different foils and drift chamber gas. Consequently, the reconstructed particle energy is lower than the particle energy at the site of their production. All energy loss corrections are done via software, and most of them are done automatically, except the correction due of the snow on the target walls. Although the target chamber is held under a high vacuum at all times, the snow made out of residual atmosphere gases (nitrogen, oxygen, carbon dioxide, and water) will be formed on the target walls, due to low temperature of the cryogenic target and the walls (around 22 K). The thickness of the snow may vary with the time and the amount of the energy loss correction due to snow has to be accordingly adjusted. This will be demonstrated in section 6.1.8.2.

6.1.6 Luminosity

The integrated luminosity L is defined as a product of two quantities; the surface density of the target nuclei N_T and the number of electrons N_e which are hitting the target during the time T:

$$L = N_T N_e \tag{6.6}$$

The N_e can be calculated from the beam current measurement in the following way:

$$N_e = \frac{1}{e} \int_0^T I(t) dt \tag{6.7}$$

where e is the unite charge, T is the duration of the measurement, $I(t)$ is the beam current. In this experiment the beam current $I(t)$ was measured with a Förster probe (fluxgate magnetometer), which is made out of two toroidal coils. The beam passes through the coils and its current creates a magnetic flux in their ferrite cores. This causes an offset to their hysteresis curve which is measured by an AC current signal running through the coils. The magnitude of the signal is proportional to the beam current. The probe is installed inside the acceleration section of the third RTM and all recirculations of the beam will contribute to the induced signal. Therefore, if one measurement of the current above 10 µA has an uncertainty of 0.3 µA, with n recirculations the uncertainty of the probe will be $0.3/n$ µA. The probe also has a second measurement range for smaller currents, but the switching has to be done by hand.

The surface density of the target nuclei N_T can be calculated from:

$$N_T = \frac{\rho \bar{x} N_A}{M} \tag{6.8}$$

where ρ is the density of the target material, $\bar{x}$ is the average target length, N_A is Avogadro constant and M is the molar mass of the hydrogen atom. In some literature M denotes the molar mass of the hydrogen molecule H_2. In this case, the above formula has to be multiplied by a factor 2.

A part of the "Cola" package [42], dedicated to the calculation of the integrated luminosity is called Lumi++. This program also uses information from the data stream to calculate the dead time. Namely, during the analog-to-digital conversion and the data read-out electronics can not accept new events. This time is called the dead time. The time during which the system can accept events is called live time in SOS and real time in spectrometer A. These times have to be used for calculation of the N_e factor. Taking into account the recorded beam current, the calculated dead time, the target material and the target density the Lumi++ calculates the integrated luminosity for each run.

6.1.7 Phase space

The reaction phase space is defined by the geometrical acceptance of the spectrometers and by various experimental conditions at which the selected reaction was measured. It cannot be calculated analytically, but it can be determined via Monte Carlo simulation with the computer program Simul++ [42]. This program can simulate the accepted phase space or can generate events according to a given model or cross section data. In a simulation of the phase space the reaction products are generated isotropically in the solid angle for a specified range of four-momentum transfer and centre-of-mass angle for a given kinematics (type of reaction, beam energy, spectrometer angles, central momenta of the spectrometers, collimators). The above specified ranges are larger than the nominal spectrometer acceptances, to ensure a good behaviour of the simulated data at edges. In the simulation of a two arm experiment, each particle of the pair has to pass through the corresponding collimator and the particle momentum has to be inside the range accepted by the corresponding spectrometer. If these conditions are fulfilled, the event is recorded and the missing mass can be calculated too.

To ensure the consistency of the simulated and the experimental data the histogram binning and the parameters of the different cuts used in the simulation have to match exactly the ones used in the analysis of the experimental data.

6.1.8 Correction factors and parameters

The correction factors and parameters are describing various experimental conditions. Some of those conditions are chaining during the beam time, some of them are kinematic dependent and some remain constant during the time.

6.1.8.1 Liquid target density

The value of the liquid target density depends on the pressure and the temperature inside the inner target loop. The changing of the density during the beam time was investigated in 2004. It was observed that the density can not be considered as constant, and that the changes of the density when turning the beam on and off, or increasing and decreasing the beam current were significant [12]. It is also important to note that for every experiment the target cell is in a different condition, which can change during the cooling and especially when changing the beam current.

The dedicated computer program called Mezzo is used to create log files which contain all detector and setup adjustments, as well as records of several sensors, among which are the temperature and the pressure sensors inside the inner loop of the target cell. The calculation of the target density is not performed automatically. It has to be done during the analysis using the data from the Mezzo log files.
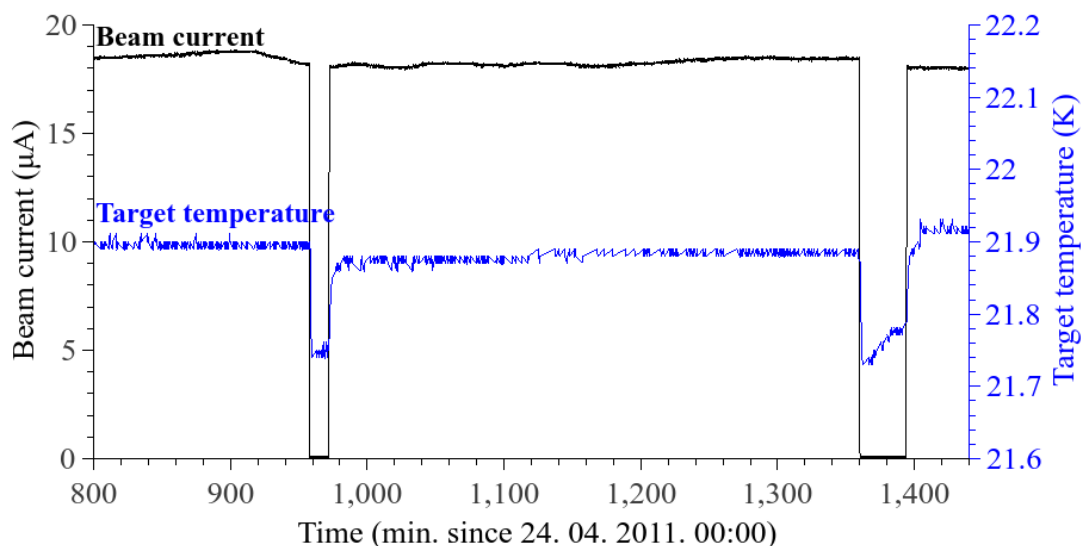
Figure 6.10 — Records of the beam current and the target temperature sensors for last 640 minutes of 24*th* of April 2011. The influence of the beam current on the target temperature can be observed.

The accuracy of the calculated target density depends on the accuracy of the measured pressure and temperature. The pressure sensor is calibrated and screened from

the radiation, and therefore it is reliable. The temperature is monitored by two sensors: the sensor A before and the sensor B after the target cell. For all conditions the sensor A shows a little bit smaller value of the temperature than the sensor B. When the beam is on, the target material is heated and as expected the sensor B measures a higher temperature. But the temperature difference is also present when the beam was off. This implies an existence of a little offset in one of the sensors. Since only the sensor A is calibrated, its measurements were used in the analysis.

A typical behaviour of the liquid target temperature, when turning the beam on and off, can be observed on Fig. 6.10. When the beam is turned on a part of the liquid target is heated, the temperature of the target rises very fast, and after some time saturates to a stable value. If the beam is switched off, the temperature inside the target cell drops rapidly to the old value.

In this analysis the target density is recalculated each time the temperature changes more than 0.03 K, the pressure more than 2 mbar, smaller fluctuations were averaged. This was done with the computer program "liquidDensity", which gives a density of the liquid hydrogen for a given temperature and pressure according to [43].

6.1.8.2 Snow on the target

Due to a non-perfect vacuum inside the scattering chamber, the snow of residual gases (nitrogen, oxygen, carbon dioxide, and water) will form on the cold surface of the target cell. The snow does not affect the incoming beam, because the beam produces enough heat to prevent formation of the snow at the beam entering spot. The same applies to the beam exit spot. But the rest of the target cell surface will be covered with the snow and reaction particles exiting the cell will suffer an additional energy loss, which has to be corrected in the analysis [44].

The snow thickness can change with the time and for each kinematics it has to be determined separately. It affects the position, the width and the shape of the experimental and the simulated missing mass peak. The thickness is determined by varying its value, until the shape and the position of the experimental and the simulated missing mass peak match as best as possible. The broadening of the experimental peak is mainly a result of the vertex position dependence. For the simulated peak the broadening is a result of the assumed energy loss and the assumed small angle scattering of the reaction products [12].

The Fig. 6.11 demonstrates the effect of the snow thickness on the missing mass distribution of the axialFF_897a setting. The left figure shows the background subtracted result of the analysis with the assumed 0.2 mm thick snow layer and the 1.5 mm thick
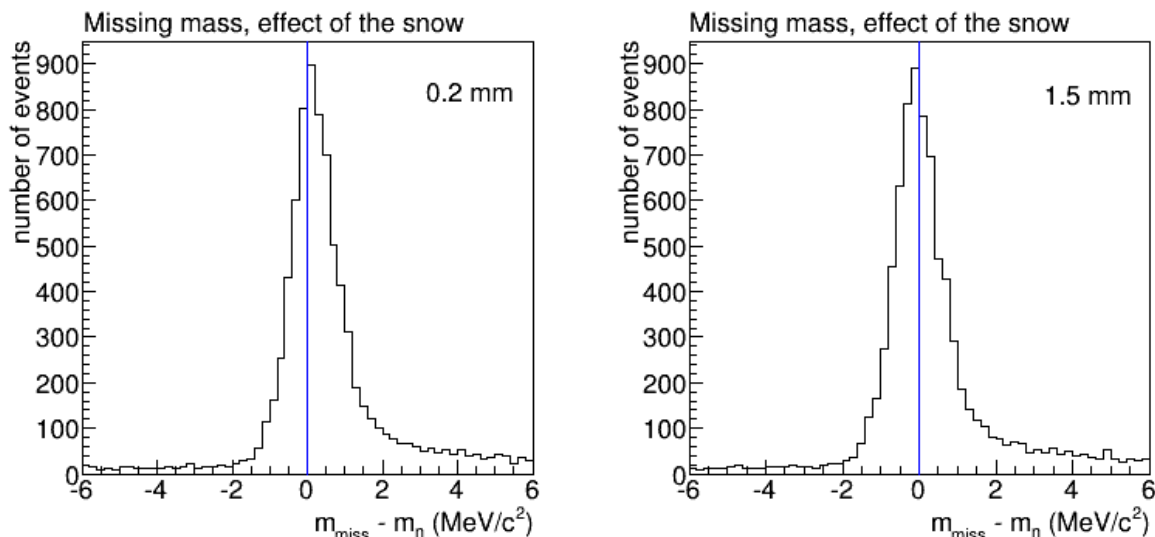
Figure 6.11 — The influence of the snow thickness correction on the missing mass distribution for the axialFF_897a setting. The left figure is an example of a good snow thickness estimate, and the right figure shows a shifting of the missing mass peak left from the 0 MeV/c^2 bin in case of an overestimation of the snow thickness.

layer on the right figure, where it is evident that the snow thickness was overestimated since the peak of the missing mass distribution is not centred at the bin 0, instead it is shifted towards the negative values of the missing mass.

6.1.8.3 Position of the target cell

Before each experiment the target cell is mounted in the centre of the scattering chamber at room temperature. During the cooling, due to the temperature stress, the cell can be displaced from the central position. The amount of the displacement can not be determined, because each spectrometer gives the target position which depends on the spectrometer angle. There is also a possibility that the target cell centre and the rotation centre of the spectrometers do not overlap. This can be corrected by the Z-offset of the target.

The Fig. 6.12. shows the reconstructed vertex along the beam line (Z-coordinate) for all particles in spectrometer A. The diameter of the target cell is 20 mm and ideally, the Z-coordinate of the reconstructed vertex should be between -10 and 10 mm to ensure occurrence of the reaction inside the target material. But due to the finite spectrometer spatial resolution, even events with the reconstructed Z-coordinate outside the target cell's physical limits may have been produced inside the target material (right zoomed Fig. 6.12). This has to be taken into account, when applying cuts on the reaction vertex.
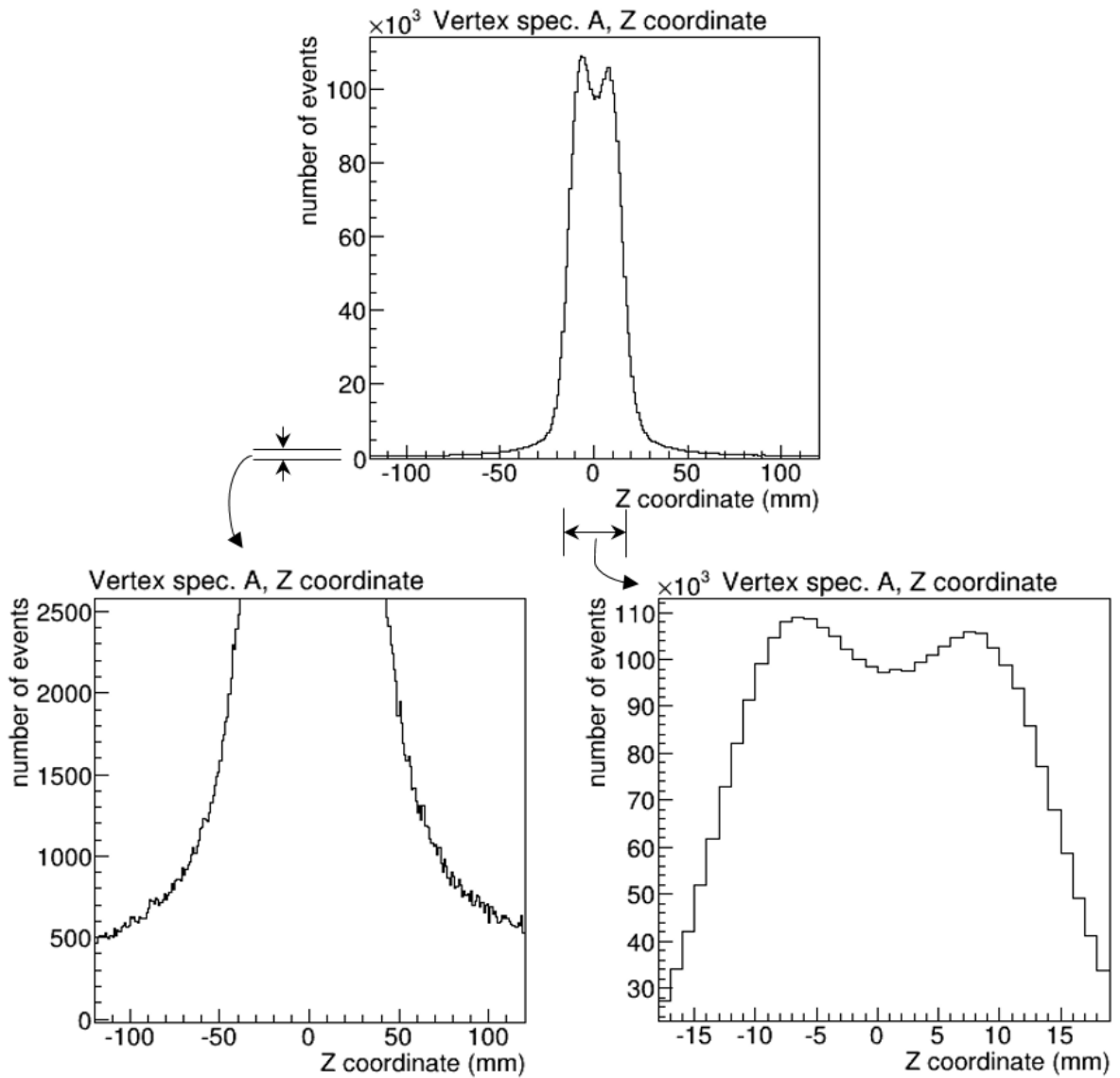
Figure 6.12 — The reconstructed Z-coordinate of the reaction vertex for all events in spectrometer A. Figures in the second row are zoomed parts of the above distribution.

6.1.8.4   Resolution of the spectrometers

The large change in the spectrometer central momentum causes the sufficient change in the resolution to alter the width of the experimental missing mass peak. This fact has to be taken into account in simulations by adjusting parameters representing the angular and the momentum resolutions of spectrometers. The measured SOS resolutions [16] were available and they were held fixed for each kinematical setting. The spectrometer A parameters were altered until the shape and the width of the simulated peak corresponded to those of the experimental missing mass peak. The used values do not necessarily correspond to the actual values of spectrometer A resolutions. The parameters are summarized in table 6.1.

Table 6.1 — Summarized resolution parameters used in the phase space simulation.

Setting	Spectrometer A, resolution		SOS, resolution	
	momentum (GeV/c)	angular (mrad)	momentum (GeV/c)	angular (mrad)
axialFF_306	0.0011	22.0		
axialFF_591	0.0015	8.5		
axialFF_897a			0.0013	11.0
axialFF_897L	0.00015	5.8		
axialFF_897R				

6.1.8.5 Total efficiency

The total efficiency correction factor is a product of several individual efficiencies. At the top level is a coincidence efficiency. It is a probability that two correlated events will be recognized as such and it quantifies the event-builder ability to synchronize and combine the data from two spectrometers into a single data stream. The coincidence efficiency for a two arm experiment can be determined by measuring the elastic electron scattering cross section as a single arm experiment $H(e,e')p$ and as a double arm coincidence experiment $H(e,e'p)$. For the same kinematical setting, the cross sections in both experiments should be equal and the coincidence efficiency is a ratio of those two cross sections. The value of $\epsilon_{coin} = 0.996$ was determined in [8].

At the spectrometer level we talk about the overall efficiency of a particular spectrometer, which is on the other hand a product of efficiencies of individual detectors.

For spectrometer A:

a) The efficiencies of scintillators planes in spectrometer A were systematically investigated in [8]. The three-detector method was used. In this method the efficiency of the middle detector is being determined and two outer detectors are used in coincidence, acting as reference or normalization detectors. In the case of the dE plane efficiency determination, the VDCs and the ToF plane acted as the reference detectors, and in the case of the ToF plane efficiency, the dE plane and the Čerenkov detector were the reference detectors. The results for spectrometer A are summarized in table 6.2. The small scintillator efficiency deterioration is caused by small voids at junctions of the scintillator paddles [8, 12]. The 100% efficiency could be achieved by using a scintillator plane with overlapping paddles, but then the particle identification by the energy loss method would not be reliable enough. For this experiment the most important was the efficiency of the ToF plane. It was rechecked and was determined to be $98.04 \pm 0.03\%$.

Table 6.2 — Efficiencies of the scintillator planes in spectrometer A [8].

dE plane (%)	ToF plane (%)	Total (%)
99.75 ± 0.01	99.78 ± 0.06	99.53 ± 0.07

b) For the Čerenkov detector we have to differentiate between two types of efficiencies. When the electron (or positron) identification is required, the efficiency is simply the ratio of the number of detected electrons N_{det} and the number of electrons with momenta high enough to produce a Čerenkov light N_{total}. In the case the Čerenkov detector is used as a veto detector, the efficiency is $1 - N_{det}/N_{nosig}$, where N_{nosig} is the number of particles which could not produce the Čerenkov light, and N_{det} is the number of particles which were detected. The Čerenkov detector efficiencies were studied in [45] using the three-detector method. The results are presented in table 6.3.

Table 6.3 — Efficiencies of the Čerenkov detector in spectrometer A [45].

Particles	Electrons (%)	Pions (veto mode) (%)
	99.98	100

For the analysis of this experiment, the Čerenkov detector was not used for the electron identification, because the acceptance of the Čerenkov detector is not known precisely enough. Therefore, the efficiency of the Čerenkov detector was not important in this particular case.

c) Performance of the VDC package is defined by two types of efficiencies: the single wire efficiency and the overall efficiency. The VDC package accept particles inside a certain angle interval and depending on the angle a particle will fly beside a corresponding number of signal wires. This number is not equal for each particle and the three-detector method can not be used to determine the efficiency. Instead, the data from the VDC is used by considering each signal wire as an independent detector. For a particle, which has triggered a certain number of signals in a VDC layer, the two outer wires with largest drift times are used as reference wires. All wires in between are marked as "tagged", corresponding bins in a "tagged wires" histogram are filled and the tagged wires are checked if they have produced a signal. If an answer is positive, a corresponding bin in a "number of wire" histogram is filled. After accumulating enough events, the "number of wire" histogram is divided by the "tagged wires" histogram and the single wire efficiency histogram is obtained. A typical single wire efficiency histogram of the x1 VDC layer is shown on Fig. 6.13. The averaged single wire efficiency was around 99.26%.
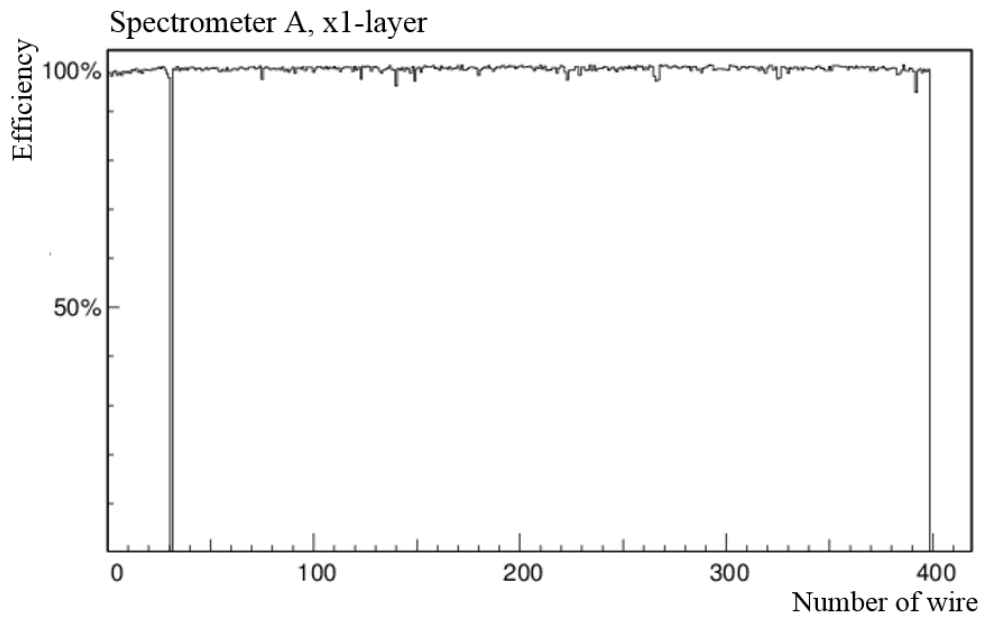
Figure 6.13 — Single wire efficiency of the x1 VDC layer in spectrometer A. The hole around bin 31 corresponds to wire without any signals.

The overall efficiency of the VDC package is defined as a ratio of the number of particles for which a trajectory was successfully reconstructed and the total number of particles passing through the drift chamber package. The VDC layers (x- and s-layers) do not work as independent detectors. For example, the trajectory in x-coordinate is successfully reconstructed if at least three wires in x-layers (x1 and/or x2) have produced signals. The same holds also for s-layers. Therefore, the overall efficiency will always be higher than the single wire efficiency. Even in case of a non-working or an inefficient wire, it is likely that the neighbouring wire will provide the needed information. Because of the high single wire efficiency, during the entire beam time, the overall efficiency of the VDC package was considered to be 100%.

For SOS:

a) Contrary to the scintillator layers in spectrometer A, the scintillators in SOS are not segmented and therefore there is no loss of efficiency in the junction of paddles as in the case of spectrometer A. The efficiency of scintillators was investigated in the framework of [12]. During this experiment, the efficiency of the scintillators was not rechecked again, but it was possible to verify the efficiency of the scintillator 2 in the data analysis. Two cross section determinations were performed: using the data from the scintillator 2 and without these data. The difference between these two cross sections should reflect the efficiency of the scintillator 2. Since the difference was only 0.1% and the statistical errors were

about 10 times larger, the efficiency of the scintillator 2 was approximated to be 100%. This procedure could not be applied to scintillator 1 because it is used in the trigger. However, since scintillators 1 and 2 are of identical material and geometry, the same efficiency was also assumed for scintillator 1.

b) Because of the specific signal wire grouping in SOS's drift cells, it is not possible to use the same method to determine a single wire efficiency, as used for the spectrometer A VDCs. The following approach has been used: first, all wires which have produced a signal are marked and corresponding bins of the "Number of wire" histogram are incremented by one. In order to enable some sort of a normalization, the response of the signal wires is linked in wire pairs. In each eight-wire-cell, signal wires are numbered from 0 to 7. If a wire w produces a signal, its neighbouring wire will be marked as "tagged": for even w a neighbouring wire is $w + 1$, for odd w a neighbouring wire is $w - 1$. Corresponding bin of the "tagged wires" histogram receives an entry. If the tagged wire itself has produced a signal a bin in the "eff.tmp" histogram gets an entry too. The single wire efficiency histogram is obtained by dividing the "eff.tmp" histogram with the "tagged wires" histogram [16].
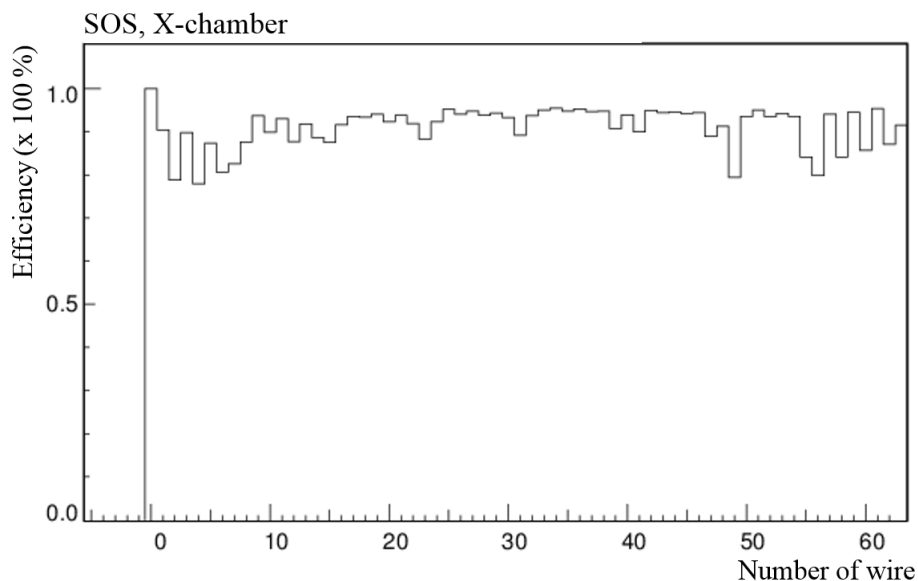
Figure 6.14 — Single wire efficiency of the SOS X-chamber. The two edge wires of the eight-wire-cell are less efficient than the middle six wires due to efficiency determination procedure.

This procedure suffers from the fact, that it is possible to have a particle which crosses two eight-wire-cells, but triggers only one signal in one of the cells. Usually this holds for a top or bottom wire. Therefore, the single wire efficiency of edge wires will be artificially reduced [16]. This effect is more pronounced in the X-chamber (Fig. 6.14) than in the Y-chamber (Fig. 6.15). The averaged single wire efficiency for the X-chamber was 89.89% and 97.26% for the Y-chamber.
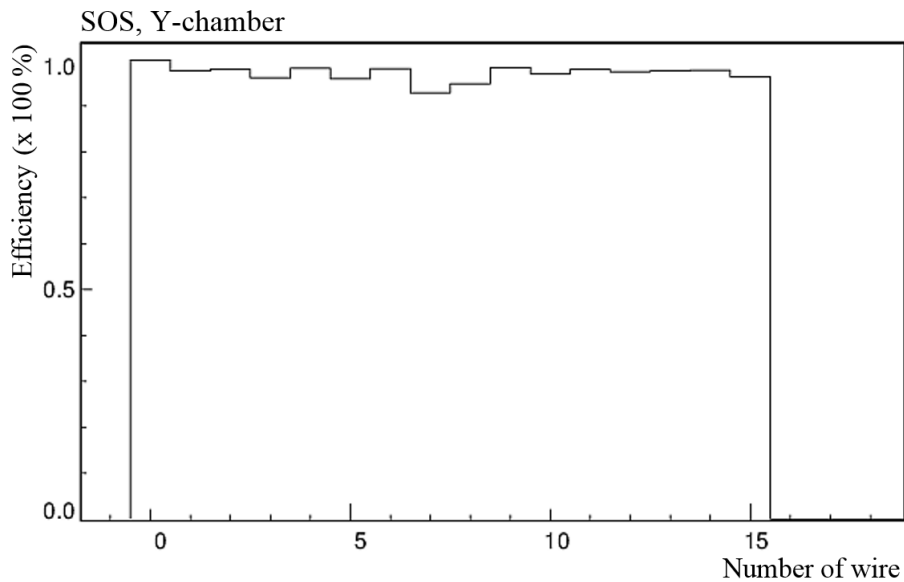
Figure 6.15 — Single wire efficiency of the SOS Y-chamber.

Even due to the high values of averaged single wire efficiencies of both chambers the overall efficiency of the SOS drift chamber package can not be considered to be 100%, as it was in the case of the spectrometer A VDCs. One reason is that the trajectory reconstruction algorithm accepts only events which have triggered at least four and maximum ten signal wires. The lower limit insures a reliable left-right decision and the upper limit rejects double events. The other reason is, that the same area is monitored by two drift cells in the Y-chamber and by eight drift cells in the X-chamber. Every drift chamber has a certain dead time, and the eight cells of the X-chamber can handle higher particle rates than the two drift cells of the Y-chamber. Therefore, the Y-chamber will be less efficient than the X-chamber.

To enable the calculation of the SOS chamber efficiency, the "pdcD.cc" file containing the trajectory reconstruction algorithm was modified. A possibility to distinguish if a trajectory reconstruction in a particular drift chamber was successful or not was added to it. If the trajectory reconstruction was successful for an event in the X-chamber, the bin "42" in the "x-pattern" histogram was incremented by one. For the successful trajectory reconstruction in the Y-chamber the same bin "42" was incremented by one in the "y-pattern" histogram. If for the same event the reconstruction was successful in both chambers, an entry was added to the bin "1" in the "pcdOK" histogram. The efficiencies of individual drift chambers can now be easily calculated. When calculating efficiency of the X-chamber, the Y-chamber is used as a reference detector and vice versa. The overall efficiency is product of the X- and Y-chamber individual efficiencies.

For each kinematical setting the SOS was placed at a different angle, the beam

current was also changed several times during the same setting and therefore the chambers were exposed to different particle rates. Because of that, the averaged individual and overall efficiencies were calculated for each setting and the results are summarized in table 6.4.

Table 6.4 — Summarized individual and overall efficiencies for each kinematical setting.

Setting	X-chamber eff. (%)	Y-chamber eff. (%)	overall eff. (%)
axialFF_306	89.50	90.63	81.11
axialFF_591	92.40	89.99	83.15
axialFF_897a	95.89	89.46	85.78
axialFF_897L	93.96	86.13	80.92
axialFF_897R	95.18	88.82	84.53

6.1.8.6   Pion decay correction

The positive charged pions π^+ are unstable particles with a lifetime of $\tau_\pi = 26.033 ns$. On their flight path through the spectrometer they can decay to a muon μ^+ and a muon neutrino ν_μ. The probability for this decay channel is 99.9877%. The pion decay can be described by [10]:

$$\frac{N_\pi^{det}}{N_\pi^{tg}} = e^{-s/l_\pi} = \frac{1}{K_{decay}}$$

(6.9)

where N_π^{det} is the number of detected pions, N_π^{tg} is the number of created pions at the target, K_{decay} is the pion decay correction factor, s is the length of the pion flight path and l_π is the pion decay length, which can be calculated in the following way:

$$l_\pi = \tau_\pi \beta_\pi c \left(\frac{E_\pi}{m_\pi c^2} \right) = \tau_\pi c \left(\frac{p_\pi}{m_\pi c} \right)$$

(6.10)

After applying all necessary cuts, the decay correction factor K_{decay} is calculated for each valid event. The determination of the pion decay length l_π is straightforward by using 6.10, since the particle momentum p_π is measured by the spectrometer.

Calculation of the pion flight path length s is little more complicated and it is realized in several steps. The assumption was made, that outside of the SOS dipole magnet a particle travels on a straight line and inside the dipole magnet it travels on a circular orbit of the radius R. The distance from the target centre and the SOS was measured before the beginning of the experiment. The dimensions of the SOSs magnet yoke interior and the detector package interior are very well documented.

The distance from the particle vertex to the edge of the magnet entrance and coordinates of entering point into the magnet field are calculated first. The starting point

and the direction of the particle are defined by the reconstructed target coordinates $(\delta p_0, \theta_0, y_0, \phi_0)$. This is followed by a calculation of the distance from the particle exit point out of the magnetic field to the top plane of the scintillator telescope. The co-ordinates of the particle exit point are calculated too. The information is provided by the SOSs drift chamber coordinates $(x_{ch}, \theta_{ch}, y_{ch}, \phi_{ch})$. The values of x_{ch} and y_{ch} corre-spond to projections of the particle trajectory on the top plane of the magnet yoke. The final step is a calculation of the circular orbit length for the particle inside the magnetic field. The coordinates of the entrance and the exit points are provided from the previ-ous steps. The radius of the circular orbit is determined by the measured momentum and by the value of the magnetic field. The sum of those three lengths is the pion flight path length s. All formulas used in the above described steps are given in Appendix B.

A typical histogram of the particle lengths s is shown on Fig. 6.16 (axialFF_591 setting, all necessary cuts applied). The length of the particle trajectories inside the SOS ranges from 1704 to 1991 mm.
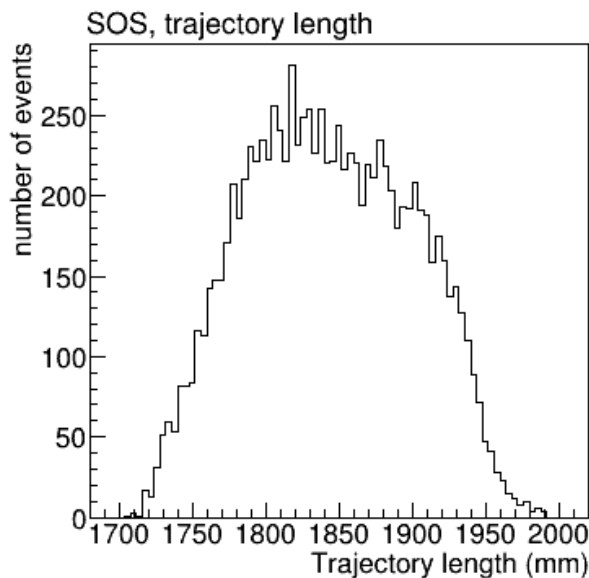
Figure 6.16 — Distribution of the particle trajectory lengths in SOS. Data from axialFF_591 setting, all cuts applied.

When applying the decay correction to the valid events, one has to keep in mind the following fact. Even with best cuts it is not possible to totally reduce the random coincidence background to zero and every averaged K_{decay} will be contaminated with random coincidences data. The cuts are keeping this contamination small, and at the same time they insure that even random coincidence particles behave "well" (they have vertex inside the target, their momenta are inside the acceptance of the spectrometer etc.).

In past experiments involving the $p(e, e'\pi^+)n$ reaction, the total number of valid

coincidences was corrected with a single averaged K_{decay}. As can be seen on Fig. 6.17, the K_{decay} (axialFF_591 setting) ranges from 1.279 to 1.387 with a certain distribution. Therefore, different approaches of averaging were tested. In first approach the full momentum acceptance of SOS (from -13% to 16%) was divided into 1 MeV/c wide intervals, 29 in total. For each interval three histograms were created. Coincidence missing mass histogram and K_{decay} histogram were produced with cut on coincidence peak, plus all other cuts. The background missing mass histogram contains data of the timing background cut, plus all other cuts. The averaged K_{decay} is calculated from the data contained in a corresponding interval. The background missing mass histogram is subtracted from the coincidence histogram and remaining number of coincidence evens are corrected with averaged K_{decay}. In the end, contributions from every interval have to be summed. Another averaging approach was to divide the particle length s histogram into 10 mm wide intervals and to follow the same procedure as described above.
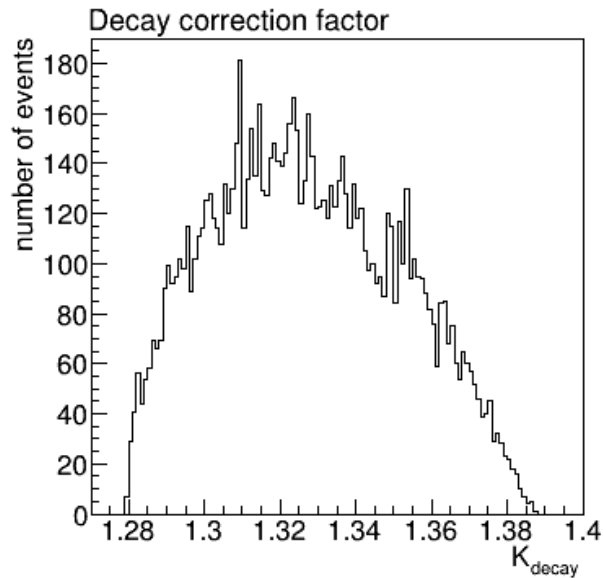
Figure 6.17 — Distribution of the decay correction factors. Data from axialFF_591 setting, all cuts applied.

6.1.8.7 Muon contamination

The pion decay correction is valid if no muon contamination is present in the data. Some muons can have momenta very close to that of a decayed pion. Those muons cannot be distinguished from pions, by means of applying different cuts. In a procedure of the decay correction, the muon contamination is also multiplied with a calculated correction factor. To prevent an overcorrection, the muon contamination has to be determined by a Monte Carlo simulation.
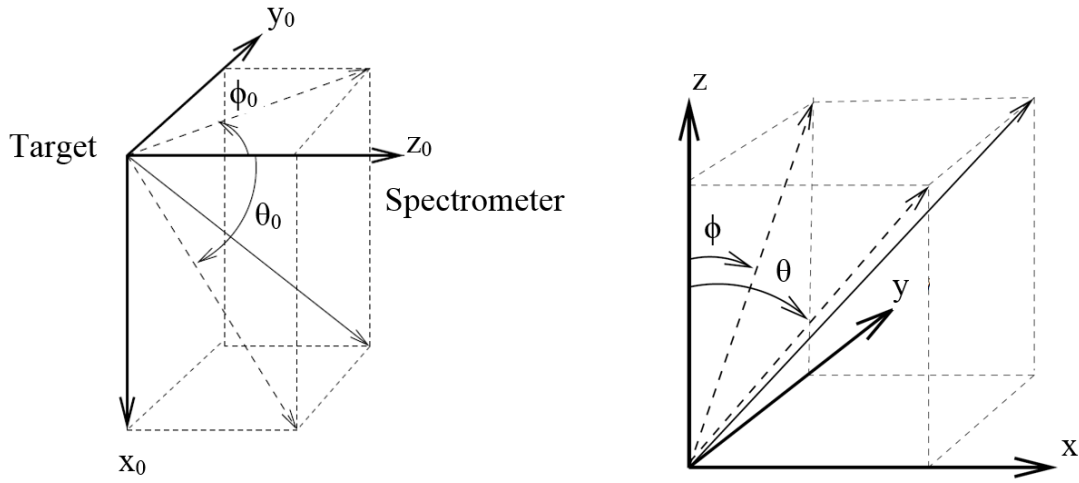
Figure 6.18 — Definition of target coordinate system (left) and the chamber coordinate system (right), from [35].

For his diploma thesis [46], Miha Mihovilovič has developed a software for a simulation of the particle decay inside spectrometers A and B as the standalone program SimDeacy and as a part of the standard A1 simulation program Simul++ [42]. Both programs track the particles from the target through the spectrometers to the focal plane and have an ability to distinguish between pions and in decay produced muons (neutrinos are neglected).

In framework of this thesis the functionality of the simulation software (both SimDecay and Simul++) was extended to include also the SOS. Only drawback of the new software is that the simulated magnet field does not include the fringe fields. The SOS has a circular dipole magnet with the 350 mm radius. Between the circular pole shoes the magnetic field is uniform and has only one component. In the target coordinate system, see Fig. 6.18, this means that only the component B_y is non-zero. But, at the edges of pole shoes components B_x and B_z are not zero any more. These so-called fringe fields have a focusing effect on particles with positive values of the θ_0 angle and a defocusing effect on particles with the negative θ_0 in the y-direction. Because of that, the SOS collimator has a shape of a trapezoid. The fringe fields were not included in the simulation and a little discrepancy between the experimental and simulated data can be expected.

Using the updated simulation software, a Monte Carlo simulation for the pion decay in SOS was performed for each kinematical setting. The particles were traced through the SOS, from the target to the read-out plane just above the third scintillator. The output of the read-out plane simulates the output of the drift chambers. It gives four coordinates $(x'_{ch}, \theta'_{ch}, y'_{ch}, \phi'_{ch})$. When projected to the plane at the top plane of the magnet yoke, they correspond to the chamber coordinates $(x_{ch}, \theta_{ch}, y_{ch}, \phi_{ch})$, using the transfer matrix the target coordinates and subsequent the missing mass can be

reconstructed. The obtained missing mass histogram of the axialFF_591 setting for the pion decay simulation is shown on the Fig. 6.19. The red distribution represents the pions and the blue distribution, under the red one, represents the muons. It can be clearly seen that there is a certain amount of muons whose reconstructed missing mass distribution is partially overlapping the pion distribution. Exactly these muons can not be excluded from the true events. Furthermore, the amount of the muon contamination also depends on the cut on the radiative tail of the missing mass distribution and the muon correction factor has to be calculated for each missing mass cut separately.
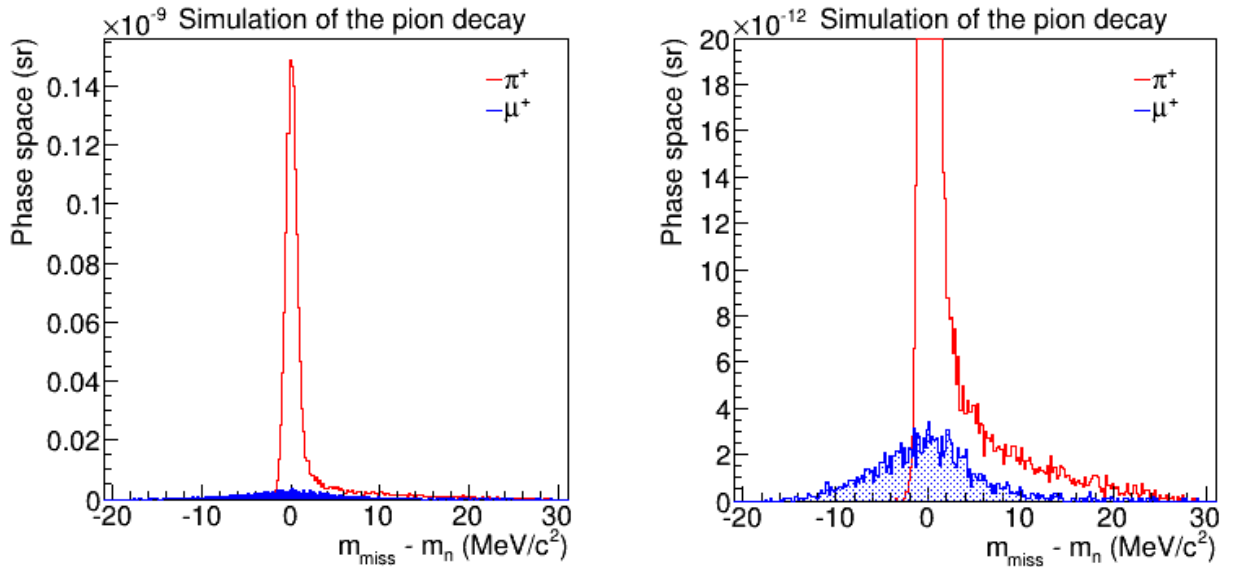
Figure 6.19 — Monte Carlo simulation of the pion decay for the axialFF_591 kinematical setting. Together with true events (red histogram), the missing mass spectrum contains also contamination (blue histogram) produced by the misidentified muons. The left figure shows full range of the distribution and the right figure shows the zoomed part of the missing mass distribution.

The amounts of the muon contamination and the corresponding correction factors for the missing mass interval from -3 to 11 MeV/c^2 are shown in table 6.5. From the averaging of the pion decay correction factors on Fig. 6.17, a value of 1.333 is obtained. This means that about 25% of the total number of the pions produced at the target will be decayed into the muons and the neutrinos. According to results in table 6.5, approximately 30% of those muons will be misidentified as the pions. All other muons (approximately 70% of them) will either not be inside the missing mass interval, or their trajectories will miss the second and the third scintillator and will not be detected.

In order to check the reliability of those results, the code with decay has been compared to the code without decay by using the phase space simulation of the same kinematical setting. The first simulation was performed with the decay turned off: this means that the code checks only if the particle has passed through the collimator and

Table 6.5 — Muon contamination percentage obtained with the Monte Carlo simulation of the pion decay for each kinematical setting and the corresponding correction factor for the missing mass cut from -3 to 11 MeV/c^2.

Setting	Muon contamination (%)	Correction factor
axialFF_306	7.674	0.92326
axialFF_591	7.276	0.92724
axialFF_897a	7.783	0.92217
axialFF_897L	7.663	0.92337
axialFF_897R	7.372	0.92628

has an appropriate momentum. The second phase space simulation was done with the decay turned on, but the pion lifetime was intentionally changed to a high value ($\gg \tau_\pi$) to prevent the decay of the pion inside of SOS. In an ideal case the results should be equal or at least differ very little. For all settings the first simulation has always given about 3.6% higher values of the phase space. There can be several reasons for this discrepancy. One of them is the fact that compared to the first simulation, the second one tracks the particles even after the collimator, throughout the magnet to the detector package. On this path all little imperfections sum up and produce the final discrepancy. The value of the discrepancy is acceptably small and the decay simulation is reliable enough to be used for the determination of the muon contamination.

6.1.9 Cuts

One of the biggest parts of the analysis consists of finding out on what quantities cuts can be imposed and where exactly to place them. General purpose of the cuts is to accept the true events and to reduce all kinds of background events. Some cuts cannot be used in the simulation: either the variable is not simulated (detector signals) or the variable is not described reliably by the simulation. These cuts have to be without the loss of true events. Hence, a missing mass histogram is produced out of excluded data. If a peak appears in this missing mass histogram around the bin 0, this means that the cut was too "aggressive". The value of the cut has to be changed until the peak in the missing mass histogram of the excluded data disappears. Small loss of true events is only acceptable for cuts on spectrometer acceptances, since the same cuts are also used in simulations. Finally, a missing mass histogram is produced out of data surviving all determined cuts. The cut on this histogram defines the quantities used in calculation of the cross section.

The following cuts were used in the analysis (some of them have been already introduced):

a) Cut on the coincidence time peak, Fig. 6.5. For this cut it is most important to be

as narrow as possible. Since it removes the biggest amount of the background. The cut accepts only events inside an interval from -2.0 to 2.5 ns around the coincidence time peak, which is centred around the zero channel and it is not perfectly symmetric. This cut is the same for all kinematical settings.
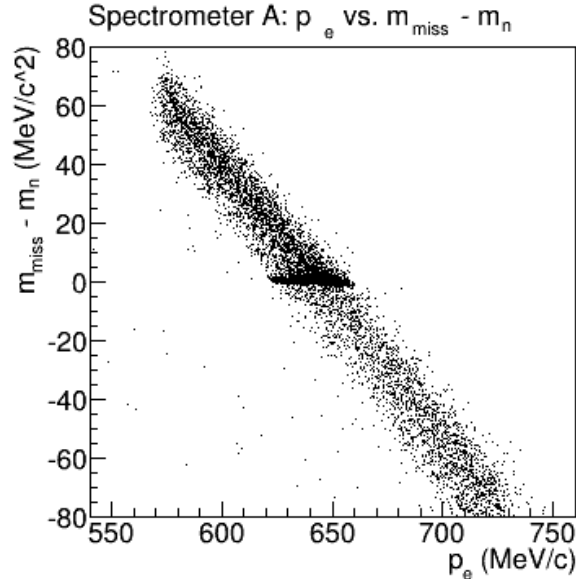
Figure 6.20 — Electron momenta in spectrometer A vs. missing mass spectrum, setting axiall_855a, only the cut on the coincidence time peak was applied.

b) Cut on the random background in the coincidence time histogram, Fig. 6.5. The events inside the intervals from -50.0 to -10.0 ns and from 7.0 to 18.0 ns are used to remove the random coincidence background, which is present under the coincidence time peak. The procedure of the random background subtraction was in detail explained and demonstrated in section 6.1.3.

c) Cut on the momentum of spectrometer A. Fig. 6.20 shows a 2D histogram of electron momenta in spectrometer A vs. missing mass spectrum of the axiall_855a kinematics with the coincidence timing cut. It can be observed that the electron momenta corresponding to the missing mass peak are concentrated inside a certain interval, and they are not distributed inside a full range of the spectrometer momentum acceptance. This small momenta interval was separated for each setting and appropriate cuts were imposed on the momentum of spectrometer A.

d) Cut on the Z-coordinate of the reconstructed vertex in spectrometer A. Some of the electrons can be scattered in the different foils and in the air between the scattering chamber and the spectrometer entrance. The trajectory of such electron can be changed and the reconstructed vertex can be outside the cryo target, see Fig. 6.12. The background caused by such electrons can be reduced by cutting on the Z-coordinate of the vertex. Accepted events have to be inside of the interval
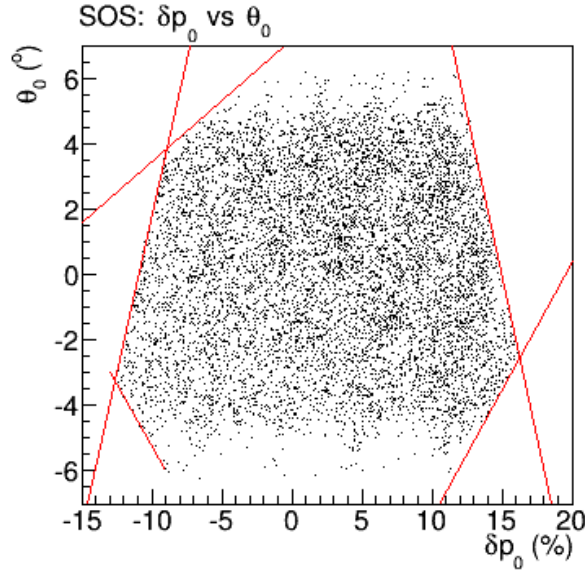
Figure 6.21 — SOS target coordinates δp_0 vs. θ_0. Cuts on SOS acceptance are represented by red lines.

-50 mm $< Z_v < 50$ mm. This interval is wider than the target cell diameter. Since the spatial resolution of the spectrometer is finite, the vertex of a reaction occurring near the target walls could be reconstructed outside of the target. Cutting on the physical dimension of the target would exclude these events.

e) Cut on the acceptance of SOS. This is the most complicated cut. The 2D histogram of the SOS target coordinates δp_0 vs. θ_0 was obtained only with cuts a), c) and d), see Fig. 6.21. A trapezoid shape, with truncated edges, can be observed. The simulation of the pion decay indicated that the detector package should cause this effect. Because of the complicated shape of the SOS acceptance, the imposed cuts were in a form of linear functions: $\theta_0 = a \cdot \delta p_0 + b$. The cuts are chosen to include as much of the acceptance as possible. This means, if a certain cut would be changed to decrease the acceptance, the final cross section will not be significantly changed, because the same amount of the true events and the corresponding phase space have been excluded. But, if a certain cut would increase the acceptance, no new true events are included, but the corresponding phase space is bigger and the final cross section would be significantly smaller. The cuts which satisfy this requests are shown on Fig. 6.21 as red lines.

f) Cut on SOS drift chamber coordinates. Matthias Ding reported in his thesis [16], that in case of particles passing very nearly the signal wires, the left-right decision can turn out wrong. Instead of the real trajectory, a mirrored ghost trajectory with the wrong angle sign is reconstructed. The same effect can also be observed in this experiment on the histogram x_{ch} vs. θ_{ch}, see Fig. 6.22. The correction
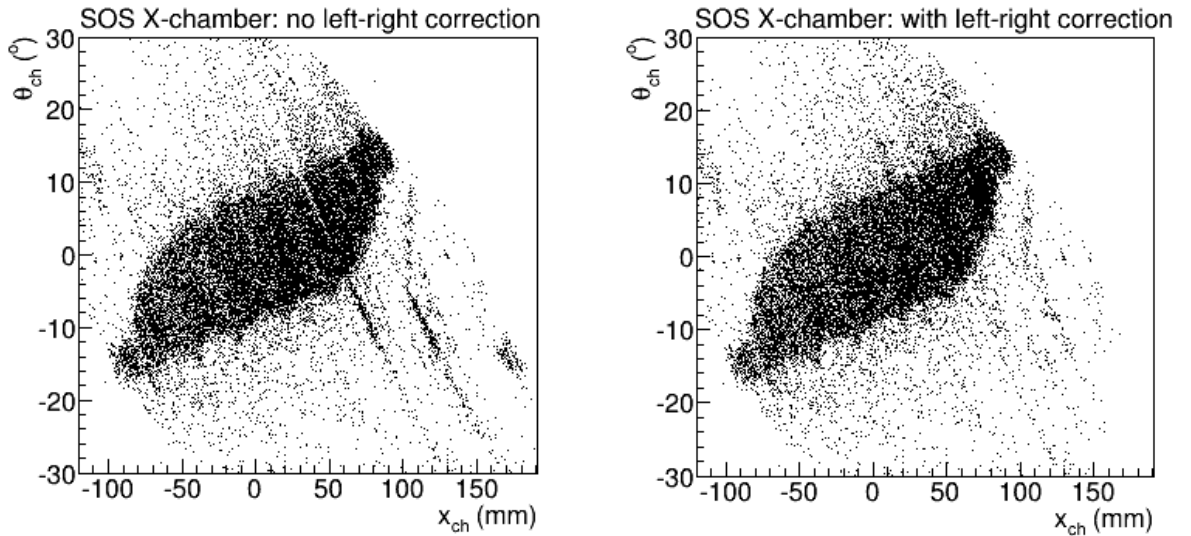
Figure 6.22 — 2D histogram x_{ch} vs. θ_{ch} of the SOS. The left figure shows the data without the left-right correction: the stripes of missing data on the right side of central distribution are due to the wrong left-right decision; the sign of the angle is reconstructed wrongly, and the corresponding stripes of data appear in the lower right corner of the histogram. The right figure shows the data including the left-right correction: compared to the left figure holes in the central distribution are now filled with the data.

was implemented in the trajectory reconstruction program "pdcD.cc". The lower right stripes were isolated and the decision regarding their angle sign was done intentionally. After the correction the isolated stripes filled the vacancies in the top right part of the left x_{ch} vs. θ_{ch} histogram, see Fig. 6.22. And, most important of all, the data in the selected stripes contained the true events.

On the left side of the distribution the effect of the wrong left-right decision can not be seen clearly, as it can be on the right side, Fig. 6.22. One explanation is that particles reaching the left side of the chamber do not have trajectories for which the angle sign is easily reconstructed wrongly. And the pessimistic explanation is, that the wrong reconstructed trajectories are hidden in a shaded area on the left side and thus can not be observed.

g) Cut on SOS scintillators. The scintillator telescope of the SOS was designed to be used as an $\Delta E - E$ telescope for the particle identification. The Fig. 6.23 shows a 2D histogram of energy deposition in scintillator layers dE2 vs. dE3. The bottom left corner of the left histogram contains the minimal ionizing particles. In both histograms, the left rising slope represents particles which have passed through the last scintillator layer and the right falling slope contains particles which were stopped in the last layer. The minimal ionizing particles were excluded with the cuts on ADC channels $dE1 > 260$ and $dE2 > 280$.
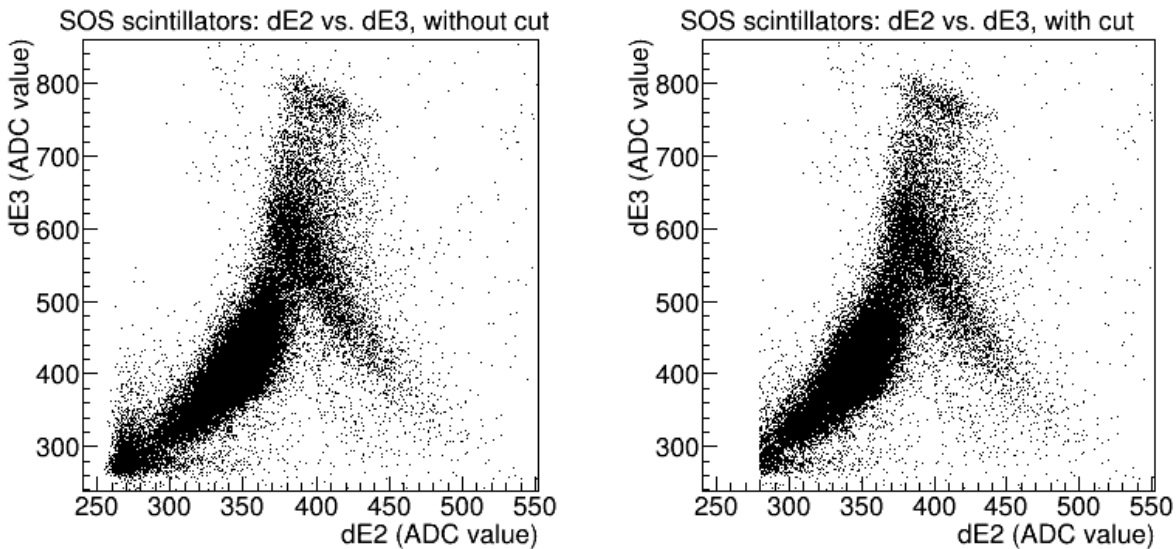
Figure 6.23 — 2D histogram of energy deposition in SOS scintillators dE2 vs. dE3. Left histogram includes minimal ionizing particles and the right histogram is with the cut which removes the minimal ionizing particles.

h) Cut on the missing mass peak. For the calculation of the cross section the integration of the events in the experimental and simulated missing mass peak has to be performed for the same interval. Therefore, the experimental and the simulated missing mass peaks have to overlap in the shape and the position as well as possible. First the experimental peak was centred around bin 0 by small changes of the specified central momentum of spectrometer A and by the snow thickness adjustment. The central momentum is defined by central magnetic fields. The magnetic field of each dipole magnet is monitored by four NMR probes and by one Hall probe. The NMR probes are located approximately 60 mm from the spectrometer magnetic midplane [10]. The magnetic field values measured by the NMR probes can differ from the values encountered by particles and this can result in a little shift of the missing mass peak with respect to the bin 0. In simulations, those two parameters were held fixed and only the resolutions (momentum and angular) of the spectrometers were varied until the best possible matching of those two peaks was obtained. In order to make the compassion of the histogram shapes possible, the phase space missing mass distribution has to be normalized with respect to the background subtracted missing mass distribution. The normalization factor was defined as a ratio of the highest bins in both distributions. In such approach the highest bins of both distributions will match perfectly [12].

The result of these procedures is shown on Fig. 6.24 for the axialFF_591 setting. Similarly as reported in [12], the matching of the two missing mass distributions is good but not perfect and the discrepancies can especially be seen in the radiation tail region of the distributions and near the beginning of the peak's left edge.
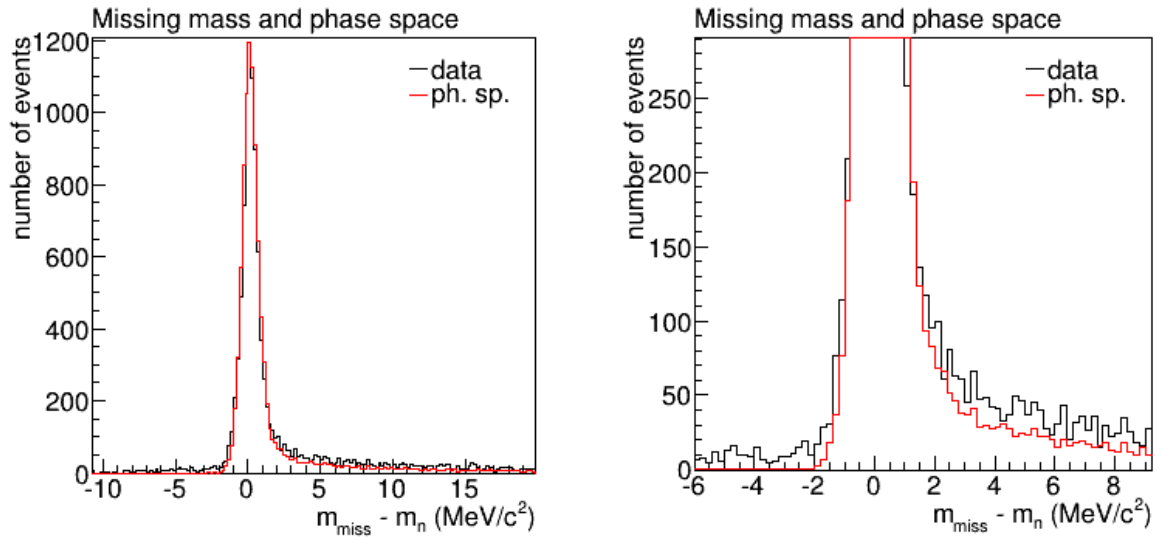
Figure 6.24 — The missing mass distributions of the background subtracted data (black) and corresponding phase space simulation (red) for the axialFF_591 setting. The phase space distribution was normalized with respect to the highest bin of the experimental distribution. The left figure shows the full height of the distribution and the right a zoomed detail.

These can be caused either by inaccurate simulation of the radiation tail or by some kind of background which was not removed by the subtraction and was not included in the simulation, candidates for this background are muons [12].
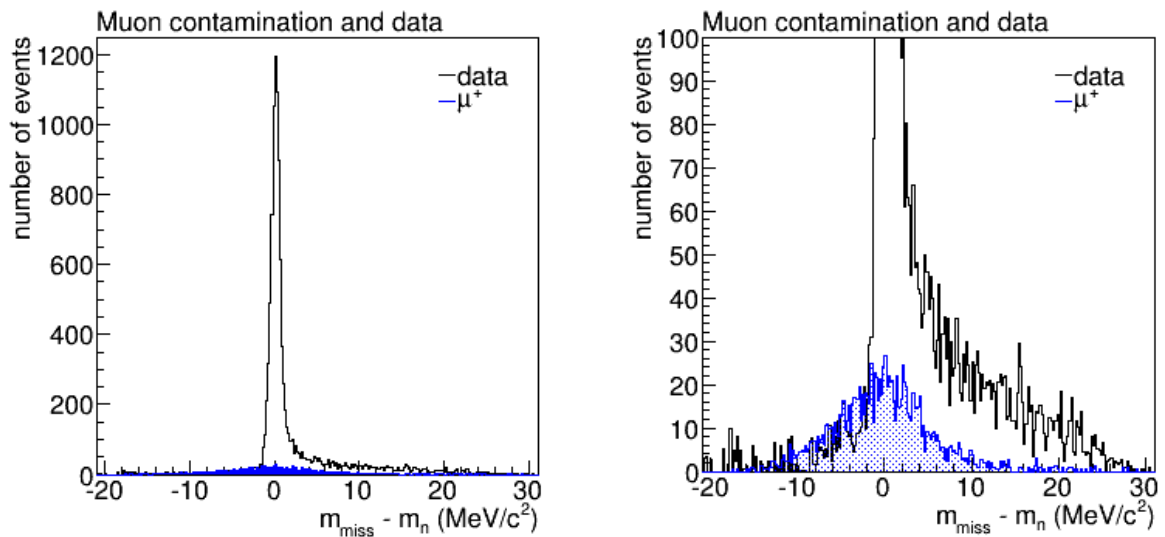
Figure 6.25 — The missing mass distributions of the background subtracted data (black) and of the muons form the pion decay simulation (blue) for the axialFF_591 setting. The total simulated distribution (pion + muon) was normalized with respect to the highest bin of the experimental distribution. The left and the right figure show same distributions, they only differ in ranges which are shown.

By using the Monte Carlo simulation of the pion decay introduced in section 6.1.8.7, it was possible to verify that the discrepancies are to some extent caused

by the muons. In similar normalization procedure as described above, the muon missing mass distribution was prepared for comparison with the background corrected data, see Fig. 6.25. Now we can see, that the muons cause the "foot" at the beginning of the left edge of the data peak and also contribute a little to the height of the radiation tail.

The muon missing mass distribution can also be subtracted from the experimental missing mass distribution. Together with the corresponding phase space distribution, the result is shown on Fig. 6.26. The "foot" in front of the left edge has now fully disappeared (this is even a little too much corrected, since negative values appear) and the discrepancy between the simulated and the experimental radiation tail is now smaller, compared with Fig. 6.24.
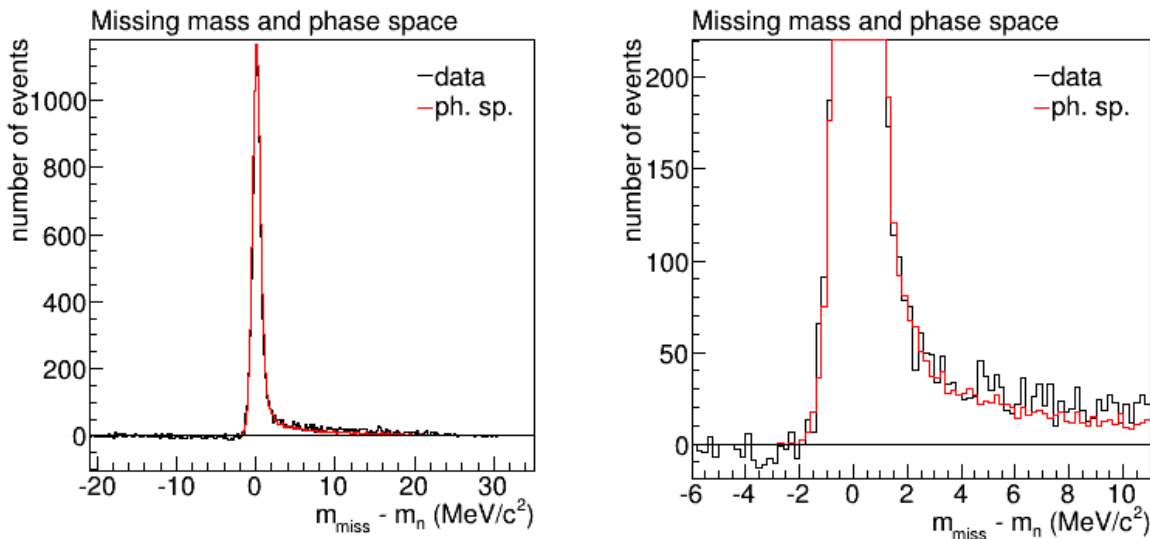
Figure 6.26 — The missing mass distributions of the background and the muon subtracted data (black) and corresponding phase space simulation (red) for the axialFF_591 setting. The left figure shows the full range of the distributions and the right figure a zoomed part.

The integration interval begins at $-3\,\mathrm{MeV}/c^2$, which was estimated to be a starting point of the left edge of the missing mass peak for all kinematical settings. Three interval end points were chosen: 11 MeV for the Rosenbluth separation, 6 and 16 MeV for estimations of systematic errors.

6.1.10 Experimental and simulated target coordinates

The effects of the cuts on the experimental data and the phase simulation were verified by comparison of target coordinate histograms. To make the experimental and the phase space histograms comparable, the phase space histogram bins were, for each

target coordinate, normalized with ratio of the highest bins in the experimental and the phase space histogram. When using this normalization method the height of the distributions will not match exactly. One reason are statistical fluctuations both in data and simulation. The other reason is the fact that the phase space simulation is not weighted with any model, which would affect the height of particular bins, especially the ones at the distribution edges.
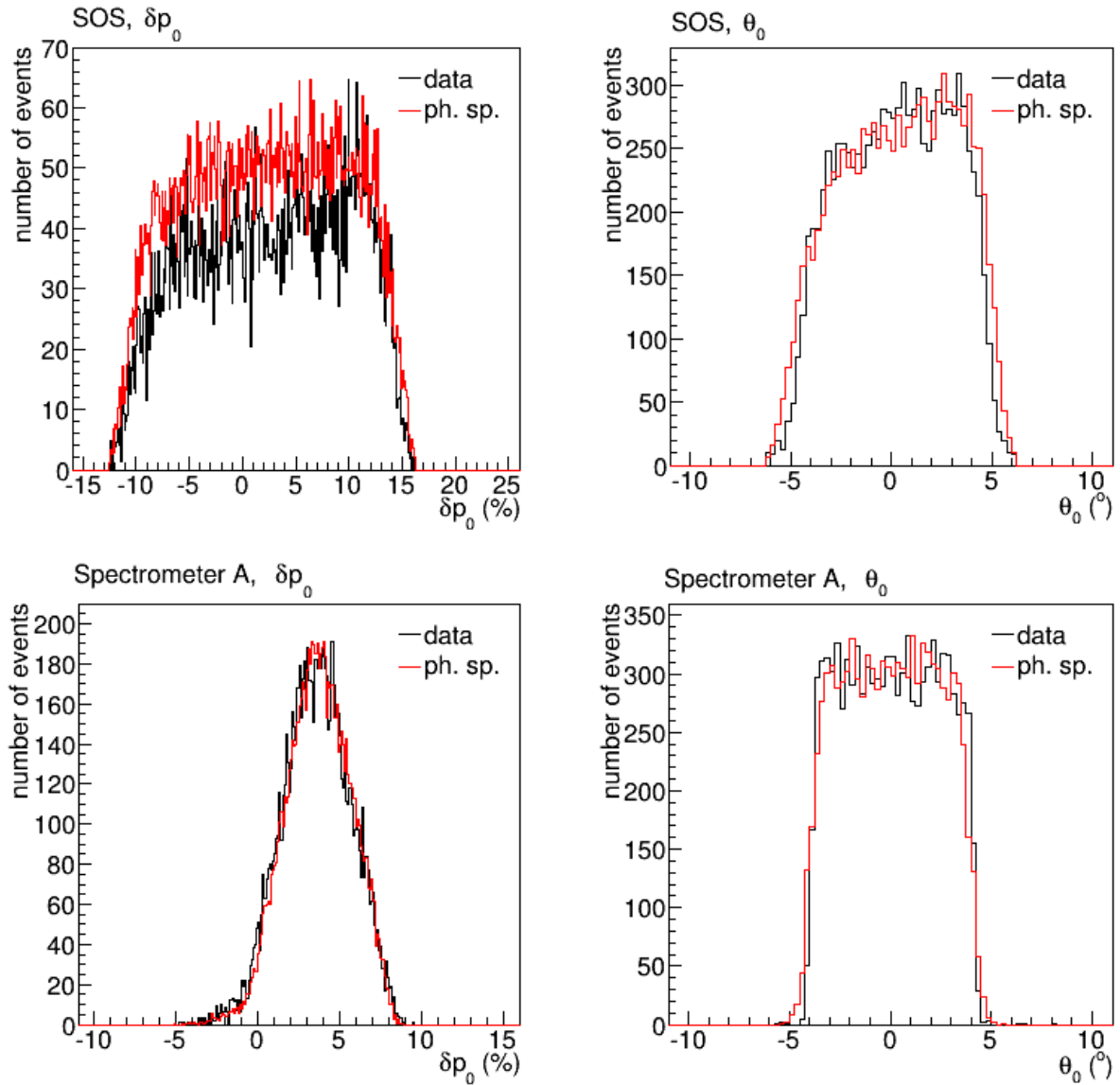
Figure 6.27 — Dispersive target coordinates $(\delta p_0, \theta_0)$ of the experimental (black) and corresponding phase space simulation (red) data for the axialFF_591 setting in SOS and spectrometer A.

For the dispersive coordinates $(\delta p_0, \theta_0)$ it is important that their distribution intervals match, since these coordinates are used in the calculation of the missing mass. Fig. 6.27 shows background corrected δp_0 and θ_0 experimental and phase space simulation histograms for the axialFF_591 setting in SOS and spectrometer A. As expected, the

distributions of δp_0 and θ_0 match in interval ranges for both spectrometers.
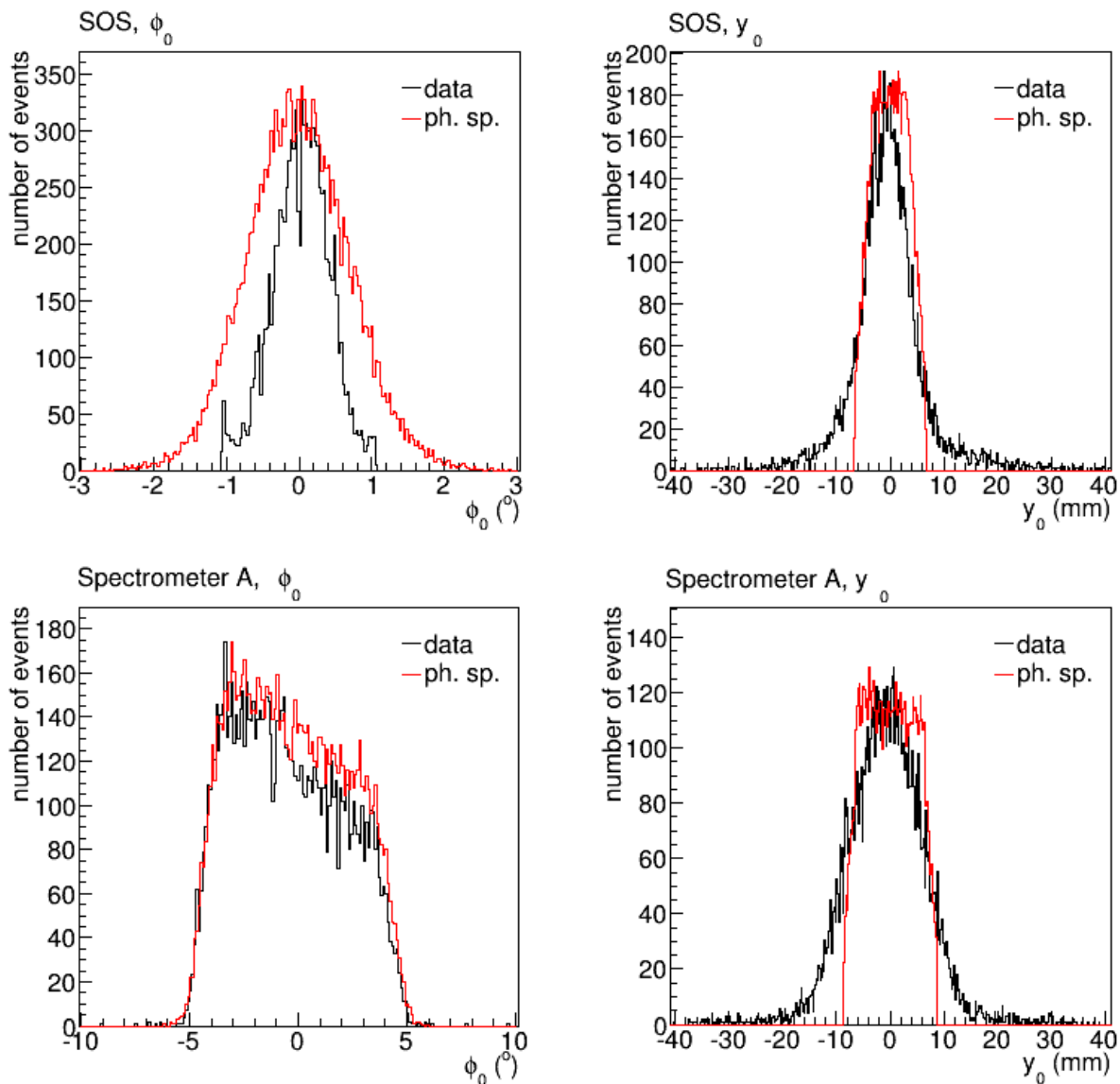
Figure 6.28 — Non-dispersive target coordinates (ϕ_0, y_0) of the experimental (black) and the corresponding phase space simulation (red) data for the axialFF_591 setting in SOS and spectrometer A.

Fig. 6.28 shows, for same kinematical setting, the comparison of the experimental and the simulated non-dispersive coordinates (ϕ_0, y_0) in SOS and spectrometer A. For both spectrometers the simulated and the experimental y_0 coordinate do not match in the distribution range, since the simulation software does not have an option for adjusting the resolution of this coordinate. In the case of SOS the ranges of the ϕ_0 coordinate distributions do not match, due to transfer matrix effects. The decision was made to perform the analysis with the SOS transfer matrix which reconstructs the momentum with the best possible resolution, as this also affects the resolution of the reconstructed missing mass. But this matrix is not optimal for the reconstruction

of the non-dispersive coordinates. Therefore no cuts are made on the non-dispersive coordinates of both spectrometers. The only thing in the analysis which is affected by the non-dispersive coordinates is the calculation of the particle trajectory length in SOS for the pion decay correction. In the non-dispersive direction the space for the passage of particles in SOS is very slim. Therefore, a possible error in the length calculation is very small and it is taken into account in a systematic error estimation for the pion decay correction factor.

6.1.11 Estimation of the total systematic error

The total systematic error has several contributions. The value of each contribution was determined separately and the method used for the value estimation will be described in the following text.

a) **Uncertainty of the luminosity ΔL.** The procedure for calculation of the luminosity is described in the section 6.1.6. When calculating the uncertainty of the luminosity ΔL, the beam current uncertainty ΔI, the target material density uncertainty $\Delta\rho$ and the average target length uncertainty $\Delta\bar{x}$ have to be taken into account. For the beam current uncertainty $\Delta I = 0.3/n$ μA formula can be used, where n is the number of recirculations in the third RTM of MAMI accelerator. The uncertainty of the target density $\Delta\rho$ comes mostly from the fluctuations of the target temperature. The fluctuations of the target pressure have only a minor influence on the uncertainty of the target density $\Delta\rho$. The lowest and the highest values of the temperature and the pressure fluctuations were used to estimate the uncertainty of the density $\Delta\rho$ by using the program "liquidDensity". The relative uncertainty of the average target length $\Delta\bar{x}^{rel}$ was taken to be 0.5% as in [10]. All other inputs for luminosity determination were considered to be precise enough to neglect their uncertainties.

$$\Delta L = \sqrt{\left(\frac{\partial L}{\partial I}\Delta I\right)^2 + \left(\frac{\partial L}{\partial \rho}\Delta\rho\right)^2 + \left(\frac{\partial L}{\partial \bar{x}}\Delta\bar{x}\right)^2} \qquad (6.11)$$

Using the equations defined in section 6.1.6 the uncertainty of the luminosity ΔL follows (the relative error was calculated to be between 0.58% and 0.59%):

$$\Delta L = \frac{T \cdot N_A \cdot Z}{e \cdot M}\sqrt{(\rho \cdot \bar{x} \cdot \Delta I)^2 + (I \cdot \bar{x} \cdot \Delta\rho)^2 + (I \cdot \rho \cdot \Delta\bar{x})^2} \qquad (6.12)$$

b) **Uncertainty of the pion decay correction ΔK_{decay}.** Here, the uncertainty comes from the pion momentum and the trajectory length reconstruction errors. The
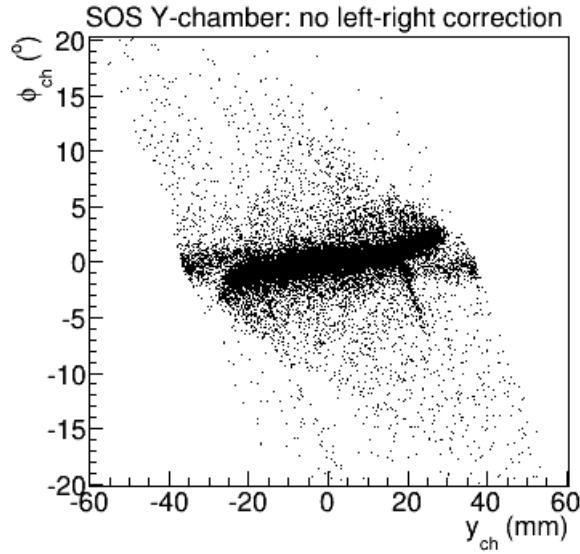
Figure 6.29 — 2D histogram y_{ch} vs. ϕ_{ch} of the SOS. Two stripes of data coming from the central distribution are due to the wrong left-right reconstruction.

momentum error Δp_π value was estimated in a measurement of the quasielastic reaction $^{12}C(e,e'p)^{11}B$ to be as high as 1.3 MeV/c [16]. The value of the length determination error Δs was not experimentally determined, a safe estimation of 2 cm was chosen instead. There are two reasons for such high value. The first reason is the fact that some dimensions of the detector package are known with limited precision. The second reason is the omitting of the left-right correction for the Y-chamber, because the data with the wrong angle sign are not clearly separated from the rest, as it can be seen on Fig. 6.29. The uncertainty of the decay correction factor ΔK_{decay} can be calculated by the following formula:

$$\Delta K_{decay} = \sqrt{\left(\frac{\partial K_{decay}}{\partial s}\Delta s\right)^2 + \left(\frac{\partial K_{decay}}{\partial p_\pi}\Delta p_\pi\right)^2}$$

$$= K_{decay}\frac{m_\pi}{c \cdot \tau_\pi \cdot p_\pi}\sqrt{(\Delta s)^2 + \left(\frac{s}{p_\pi}\Delta p_\pi\right)^2} \tag{6.13}$$

or if a relative uncertainty is used:

$$\Delta K_{decay}^{rel} = 100[\%] \cdot \frac{m_\pi}{c \cdot \tau_\pi \cdot p_\pi}\sqrt{(\Delta s)^2 + \left(\frac{s}{p_\pi}\Delta p_\pi\right)^2} \tag{6.14}$$

Fig. 6.30 shows a distribution of ΔK_{decay}^{rel} for the axialFF_987a setting. Depending on the momentum p_π and the pion path length s the relative uncertainty of the

decay correction factor ΔK^{rel}_{decay} takes different values. For the calculation of the total systematic error a 0.54% value was used, as it represents the highest limit for the ΔK^{rel}_{decay}.
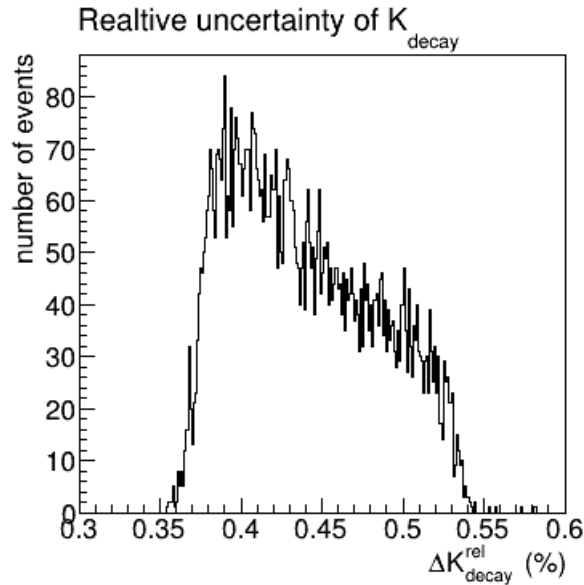
Figure 6.30 — Distribution of the relative uncertainty of the decay correction factor K_{decay} for the axialFF_987a setting.

c) Uncertainties of the muon contamination correction Δ_μ and of the phase space simulation Δ_{ph-sp}. The uncertainty of this correction factor was determined from statistical fluctuations in simulations of the muon contamination with a different number of simulated events. The simulation with the 10^8 events served as a reference. The upper and the lower event values were $1.1 \cdot 10^8$ and $0.9 \cdot 10^8$ respectively. A relative error for the muon contamination correction factor of 0.23% was obtained for all settings. With the same procedure the phase space relative error of 0.12% was estimated too.

d) Uncertainty of SOS drift chamber coordinates Δ_{ch}. The true events for which the left-right decision was done intentionally make up 2.04% of the true events. This correction only includes three drift cells of the X-chamber, for other five drift cells this correction could not be done. Either the wrong reconstructed events lie inside the shaded area (see Fig. 6.22), or the effect is too small (or even non-existent) to observe it on the left side of the shaded area. The 0.68% is the average number of the true events per drift cell for which the left-right decision was performed on purpose and this value is used as the estimate for a relative systematic uncertainty for this effect.

e) Uncertainty of the cut on missing mass Δ_{mm}. When calculating the cross section for the $p(e, e'\pi^+)n$ reaction, the width of the cut on experimental and phase space

missing mass peak has to be equal. The value of the obtained cross section should not be dependent on the mass cut-off along the radiative tail, because for a given cut the number of included true events should correspond to the amount of the included phase space. As reported in [11] and [12], but also seen in this experiment, expanding the width of the cut increases the value of the cross section, see Fig. 6.31. What actually causes the mismatch is not yet fully understood. A reason for such behaviour can be a non-perfect matching of the experimental and the phase space radiation tails, caused by not precise enough determination of different energy loss corrections. It is also important to notice, that high cut-off values take into account bins which suffer from the high statistical errors, since they contain a small number of the experimental and the simulated events.
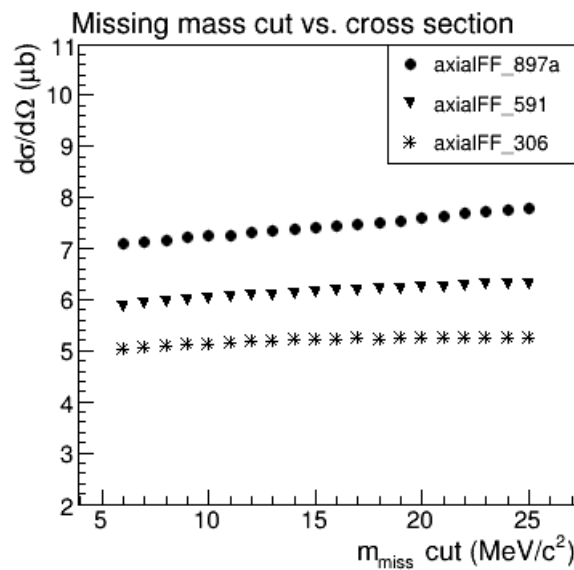
Figure 6.31 — Dependence of the $p(e, e'\pi^+)n$ cross section on the missing mass cut. Although the cross section should not depend on the value of the missing mass cut, the increase of the cut-off value causes a small rise of the cross section.

For all kinematical settings a 11 MeV/c^2 cut-off mass was used for the Rosenbluth separation and the TL term determination. For each setting the cross section was also calculated for the 6 and 16 MeV/c^2 boundary cut-offs. The estimated systematic error for the missing mass cut was determined by a standard deviation method. Depending on the setting, the errors were between 2.4% and 3.2%.

f) Uncertainty of the snow correction Δ_{snow}. Even with fine variations of the snow thickness no perfect matching between the experimental and the simulated missing mass peak could be accomplished. The analysis was repeated with two boundary values for the snow thickness: -0.2 mm and $+0.2$ mm from the optimal value. The calculated standard deviation was used as the estimate of the systematic error of 0.09%.

The total systematic error is calculated as a square root of the sum of the squared individual contributions:

$$\Delta_{total} = \sqrt{(\Delta L)^2 + (\Delta K_{decay})^2 + (\Delta_\mu)^2 + (\Delta_{ph\_sp})^2 + (\Delta_{ch})^2 + (\Delta_{mm})^2 + (\Delta_{snow})^2}$$

$$(6.15)$$

6.2 Elastic measurements

Results of the elastic electron scattering on protons $p(e, e')$ are given in this section. The cross section for this process is very well known, and a comparison of the experimental data with the theoretical prediction serves only as a verification of spectrometer A performance. Six different kinematical settings, listed in table 5.2, were measured.

The missing mass peak now appears at a place of the proton mass. The dead time corrected luminosity L is determined with Lumi++ and the phase space Φ covered by spectrometer A is calculated with Simul++. All efficiencies of spectrometer A are known and the evaluation of the elastic cross section is straightforward:

$$\frac{d\sigma_{el}}{d\Omega_e} = \frac{N_{true}}{L \cdot \Phi} \cdot \epsilon_{total}$$

$$(6.16)$$

The theoretical cross section is given by equation 2.32. The spline parameterization of the electric and the magnetic form factors was used from [36]. The cross section of the elastic electron scattering is plotted as a function of the electron scattering angle θ_e. The theoretical cross section is plotted with a red line and the measured cross section is represented by blue points with error bars. Only statistical errors of the simulated phase space and of the measured data were used for the calculation of the error bars.

Comparisons of the experimental data and the theory are shown on Fig. 6.32. In the middle of the spectrometer acceptance the agreement of the experimental data and the theory is very good. Only at the edges there are bigger discrepancies because the spectrometer acceptance for these angles no longer covers the full phase space. The best agreement between the theory and the experiment was obtained for settings with the highest beam energy. With a decreasing of the beam energy the agreement becomes slightly worse. Due to high particle rate, the elastic measurement has to be performed with low beam current (around 1 μA). This worsens the precision of the beam current measurement by the Förster probe, which deteriorates even more with the decreasing of the beam energy and the corresponding number of recirculations in the third RTM. Therefore, for low beam energy settings (elastic_345a/b and elastic_450a/b) the luminosity is determined less precisely, causing the small discrepancy between the theory and the experiment. But general, the spectrometer A performed very well.
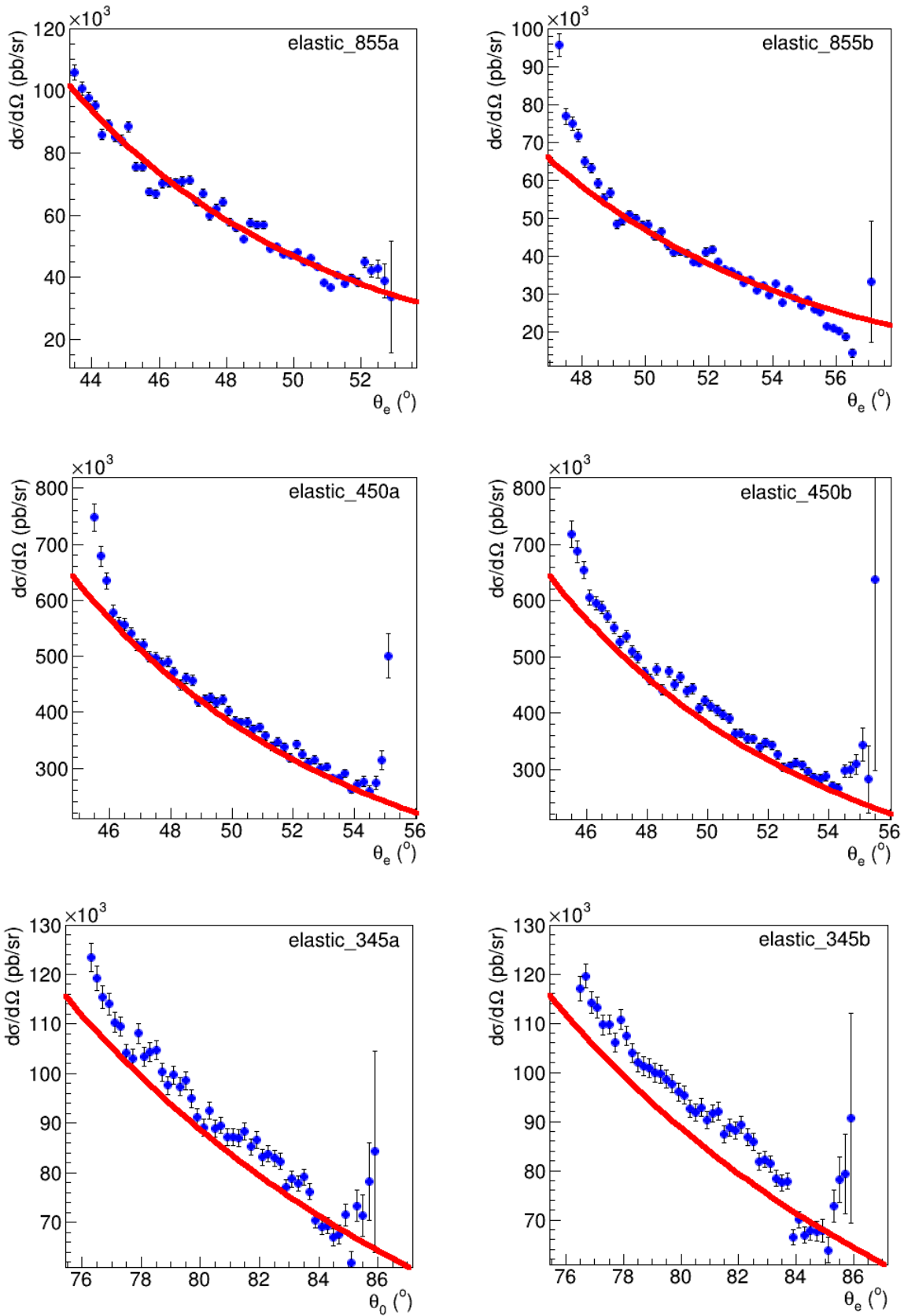
Figure 6.32 — The elastic cross sections $p(e, e')$ as a function of the electron scattering angle θ_e. The experimental data is labeled by blue points, theoretical model is shown by the red line.

7

Results and Outlook

In this chapter results of the analysis of the $p(e, e'\pi^+)n$ data will be presented. Starting in 7.1 with a discussion of the final missing mass spectra obtained in the data analysis for each kinematical setting and corresponding cross section. Results of the Rosenbluth separation and the extracted TL term of the cross section are presented in section 7.2 and compared with selected models in section 7.3. Finally, the conclusion and the outlook for further research are given in section 7.4.

7.1 Experimental results

For a decent Rosenbluth separation and an acceptable statistical error at least 5000 true events per kinematical setting have to be measured. This condition was verified for each kinematical setting by integrating only the background corrected missing mass histogram over the analysis interval from -3 to 11 MeV/c^2 (the data obey all other cuts, but no corrections were applied). Table 7.1 shows that the "5000" goal was successfully fulfilled for each kinematical setting. The time needed to achieve this goal was different for each setting and was mainly influenced by the pion production rate at a particular angle at which SOS was placed, by the value of the beam current (limited by the cooling power of the Philips machine) or by the maximum particle rate which the detector packages of spectrometers can accept. The measurement time, the average beam current, the dead time corrected luminosity and the phase space covered by spectrometers in -3 to 11 MeV/c^2 interval are also presented in table 7.1 for each kinematical setting.

After repeating the data analysis and phase space simulation with the final, above mentioned, cuts and adjustments, as well as applying all necessary corrections, the cross section of the $p(e, e'\pi^+)n$ reaction was determined for each kinematical setting. Here it is important to mention that from the procedures for determining the pion de-

cay correction factor described in section 6.1.8.6, the cross section values in table 7.2 were calculated using the averaging over 1 MeV/c wide pion momentum intervals, since the averaging over 10 mm wide particle length intervals gives only 0.08% different values. The results are presented in table 7.2, together with the total, the statistical and the systematic errors. In all kinematical settings the systematic error is about 3 times larger than the statistical error. The biggest contribution to the total systematic error comes from the missing mass cut on the radiation tail. Depending on the kinematical setting, the relative missing mass cut error alone amounts to the interval between 2.4% and 3.2%. The reason for such big error is the non-perfect overlapping of the experimental and the simulated radiation tails (Fig. 6.26) caused either by simulation parameters and/or by low statistics in the radiation tail of the experimental data.

Table 7.1 — N_{run} is the number of runs or in other words the number of data files recorded for a particular setting, N_{corr} is the number of the true events after background subtraction for the missing mass cut from -3 to 11 MeV/c^2, *Dead* is the averaged dead time percentage, T is the total time of data taking for the particular setting, $\bar{I}$ is the averaged beam current, L_{corr} is the dead time corrected integrated luminosity and Φ is the phase space accepted by the apparatus for the missing mass cut from -3 to 11 MeV/c^2.

Setting	N_{run}	N_{corr}	*Dead* (%)	T (h:min:s)	$\bar{I}$ (μA)	L_{corr} (1/pb)	Φ (10^{-10} sr)
axialFF_306	221	7046	7.8	104 : 02 : 57	17.708	3126545	7.00198
axialFF_591	84	9860	6.5	40 : 54 : 43	20.968	1470661	17.4821
axialFF_897a	29	8179	5.4	13 : 08 : 58	7.961	181920	94.5037
axialFF_897L	41	10235	7.7	19 : 35 : 44	10.860	361032	80.5353
axialFF_897R	34	13379	6.5	16 : 44 : 32	9.917	285110	80.5124

Table 7.2 — The results of the $p(e, e'\pi^+)n$ cross section measurement at $Q^2 = 0.078$ (GeV/c)^2.

Setting	$d\sigma/d\Omega_\pi^\star$ (μb/sr)	$\pm$	total error (μb/sr)	stat. error (μb/sr)	syst. error (μb/sr)
axialFF_306	4.91	$\pm$	0.15 (3.1%)	0.06 (1.2%)	0.14 (2.9%)
axialFF_591	5.73	$\pm$	0.21 (3.7%)	0.06 (1.1%)	0.20 (3.5%)
axialFF_897a	6.83	$\pm$	0.24 (3.5%)	0.08 (1.2%)	0.23 (3.4%)
axialFF_897L	5.37	$\pm$	0.18 (3.4%)	0.05 (0.9%)	0.17 (3.1%)
axialFF_897R	8.53	$\pm$	0.27 (3.2%)	0.07 (0.8%)	0.26 (3.1%)

7.2 Determination of the L, T and TL terms

For the extraction of the L and T terms from the total cross section $d\sigma/d\Omega_\pi^\star$ of the charged pion electroproduction at $Q^2 = 0.078\,(\mathrm{GeV}/c)^2$ and $W = 1094\,\mathrm{MeV}$ the Rosenbluth method was used. The values of the cross section in parallel kinematics were plotted as a function of the transverse virtual photon polarization ϵ, see Fig. 7.1. As expected from the equation 2.20 data points lie on the straight line.
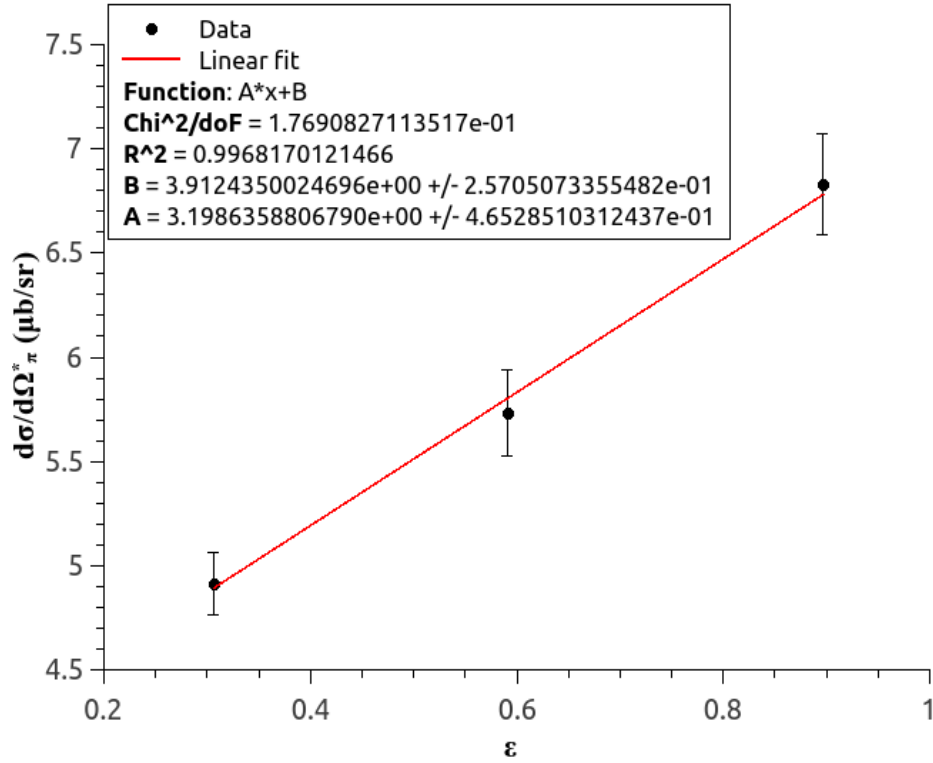
Figure 7.1 — Rosenbluth separation.

Table 7.3 — The T, L and TL terms of the $p(e, e'\pi^+)n$ cross section at $Q^2 = 0.078\,(\mathrm{GeV}/c)^2$ and $W = 1094\,\mathrm{MeV}$.

Cross section term	value (μb/sr)	±	total error (μb/sr)	stat. error (μb/sr)	syst. error (μb/sr)
$d\sigma_T$	3.91	±	0.26 (6.7%)	0.10 (2.6%)	0.24 (6.1%)
$d\sigma_L$	3.20	±	0.47 (14.7%)	0.16 (5.0%)	0.44 (13.8%)
$d\sigma_{LT}$	-0.86	±	0.09 (10.5%)	0.02 (2.3%)	0.08 (9.3%)

Using the linear regression the total cross section $d\sigma/d\Omega_\pi^\star$ was separated into the L and T terms, the linear regression was performed three times to include the influence

of the total, the statistical and the systematic error separately, see table 7.3. If no errors are included for the $d\sigma/d\Omega_\pi^\star$ data, the linear regression gives relative errors of 3.4% for the T term and 6.3% for the L term.

Models in next section define the factorization of the total cross section into cross section terms slightly different from those stated in equations 1.1 and 2.19. The models use only ϵ in the factorization. $\epsilon_L^\star$ is not used [47]! Hence, the TL term, presented in table 7.3, was calculated by using:

$$\frac{d\sigma_{TL}}{d\Omega_\pi^\star} = \frac{\left.\dfrac{d\sigma_L}{d\Omega_\pi^\star}\right|_{\Phi_\pi=0°,\theta_\pi^\star=18.7°} - \left.\dfrac{d\sigma_R}{d\Omega_\pi^\star}\right|_{\Phi_\pi=180°,\theta_\pi^\star=-18.7°}}{2\sqrt{2\epsilon(1+\epsilon)}} \tag{7.1}$$

7.3 Comparison of experimental results and model predictions

The results for the L, T and TL terms of the total cross section were compared with results of three theoretical models, which can be accessed via web interface [47].

The first model is the Dubna-Mainz-Taipei model or simply DMT2001. The calculations are done within a meson-exchange dynamical model describing most of the existing pion electromagnetic production data up to the second resonance region. The model uses potentials derived from an effective chiral Lagrangian [48]. Further details about the model can be read in [48–50].

The second model is based on the partial-wave analysis with a Mainz unitary isobar model MAID. The model is constructed with nucleon resonances and a non-resonant background. From the first version in year 1998, the unitary isobar model has been improved several times. Hence, the version MAID2007 [51] includes a full set of total 13 nucleon resonances for energies below 2 GeV with transverse electric, transverse magnetic and Coulomb couplings. The resonances are described by appropriately unitarized Breit-Wigner forms. The non-resonant background is described by the pion electroproduction potential containing contributions from the Born terms described by an energy-dependent mixing of pseudovector and pseudoscalar πNN coupling and a t-channel vector meson exchange. The Q^2 dependence of the s- and u-channel nucleon pole terms of the background is described by the form factors from [52]. At electromagnetic vertex of the pion-pole a monopole form for the pion form factor was applied, at the vertex of the seagull term a dipole form for the axial form factor, and the standard dipole form factor was used for the vector-meson exchange. The background is unitarized using the K-matrix procedure. Parameters are obtained by both single-energy

and global fits of the world data base of pion photo- and electroproduction [51].

The third model is the Chiral MAID (χMAID) [53]. It provides calculation of the pion photo- and electroproduction in Lorentz-invariant baryon chiral perturbation theory up to and including order q^4. The low-energy constants are fixed by fitting experimental data in all available reaction channels. In a web-based application calculation of a complete amplitude is avoided due to long computing time. The input of χMAID is restricted to multipoles up to and including $l = 4$ (G waves). All observables are derived from the multipoles which have been computed beforehand for all reaction channels. The calculation of the multipoles is performed for an energy range $W = 1073.3 - 1190$ MeV, and for electroproduction through $Q^2 = 0.3$ (GeV/c)^2 [53]. The loop contributions and their parameters have fixed values and they cannot be changed via web interface. The contact diagrams at $O(q^3)$ and $O(q^4)$ enter analytically and the corresponding low-energy constants can be changed arbitrarily. More details can be found in [53].

Table 7.4 — The T, L and TL calculations based on selected models.

Model	$d\sigma_T$ (μb/sr)	$d\sigma_L$ (μb/sr)	$d\sigma_{TL}$ (μb/sr)
DMT2001	4.38	3.33	-0.79
Maid2007	4.39	4.22	-0.98
χMAID	4.73	2.89	-1.11
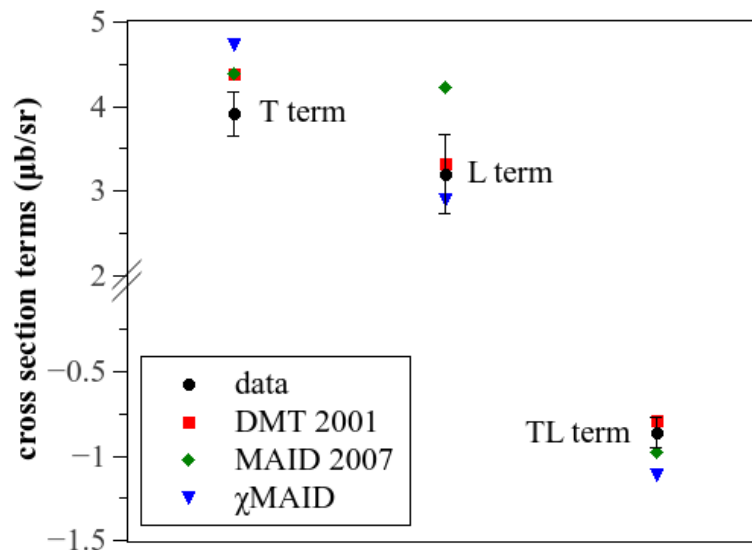
Figure 7.2 — The experimental and the model predictions for the T, L and TL terms.

The prediction of the theoretical models for T, L and TL pion electroproduction

terms at $Q^2 = 0.078$ (GeV/c)^2 and $W = 1094$ MeV is presented in table 7.4. Here it is important to mention that χMAID results were obtained using low-energy constants which were adjusted for the past charged pion electroproduction experiments [53].

For more convenient comparison the experimentally obtained terms with the total errors were plotted on the same graph together with the model predictions, see Fig. 7.2. All models overestimate the value of the T term. In the case of the DMT2001 and the Maid2007 the overestimation is around 10.7% and around 17.3% for the χMAID. On the other hand, in the case of the L term the predictions of the χMAID and the DMT2001 are very near to the experimental value, but the Maid2007 predicts a somewhat higher value. For the TL term, the DMT2001 prediction is inside the error bar, MAID2007 is very near to the bar and χMAID is slightly more outside the bar.

7.4 Conclusion and Outlook

The electroproduction of positively charged pions on the proton has been measured at the invariant mass $W = 1094$ MeV and four-momentum transfer $Q^2 = 0.078$ (GeV/c)^2. The scattered electron was detected in the spectrometer A in coincidence with produced charged pion detected in the SOS. For the first time the complete analysis of the pion data measured with SOS was successfully performed for five kinematical settings. This included introduction of SOS specific corrections, as well as a new Simul++ option for Monte Carlo simulation of pion decay in SOS. The statistical errors of the measured cross sections were between 0.8% and 1.2% and the systematic errors were estimated to be between 2.9% and 3.5%.

By using the Rosenbluth method the total pion electroproduction cross section was separated into longitudinal and transversal cross sections, which suffer from relatively high total error 14.7% and 6.7%, respectively. In addition, the longitudinal-transversal interference cross section was also extracted, having total error of 10.5%. The experimental values have been compared with predictions of three selected models. For the transversal cross section the models overestimate the experimental value by less than 17.3%. In case of longitudinal component the predictions of the χMAID and the DMT2001 are inside the experimental error bar, but the Maid2007 gives 24.2% larger value than the experiment. DMT2001 and MAID2007 predict the longitudinal-transversal interference cross section term very close to the experimental value, whereby the DMT2001 prediction is somewhat better. Here, the prediction of χMAID is approximately 22.5% higher. Again, χMAID results were obtained by using low-energy constants optimized for previous pion electroproduction experiments [53].

In future there are many possibilities to reduce rather high systematic errors. For

example, new transfer matrices for the drift chambers would improve the reconstruction of non-dispersive coordinates (ϕ_0, y_0) and related quantities for both spectrometers. In case of spectrometer A the work is in progress. Measurement with the thin carbon foils placed one after another was already performed, and at the time when this thesis is written the data is being evaluated. Similar calibration measurement should also be performed with SOS. Another thing which should reduce the systematic error is creation of the field map for the SOS dipole magnet. This would allow adding the magnetic fringe fields into the simulation and the particle behaviour inside the SOS would be reproduced more accurately.

The extracted transversal cross section at $W = 1094$ MeV and $Q^2 = 0.078$ (GeV/c)^2 is a data point, which defines the behaviour of the axial nucleon form factor G_A at low Q^2. With the SOS it is possible to detect pions with momenta less than 113 MeV/c and this gives us opportunity, to determine the behaviour of the G_A at even lower Q^2 in future experiments.

At the reaction threshold the longitudinal cross section is dominated by the induced pseudoscalar form factor G_P. Since this experiment was performed approximately 15 MeV above the reaction threshold, we have determined the longitudinal cross section term close enough to the threshold and obtained a first Q^2 point for extraction of the induced pseudoscalar form factor G_P. Further experiments are needed to obtain the longitudinal cross section at additional Q^2 values.

The precise measurement of the weak form factors will allow more precise determination of the weak axial nucleon current. The electromagnetic form factors, which define the vector current of the nucleon, are already known with a high precision. All together will contribute to the more detailed description of the nucleon structure and the proprieties which are derived from it.
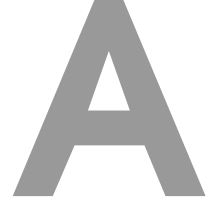
Cuts and analysis parameters

This section contains full summary of all cuts and parameters used in the analysis of the $p(e, e'\pi^+)n$ reaction measurement at $Q^2 = 0.078$ (GeV/c)^2.

Table A.1 — Global and kinematical setting depended cuts used in the analysis of the experimental data. Only the kinematical setting depended cuts were also used in the phase space simulations. T_{A-SOS} refers to the corrected time spectrum of the coincidence TDC, Z_v is the Z-coordinate of the reconstructed vertex in spectrometer A, $dE1$ and $dE2$ denote an ADC value of the energy deposition in a certain scintillator layer of the SOS, m_{miss} is the missing mass, E' is the energy of the scattered electron, θ_0 and δp_0 are dispersive target coordinates of SOS.

Global cuts, same for all kinematical settings	
Coincidence cut (ns)	$-2.0 \leq T_{A-SOS} \leq 2.5$
Background cut (ns)	$-50.0 \leq T_{A-SOS} \leq -10.0$ $7.0 \leq T_{A-SOS} \leq 18.0$
Vertex cut Z_v (mm)	$-50.0 \leq Z_v \leq 50.0$
SOS scint. cut (chan.)	$dE1 > 260$ and $dE2 > 280$
m_{miss} cut (MeV/c^2)	$-3.0 \leq m_{miss} \leq -11.0$

Kinematical setting depended cuts, momentum acceptance		
Setting	Spectrometer A	SOS
	E' (GeV)	θ_0 (mrad), δp_0 (%)
axialFF_306	$0.12127 < E' < 0.14822$	$\theta_0 \geq 0.775 \cdot \delta p_0$ - 15.1145
axialFF_591	$0.21582 < E' < 0.26378$	$\theta_0 \geq$ -0.75$\cdot\delta p_0$ - 12.75
axialFF_897a		$\theta_0 \leq 0.375\cdot\delta p_0$ + 7.0
axialFF_897L	$0.5805 < E' < 0.7095$	$\theta_0 \leq$ -2.0$\cdot\delta p_0$ + 30.0
axialFF_897R		$\theta_0 \leq 1.9\cdot\delta p_0$ + 20.8

Table A.2 — Summarized parameters of the each kinematical setting used in the analysis and the resolutions of the parameters used in simulation of the phase space. E is the energy of the beam, ϵ is the transversal polarization of the virtual photon, p_e is the central momentum of the spectrometer A obtained from the magnetic field measurement and the second number is a correction needed to move the experimental missing mass peak at the position of the bin 0, θ_e is the angle at which the spectrometer A was set, p_π and θ_π are corresponding values for the SOS, ρ_{snow} is the snow density and d is the snow thickness.

Kinematical setting axialFF_306					
Beam	Spectrometer A		SOS		Target/Snow
E (MeV)	p_e (MeV/c)	θ_e (°)	p_π (MeV/c)	θ_π (°)	ρ_{snow} (g/cm^3)
ϵ	Δp_e (MeV/c)	$\Delta\theta_e$ (mrad)	Δp_π (MeV/c)	$\Delta\theta_\pi$ (mrad)	d (mm)
345	134.750 - 0.4	80.70	113.005	22.42	0.4
0.3065	1.1	22.0	0.13	11.0	0.2

Kinematical setting axialFF_591					
Beam	Spectrometer A		SOS		Target/Snow
E (MeV)	p_e (MeV/c)	θ_e (°)	p_π (MeV/c)	θ_π (°)	ρ_{snow} (g/cm^3)
ϵ	Δp_e (MeV/c)	$\Delta\theta_e$ (mrad)	Δp_π (MeV/c)	$\Delta\theta_\pi$ (mrad)	d (mm)
450	239.8 - 0.12	50.30	113.011	31.79	0.4
0.5913	1.5	8.5	0.13	11.0	0.2

Kinematical setting axialFF_897a					
Beam	Spectrometer A		SOS		Target/Snow
E (MeV)	p_e (MeV/c)	θ_e (°)	p_π (MeV/c)	θ_π (°)	ρ_{snow} (g/cm^3)
ϵ	Δp_e (MeV/c)	$\Delta\theta_e$ (mrad)	Δp_π (MeV/c)	$\Delta\theta_\pi$ (mrad)	d (mm)
855	644.698 -0.45	22.50	112.999	42.93	0.4
0.8970	0.15	5.8	0.13	11.0	0.2

Kinematical setting axialFF_897L					
Beam	Spectrometer A		SOS		Target/Snow
E (MeV)	p_e (MeV/c)	θ_e (°)	p_π (MeV/c)	θ_π (°)	ρ_{snow} (g/cm^3)
ϵ	Δp_e (MeV/c)	$\Delta\theta_e$ (mrad)	Δp_π (MeV/c)	$\Delta\theta_\pi$ (mrad)	d (mm)
855	644.762 -0.45	22.50	109.995	32.79	0.4
0.8970	0.15	5.8	0.13	11.0	0.2

Kinematical setting axialFF_897R					
Beam	Spectrometer A		SOS		Target/Snow
E (MeV)	p_e (MeV/c)	θ_e (°)	p_π (MeV/c)	θ_π (°)	ρ_{snow} (g/cm^3)
ϵ	Δp_e (MeV/c)	$\Delta\theta_e$ (mrad)	Δp_π (MeV/c)	$\Delta\theta_\pi$ (mrad)	d (mm)
855	644.698 -0.45	22.50	109.990	53.18	0.4
0.8970	0.15	5.8	0.13	11.0	0.2

Table A.3 — Density ρ (g/cm^3) of a hydrogen target after a given date, which is given as two last digits of a year, month, day, hour, minutes, seconds (*yymmddhhmmss*).

axialFF_306		axialFF_591		axialFF_897R	
date	ρ (g/cm^3)	date	ρ (g/cm^3)	date	ρ (g/cm^3)
110421154954	0.0687422	110427171200	0.0685444	110430153712	0.0687533
110422043000	0.0687291	110427173000	0.0684654	110430154012	0.0686361
110422084700	0.0689232	110427183000	0.0684324	110430155836	0.0685837
110422090500	0.0687810	110428032000	0.0684126	110430163012	0.0687663
110422093106	0.0685199	110428075700	0.0683064	110430163712	0.0686882
110422094006	0.0687940	110428100600	0.0687924	110430164212	0.0685706
110422095106	0.0686248	110428103630	0.0685837	110501000000	0.0685180
110422100900	0.0686639	110428105300	0.0685575	110501005400	0.0685574
110422103000	0.0686900	110428115800	0.0685312	110501014800	0.0685706
110422150600	0.0686770	110428134900	0.0685049	110501043100	0.0688311
110422182100	0.0686639	110428143800	0.0684785	110501052932	0.0686622
110422201400	0.0686509	110428203200	0.0684521	110501054600	0.0685967
110423000000	0.0686769	110429000000	0.0684125	110501071000	0.0685705
110424030800	0.0687151	110429060000	0.0683860	axialFF_897a	
110424042512	0.0688059	110429082000	0.0687533	date	ρ (g/cm^3)
110424053936	0.0687215	110429090440	0.0685574	110501103000	0.0688051
110424081554	0.0687993	110429091500	0.0684917	110501105900	0.0686621
110424155754	0.0689863	110429092700	0.0684521	110501124000	0.0686229
110424161254	0.0688187	110429095200	0.0684124	110501140700	0.0688569
110424224012	0.0689734	110429105800	0.0683859	110501155000	0.0687402
110424231512	0.0687733	110429115430	0.0688827	110501160900	0.0686490
110425000000	0.0687343	axialFF_897L		110501173800	0.0687143
110425180024	0.0689347	date	ρ (g/cm^3)	110501174000	0.0686490
110425183524	0.0688961	110429161900	0.0689215	110501182100	0.0686098
110425204642	0.0687147	110429164200	0.0687194	110501194800	0.0685770
110425223542	0.0686886	110429193900	0.0687012	110502000000	0.0686228
110426043400	0.0686625	110429204042	0.0686360		
110426085430	0.0689089	110429215000	0.0686099	elastic_345a and elastic_345b	
110426103118	0.0687016	110430051000	0.0685706	date	ρ (g/cm^3)
110426110006	0.0686755	110430080042	0.068636	110427112906	0.0688829
110426112454	0.0689282	110430085700	0.0685837	elastic_450a and elastic_450b	
110426121318	0.0686755	110430100000	0.0685574	date	ρ (g/cm^3)
110426143418	0.0686494	110430115000	0.0685443	110430145412	0.0688440
110427000000	0.0686232	110430143218	0.0687404	elastic_855a and elastic_855b	
110427112906	0.0688829	110430143730	0.0686753	date	ρ (g/cm^3)
		110430144012	0.0685706	110421104000	0.0689230
		110430145412	0.0688440		

B

Trajectory length determination in SOS

The calculation of the pion trajectory length s is made in four steps. First the length from the target to the entrance inside the magnetic field is calculated, in this step the entrance coordinates are obtained too. Then the length from the top plane of the magnet yoke to the particle exit out of the magnet field is determined together with exit coordinates. The third step is a calculation of the length from the top plane of the magnet yoke to the top plane of the scintillator telescope. The final step is determination of the particle trajectory inside the magnetic field. The total length s is the sum of mentioned contributions. In the following text each step will be explained in detail.

The reconstructed target coordinates $(\delta p_0, \theta_0, y_0, \phi_0)$ and a position of the magnet are needed for the determination of the distance from the target to the entrance inside the magnet s_{t-m}. Starting from the definition of the target coordinates (θ_0 and ϕ_0), see Fig. 6.18, we can write:

$$\tan \theta_0 = \frac{x}{z}$$

$$\tan \phi_0 = \frac{y}{z}$$

(B.1)

The length r of a vector $\vec{r}$ in a 3D Cartesian coordinate system can be expressed as:

$$r^2 = x^2 + y^2 + z^2$$
(B.2)

The definition B.1 and B.2 can be used to express components of the Cartesian system (x, y, z) in terms of target coordinates (θ_0 and ϕ_0):

$$x = r \left[1 + \frac{\tan^2 \phi_0}{\tan^2 \theta_0} + \frac{1}{\tan^2 \theta_0} \right]^{-1/2} \qquad \text{or substitution} \qquad x = r \cdot a$$

$$y = r \left[1 + \frac{\tan^2 \theta_0}{\tan^2 \phi_0} + \frac{1}{\tan^2 \phi_0} \right]^{-1/2} \qquad \text{or substitution} \qquad y = r \cdot b \qquad \text{(B.3)}$$

$$z = r \left[1 + \tan^2 \theta_0 + \tan^2 \phi_0 \right]^{-1/2} \qquad \text{or substitution} \qquad z = r \cdot c$$

Hence, the position of the particle, which is emitted from the target with start/target coordinates (y_0, θ_0, ϕ_0), is in the Cartesian coordinate system defined by $(r \cdot a, r \cdot b + y_0, r \cdot c)$.

The entrance inside the magnet, in the target coordinate system, is defined with:

$$x^2 + (z - Z_0)^2 = R^2 \qquad \text{(B.4)}$$

where $Z_0 (= 1131.6 \ mm)$ is the position of the SOS magnet centre and $R (= 350 \ mm)$ is the radius of the magnet pole shoes.

The length from the target to the entrance inside the magnetic field can now be calculated by using equations B.3 and B.4:

$$a^2 \cdot r^2 + (c \cdot r - Z_0)^2 = R^2$$

$$\qquad \text{(B.5)}$$

$$(a^2 + c^2) \cdot r^2 - 2cZ_0 \cdot r + Z_0^2 - R^2 = 0$$

We obtained a quadratic equation in r, which can be easily solved: B.4:

$$r_{1/2} = \frac{2cZ_0 \pm \sqrt{(-2cZ_0)^2 - 4(a^2 + c^2)(Z_0^2 - R^2)}}{2(a^2 + c^2)} \qquad \text{(B.6)}$$

From the two solutions for r, our problem is described with the one, which has the minus sign in front of the square root term:

$$s_{t-m} = r_{t-m} = \frac{cZ_0 - \sqrt{(cZ_0)^2 - (a^2 + c^2)(Z_0^2 - R^2)}}{(a^2 + c^2)} \qquad \text{(B.7)}$$

Keeping in mind the sign of angles θ_0 and ϕ_0, the particle entrance coordinates inside the magnetic field can also be calculated now:

$$x_{m-in} = r_{t-m} \cdot a \quad (if\ \theta_0 > 0) \quad or \quad -r_{t-m} \cdot a \quad (if\ \theta_0 < 0)$$

$$y_{m-in} = r_{t-m} \cdot b + y_0 \quad (if\ \phi_0 > 0) \quad or \quad -r_{t-m} \cdot b + y_0 \quad (if\ \phi_0 < 0) \qquad \text{(B.8)}$$

$$z_{m-in} = r_{t-m} \cdot c$$

For the calculation of the particle length s_{j-m} from the top plane of magnet yoke to the point of exit from the magnetic field, the chamber coordinates $(x_{ch}, \theta_{ch}, y_{ch}, \phi_{ch})$ and a position of the SOS dipole magnet are used. The calculation is performed in the detector coordinate system, see Fig. 6.18. In this coordinate system the position of the particle is defined with:

$$x = x_{ch} + z \cdot \tan \theta_{ch}$$

$$y = y_{ch} + z \cdot \tan \phi_{ch} \qquad \text{(B.9)}$$

$$z = z$$

The edge of the magnetic field, in the detector coordinate system, is also defined with:

$$x^2 + (z - Z_0)^2 = R^2 \qquad \text{(B.10)}$$

but here the position of the SOS magnet centre is $Z_0 = -608$ mm.

The intersection of the particle trajectory and the edge of the magnetic field is obtained by combining the equation for x coordinate B.9 and the equation B.10:

$$(x_{ch} + z \cdot tan\theta_{ch})^2 + (z - Z_0)^2 = R^2$$

$$\qquad \text{(B.11)}$$

$$(1 + \tan^2 \theta_{ch}) \cdot z^2 + (-2Z_0 + 2x_{ch} \tan \theta_{ch}) \cdot z + x_{ch}^2 + Z_0^2 - R^2 = 0$$

Solving the quadratic equation B.11 following solutions are obtained:

$$z_{1/2} = \frac{-(-Z_0 + x_{ch} \tan \theta_{ch}) \pm \sqrt{(-Z_0 + x_{ch} \tan \theta_{ch})^2 - (1 + \tan^2 \theta_{ch})(x_{ch}^2 + Z_0^2 - R^2)}}{1 + \tan^2 \theta_{ch}}$$

$$\qquad \text{(B.12)}$$

This particular problem is described with solution B.12 which has plus sign in front of the square root term:

$$z_{j-m} = \frac{(Z_0 - x_{ch} \tan \theta_{ch}) + \sqrt{(-Z_0 + x_{ch} \tan \theta_{ch})^2 - (1 + \tan^2 \theta_{ch})(x_{ch}^2 + Z_0^2 - R^2)}}{1 + \tan^2 \theta_{ch}}$$

$$\qquad \text{(B.13)}$$

The particle exits the magnetic field at the point defined by:

$$x_{m-ex} = x_{ch} + z_{j-m} \cdot \tan \theta_{ch}$$

$$y_{m-ex} = y_{ch} + z_{j-m} \cdot \tan \phi_{ch} \tag{B.14}$$

$$z_{m-ex} = z_{j-m}$$

Finally, the length from the top plane of magnet yoke to the point of exit from the magnetic field is now:

$$s_{j-m} = \sqrt{(x_{ch} - x_{m-ex})^2 + (y_{ch} - y_{m-ex})^2 + z_{m-ex}^2} \tag{B.15}$$

The calculation of the length $s_{j-scint}$ from the top plane of the magnet yoke to the top plane of the scintillator telescope is rather straightforward, because in the z coordinate this distance equals 237 mm:

$$s_{j-scint} = \sqrt{(237 \cdot \tan \theta_{ch})^2 + (237 \cdot \tan \phi_{ch})^2 + 237^2} \tag{B.16}$$

The final step is determination of the trajectory length s_m inside the magnetic field. The entrance B.8 and the exit point B.17 are given in different coordinate systems, therefore we will first of all transform the exit coordinates into the target coordinate system:

$$x_{m-ex}^{tg} = -1 * (z_{m-ex} + 608.0)$$

$$y_{m-ex}^{tg} = y_{m-ex} \tag{B.17}$$

$$z_{m-ex}^{tg} = 1131.6 + x_{m-ex}$$

In target coordinate system the magnetic field of the SOS dipole magnet has only one component, namely $\vec{B} = B \cdot \vec{y}$. Therefore, the magnetic field will affect the particle trajectory only in the dispersive plane, defined by coordinates x and z (movement in y will not be affected by this magnetic field). We continue with calculation of the straight line distance between the entrance and the exit point in the dispersive plane:

$$d_{in-ex} = \sqrt{(x_{m-in} - x_{m-ex}^{tg})^2 + (z_{m-in} - z_{m-ex}^{tg})^2} \tag{B.18}$$

The radius R_m of the trajectory inside the magnetic field is defined by the momentum p and the magnitude of magnetic field B:

$$R_m = \frac{p \cdot 10^{12}}{c \cdot B} [mm] \tag{B.19}$$

To obtain R_m in millimetres p has to be in GeV/c, c is the speed of light in m/s, B has to be in units of T. Now we can calculate the β angle which a particle makes when travelling on a circular trajectory of a radius R_m from the entrance to the exit point:

$$\beta = 2 \cdot \arccos \frac{\sqrt{R_m^2 - (d_{in-ex}/2)^2}}{R_m} \tag{B.20}$$

The arc length in the dispersive plane is now:

$$s_{arc} = \beta \cdot R_m \tag{B.21}$$

and the length of the particle inside the magnetic field is:

$$s_m = \sqrt{s_{arc}^2 + (y_{m-in} - y_{m-ex}^{tg})^2} \tag{B.22}$$

Finally, the total length s of the particle inside the SOS is a sum of B.7, B.15, B.16 and B.23:

$$s = s_{t-m} + s_{j-m} + s_{j-scint} + s_m \tag{B.23}$$

8

Prošireni sažetak

8.1 Uvod

Tijekom posljednjih nekoliko desetljeća postignut je veliki napredak u razumijevanju strukture nukleona, međutim neke veličine bitne za opis strukture još uvijek nisu poznate sa željenom preciznošću. Nukleon nije točkasta čestica, ima složenu strukturu i konačnu dimenziju, a većina podataka o veličini i strukturi nukleona dobivena je u eksperimentima s elektronskim raspršenjem. Na niskim prijenosima četveroimpulsa Q^2, interakcija elektrona i nukleona mete može se aproksimirati s izmjenom jednog virtualnog fotona. Budući da je ta interakcija elektromagnetska, vrlo je jednostavna i dobro poznata u okviru kvantne elektrodinamike (QED).

Energija i količina gibanja virtualnog fotona mogu se varirati neovisno jedno o drugom i te su veličine dobro definirane s energijom i količinom gibanja upadnog i raspršenog elektrona. Ako energiju virtualnog fotona držimo fiksnom i samo mijenjamo njegovu količinu gibanja, možemo mapirati tzv. form-faktore. U sustavu u kojem nema prijenosa energije (Breitov sustav), form-faktori se (na niskim Q^2) mogu interpretirati kao trodimenzionalni Fourierovi transformati gustoće naboja, gustoća struja i gustoća prijelaza. Tada inverzne Fourierove transformacije form-faktora daju prostorne raspodjele tih gustoća u nukleonu [1, 2].

Precizno mjerenje udarnog presjeka elektroprodukcije nabijenog piona na protonu $(p(e, e'\pi^+)n)$, blizu praga reakcije, otvara nam mogućnost da istražimo jedan dio strukture nukleona. Kako se emisijom nabijenog piona mijenja stanje početnog nukleona, taj je proces osjetljiv na dio nukleonske strukture slabog aksijalnog vektora i pripadnih form-faktora: aksijalnog form-faktora i induciranog pseudoskalarnog form-faktora [3]. Aksijalni form-faktor povezan je sa spin-izospinskom raspodjelom u nukleonu [4], a inducirani pseudoskalarni form-faktor povezan je s pionskim polom.

Virtualni foton nosi i transverzalnu ϵ i longitudinalnu $\epsilon_L^\star$ polarizaciju. Ta činjenica, u udarnom presjeku koji opisuje interakciju virtualnih fotona s protonskom metom, rezultira s pojavom transverzalnog T, longitudinalnog L, te interferencijskih (TL i TT) članova. U slučaju nepolariziranog snopa elektrona i protonske mete, udarni presjek se može faktorizirati kao u jednadžbi 1.1 [5, 6]. Ovdje su najvažniji T i L članovi. Naime, T član se može direktno povezati s aksijalnim form-faktorom, dok L član kao jedan od doprinosa sadrži i inducirani pseudoskalarni form-faktor.

T i L članove udarnog presjeka moguće je eksperimentalno separirati. Za to su potrebna mjerenja u tzv. paralelnoj kinematici, u kojoj se proizvedeni pion detektira u smjeru virtualnog fotona (kut produkcije piona $\theta_\pi = \theta_\pi^\star = 0°$, * označava veličine u sustavu centra mase). Kako interferencijski članovi udarnog presjeka imaju eksplicitnu ovisnost tipa $d\sigma_{TL} \sim sin\theta_\pi^\star$ i $d\sigma_{TT} \sim sin^2\theta_\pi^\star$, oni iščezavaju u paralelnoj kinematici, pa u udanom presjeku ostaju samo T i L članovi [5, 6]. Ideja je da se na fiksnoj vrijednosti invarijantne mase W i prijenosa četveroimpulsa Q^2 mjerenje udarnog presjeka ponovi na različitim vrijednostima polarizacije virtualnog fotona ϵ ($\epsilon_L^\star$), koje se mogu precizno kontrolirati pomoću kinematike elektrona. T i L članovi se sada ponašaju kao koeficijenti u jednadžbi pravca, te ih se jednostavno može odrediti linearnom regresijom. Ovaj postupak se zove Rosenbluthova separacija [7].

Također je, dosta jednostavno, moguće eksperimentalno izdvojiti i TL interferencijski član. Za to su dovoljna dva mjerenja na istim vrijednostima W, Q^2 i ϵ. Jedno mjerenje treba se napraviti na $\theta_\pi^\star \neq 0$ i $\phi_\pi = 0°$, a drugo na istom kutu $\theta_\pi^\star$, ali za $\phi_\pi = 180°$ (u ovom slučaju ravnina, koju definiraju vektori količine gibanja virtualnog fotona i količine gibanja piona, je okrenuta naglavačke), vidi sliku 2.2. Drugim riječima, mjerenja udarnog presjeka se trebaju napraviti za isti kut, lijevo i desno, u odnosu na smjer virtualnog fotona [6]. Kako se u obje navedene kinematike iznosi T, L i TT članova ne mijenjaju, TL član je jedini doprinos koji će preživjeti u razlici lijevog i desnog udarnog presjeka.

U okviru pojedinih teorijskih modela strukture nukleona moguće je izračunati iznose T, L i TL članova udarnog presjeka. Stoga precizno izmjereni T, L i TL članovi omogućuju da testiramo, ali i poboljšamo dane modele.

Prva mjerenja udarnog presjeka elektroprodukcije nabijenih piona blizu praga reakcije, te određivanje L i T članova udarnog presjeka u analizi podataka, započela su u sedamdesetim godinama prošlog stoljeća u Frascati-u, Saclay-u, Hamburg-u (DESY), Daresbury-u, Kharkov-u (pogledati [5] i pripadne reference). Dobiveni podaci su iskorišteni da se iz Q^2-ovisnosti T člana udarnog presjeka odredi aksijalni form-faktor. Problem tih mjerenja i pripadnih rezultata je da imaju velike statističke i sistematske greške.

Niz novijih eksperimenata napravljen je u okviru A1 kolaboracije, pri čemu je korišten elektronski akcelerator Mainz Microtoron (MAMI), na Institutu za nuklearnu fiziku Johannes Gutenberg Sveučilišta u Mainzu, Njemačka. Mjerenja udarnog presjeka elektroprodukcije pozitivnog piona na protonu napravljena su na invarijantnoj masi $W = 1125$ MeV, što je otprilike 46 MeV iznad praga reakcije, te na transferima četveroimpulsa od $Q^2 = 0.117$ (GeV/c)^2 [8, 9], $Q^2 = 0.195$ (GeV/c)^2, i $Q^2 = 0.273$ (GeV/c)^2 [10, 11]. Statističke greške mjerenih udarnih presjeka reakcije $p(e, e'\pi^+)n$ kretale su se između 0.7% i 2.3%, dok su pripadne sistematske greške bile između 1.6% i 3.7% [11]. Za svaku Q^2 vrijednost metodom Rosenbluthove separacije određeni su L i T članovi udarnog presjeka, pa je bilo moguće odrediti i aksijalni form-faktor. Kasnije je napravljeno i mjerenje na $Q^2 = 0.058$ (GeV/c)^2 [12], kako bi se proučilo ponašanje L i T članova na nižim prijenosima četveroimpulsa.

Kako mjerenje bliže pragu $p(e, e'\pi^+)n$ reakcije ($W = 1079.14$ MeV odgovara pragu) omogućava pristup još nižim prijenosima četveroimpulsa, u ovom radu prezentirati će se mjerenje i analiza $p(e, e'\pi^+)n$ koincidencijskog eksperimenta na samo $\simeq 15$ MeV iznad praga reakcije. Eksperiment je proveden u okviru A1 kolaboracije, koristeći kontinuiran snop elektrona akceleratora MAMI. Raspršeni elektron detektiran je u spektrometru A, dok je producirani pion detektiran u spektrometru kratke orbite (SOS). Invarijantna masa iznosila je $W = 1094$ MeV, a prijenos četveroimpulsa $Q^2 = 0.078$ (GeV/c)^2. Udarni presjek reakcije $p(e, e'\pi^+)n$ izmjeren je za pet različitih kinematika, tablica 5.1. Tri su udarna presjeka mjerena u paralelnoj kinematici na polarizacijama virtualnog fotona od $\epsilon = 0.897, 0.591$ i 0.306, sa ciljem da se Rosenbluthovom metodom odrede L i T članovi udarnog presjeka. U dva mjerenja udarnog presjeka na $\epsilon = 0.897$, pion je detektiran jednom na $\theta_\pi^\star = -18.7°$ u odnosu na smjer virtualnog fotona, a drugi put na $\theta_\pi^\star = +18.7°$. Na taj je način bilo moguće izdvojiti TL interferencijski član.

Detekcija niskoenergijskih piona je eksperimentalno vrlo zahtjevna. Pioni su nestabilne čestice i imaju vrijeme života od 26.033 ns [13], a njihov dominantni kanal raspada (99.9877% [13]) je raspad u mion i mionski neutrino. Duljine putanja čestica, u svakom od tri standardna spektrometra A1 kolaboracije, iznose otprilike 10 m. Kako se približavamo pragu reakcije, zbog raspada, broj piona koji prolaze kroz detektorski paket spektrometra se smanjuje. Isto tako, vrijeme trajanja eksperimenta koje je potrebno da bi se skupio statistički značajan broj događaja se produžava. Istovremeno broj miona, koji nastaju raspadom piona, se povećava. Od toga će jedan dio miona nastati u smjeru gibanja piona. Takve mione ne možemo eksperimentalno razlikovati od piona, te ćemo ih pogrešno identificirati kao pione, a sistematska greška mjerenja će se povećati. Mionska kontaminacija određuje se pomoću simulacije. SOS je napravljen da bi se navedeni problemi sveli na minimum, a to je ostvareno tako da se duljina putanje čestice skrati na otprilike 1.6 m. Projektiranje, izgradnja i kalibracija detektorskog

sustava SOS-a napravljena je u sklopu diplomskih i doktorskih radova Dagmar Baumann [12, 14] i Matthias-a Ding-a [15, 16]. Uzimajući u obzir novi iznos duljine putanje piona, udio detektiranih piona je znatno povećan, dok je mionska kontaminacija bitno smanjena.

U ovom radu, prvi puta će biti opisana analiza podataka reakcije $p(e, e'\pi^+)n$, koji su mjereni SOS-om. To uključuje razvoj različitih korekcijskih metoda koje su potrebne za konzistentnu analizu podataka, kao što su određivanje efikasnosti detektora, izračun udjela raspadnutih piona, razvoj Monte Carlo simulacije za određivanje mionske kontaminacije itd. Uz korištenje navedenih korekcijskih metoda izmjeren je udarni presjek $p(e, e'\pi^+)n$ reakcije za svih pet kinematika. Fizikalni cilj ovog doktorskog rada potpuno je ispunjen određivanjem T, L i TL članova udarnog presjeka na $W = 1094$ MeV i $Q^2 = 0.078$ (GeV/c)^2.

8.2 Eksperimentalni postav

8.2.1 MAMI akcelerator

MAMI ili punim imenom Mainz Microtron je akcelerator kontinuiranog snopa elektrona. Snop je podijeljen u pulsove elektrona koji se ponavljaju s frekvencijom od 2.45 GHz. Detektori koje koriste eksperimentalne grupe ne mogu razlučiti pojedine pulsove, pa snop djeluje kontinuirano. Akcelerator je u mogućnosti isporučivati struje jakosti u rasponu od 10 pA do 100 μA i energije snopa u intervalu od 180 MeV do 1.6 GeV. Zbog sinkrotronskog zračenja, rasap energije snopa na 855 MeV iznosi 30 keV, dok na energiji od 1.5 GeV iznosi 110 keV. Za sada se akceleracija snopa vrši u pet uzastopnih stupnjeva koje čine: linearni injektorski akcelerator, tri uzastopna jednostrana mikrotrona (RTM) i harmonički dvostrani mikrotron (HDSM) [32, 33]. Tlocrt eksperimentalnih hala zajedno sa shemom akceleratora može se vidjeti na slici 3.1.

Akcelerator može dati dva tipa snopa: nepolarizirani i polarizirani snop. Kod nepolariziranog snopa koristi se termionski izvor elektrona. Navedenim izvorom mogu se postići struje jakosti do 100 μA. Polarizirani elektroni proizvode se fotoelektričnim efektom na kristalima $GaAs$ pomoću polariziranog laserskog svjetla. Polarizacija snopa elektrona iznosi oko 80%. I ovim se izvorom može postići struja jakosti 100 μA. Međutim, da bi se spriječilo oštećenje $GaAs$ kristala jakost struje je ograničena na 20 μA [33].

Za potrebe ovog eksperimenta korišten je izvor nepolariziranog snopa elektrona. HDSM, odnosno posljednji stupanj akceleratora nije korišten. Dovoljna su bila prva četiri stupnja akceleratora, koji su još poznati i pod imenom MAMI B, a omogućavaju raspon energije snopa od 180 do 855 MeV po koracima od 15 MeV.

8.2.2 Sustav meta

Sustav meta nalazi se u vakuumskoj komori koja je smještena u središtu osi rotacije spektrometara. Sam sustav sastoji se od ljestva na koje je moguće pričvrstiti različite čvrste mete kao što su grafit, polietilen, tantal, bakar i sl. Na ljestvama se uvijek nalazi i luminiscentna meta (kromom dopirana Al_2O_3 pločica s otisnutim križićem), koja služi za optimizaciju položaja snopa. Željeni materijal se bira pomicanjem ljestvi u vertikalnom smjeru, s mogućnošću kontrole na daljinu.

Vakuumska komora je opremljena s dva tipa poklopca. Jedan služi za plinovitu metu pod visokim tlakom (helij), dok se drugi koristi kod tekuće kriogene mete (vodik i deuterij).

Sustav kriogene tekuće mete sastoji se od dva rashladna kruga. Najbitniji dio u vanjskom krugu je Philipsov kompresor koji služi za ukapljivanje vodika. Ukapljeni vodik se pomoću transfer cijevi dovodi do vakuumske komore gdje hladi izmjenjivač topline. Ugrijani plin vodika vraća se natrag u Philipsov kompresor. Izmjenjivač topline spojen je na unutarnji krug (tzv. Basel krug), slika 3.2, koji sadrži ukapljen plin - metu. Snop elektrona gađa cilindar dijametra 2 cm, čije stjenke su napravljene od 50 µm debele havarske folije. Tekuća kriogena meta nalazi se u pothlađenom stanju i neprestano se recirkulira pomoću ventilatora kako bi se spriječilo lokalno pregrijavanje od strane snopa i formiranje mjehurića plina u cilindru. Kod većih iznosa struje snopa, lokalno pregrijavanje sprječava se tako da se snop dodatno rasterizira u transverzalnim smjerovima frekvencijom od nekoliko kHz i amplitudom od nekoliko mm. Temperatura i tlak u unutarnjem krugu se neprestano prate i bilježe, kako bi se u svakom trenutku moglo odrediti gustoću tekuće mete. U ovom eksperimentu meta je bila tekući vodik.

8.2.3 Tri standardna spektrometra

Glavni eksperimentalni postav A1 kolaboracije, sastoji se od tri magnetska spektrometra visoke rezolucije, a poznati su kao A (crveni), B (plavi) i C (zeleni), vidi sliku 3.3. Spektrometri mogu mjeriti nezavisno jedan o drugom, a mogu i raditi u dvostrukoj ili trostrukoj koincidenciji. Sva tri spektrometra mogu se rotirati oko središta u kojem je vakuumska komora s metama.

Magneti spektrometara A i C raspoređeni su u kvadrupol-sekstupol-dipol-dipol konfiguraciju. Kvadrupol fokusira čestice u nedisperzivnom smjeru i time povećava akceptanciju kuta raspršenja, te istovremeno defokusira čestice u disperzivnom smjeru, pa time povećava intrinzičnu razlučivost količine gibanja. Uloga sekstupolnog

magneta je da ispravi magnetooptičke greške drugog reda, odnosno tzv. sfernu aberaciju. Dva dipolna magneta zakreću putanje čestica prema detektorskom sustavu. Ovaj raspored magneta omogućava visoku rezoluciju u mjerenju kuta i količine gibanja čestica na relativno velikoj akceptanciji (28 msr). Spektrometar C je umanjena verzija spektrometra A za faktor 11/14.

Spektrometar B ima samo jedan dipolni magnet, koji podsjeća na poluotvorenu morsku školjku. Zbog toga je spektrometar B mnogo uži u odnosu na A i C, te može dohvatiti i čestice koje se raspršuju pod kutom od 7°. Nagib polova magneta stvara nehomogeno magnetsko polje s dvostrukim fokusom, što omogućava fokusiranje u disperzivnom i nedisperzivnom smjeru [34]. Navedeno ima za posljedicu da je prostorna rezolucija spektrometra B bolja, ali je akceptancija manja (5.6 msr). Ovaj spektrometar je također moguće nagnuti do 10° za mjerenja izvan ravnine.

Glavne karakteristike spektrometara sažete su u tablici 3.1, a presjeci kroz spektrometre A i B nalaze se na slici 3.4. Centralna magnetska polja spektrometara, a samim time i centralna količina gibanja, određena su i kontroliraju se putem Hallovih i NMR proba. Hallove probe služe za grubo mjerenje magnetskog polja, dok NMR probe vrlo precizno mjere magnetsko polje, te služe za fina podešavanja centralne količine gibanja.

8.2.3.1 Detektorski sustavi

Detektorski sustavi sva tri spektrometara su vrlo slični. Sastoje se od četiri vertikalne driftne komore (VDC), dva sloja scintilatora (dE i ToF) i plinskog Čerenkovog detektora, slika 3.5. VDC-i služe za rekonstrukciju putanje čestice, scintilatori daju vremenski signal, a obje ravnine zajedno omogućuju razlikovanje protona od lakših čestica (nabijenih piona, elektrona i pozitrona) na temelju mjerenja energije deponirane u pojedinom sloju. Slojevi scintilatora nisu prikladni za razlikovanje između elektrona/pozitrona i nabijenih piona - za to služi Čerenkov detektor. Dodatno se kod spektrometra A plinski Čerenkov detektor može zamijeniti s protonskim polarimetrom.

8.2.3.2 Elektronika i sustav za prikupljanje podataka

Svi spektrometri opremljeni su s nezavisnom elektronikom. Svrha te elektronike je pojačavanje signala iz detektora i analogno-digitalna konverzija istih, ali i generiranje signala (okidača) za početak prikupljanja podataka. Minimalni uvjeti da bi se generirao signal okidač je ispunjen, ako događaj u scintilatoru proizvede signal koji je veći od zadanog praga. Ovaj minimalni uvjet može se proširiti tako da se traži prisutnost signala u: dE i ToF sloju (uvjet koincidencije), dE ili ToF sloju, samo u dE sloju,

samo u ToF sloju. Također se može zahtijevati i koincidencija ili anti-koincidencija sa Čerenkovljevim detektorom. Željeni uvjeti se mogu odabrati i za vrijeme mjerenja pomoću jedinice s programabilnom logikom (PLU) [34]. PLU signali iz A, B i C spektrometara šalju se u univerzalni logički modul (ULM) koji je opremljen s FPGA-om (od engl. Field Programmable Gate Array). Moguće je promijeniti širinu dolaznih signala, zakasniti ih i skalirati njihovu učestalost na niže, ovisno o kinematičkoj konfiguraciji i mjerenoj fizikalnoj reakciji. Tijekom mjerenja FPGA se može namjestiti na sljedeće logičke uvjete: svi događaji u A, svi događaji u B, svi događaji u C, koincidencija AB, koincidencija BC, koincidencija ABC [38].

8.3 Spektrometar kratke orbite - SOS

SOS je spektrometar specijaliziran za detekciju, te precizno mjerenje energije i količine gibanja niskoenergijskih piona, slika 4.1 i 4.3. To omogućavaju njegove male dimenzije u odnosu na spektrometre A, B i C, što rezultira duljinom centralne putanje čestica od otprilike 1.6 m (misli se na udaljenost od mete do detektorskog sustava u SOS-u). Za danu vrijednost količine gibanja, udio piona koji se ne raspadnu u SOS-u biti će mnogo veći nego u slučaju tri standardna spektrometra A, B i C. Nadalje, smanjivanjem kinetičke energije piona povećava se vjerojatnost višestrukog raspršenja. Stoga je SOS-ov sustav za određivanje putanje čestica izveden s dvije driftne komore volumnog tipa (slika 4.4) koje rade s plinskom mješavinom 50% helija i 50% etana [15, 16]. Ovakvim izborom tipa driftnih komora i radnog plina smanjena je efektivna debljina SOS-ovog sustava za određivanje putanje čestica u odnosu na velike spektrometre, a samim time smanjena je i vjerojatnost višestrukog raspršenja niskoenergijskih piona.

Detektorski paket SOS-a sastoji se još i od pet slojeva plastičnih scintilatora debljina 3, 10, 20, 20 i 10 mm [12, 14], slika 4.6. Svaki sloj scintilatora daje vremensku i energijsku informaciju o čestici koja je prošla kroz njega. Vremenske informacije moguće je staviti u različite logičke odnose, kako među scintilatorima tako i s ostalim spektrometrima. Energijske informacije iz pojedinih scintilatora mogu se na različite načine kombinirati u konfiguraciju dE-E teleskopa i na taj način moguće razlikovati pione od pozitrona i protona.

SOS ima jedan dipolni magnet (slika 4.2) Browne-Buechner tipa [39]. Između kružnih polova radijusa 350 mm formira se homogeno magnetsko polje, koje ovisno o naboju čestice zakreće putanju normale za $\pm 90°$. Ostale karakteristike SOS mogu se vidjeti u tablici 3.1.

8.4 Analiza podataka

Analizu podataka možemo opisati kao postupak u kojem koristimo sirove podatke iz različitih detektora kako bi identificirali čestice koje su nastale u relevantnoj reakciji i da rekonstruiramo njihove fizikalne veličine kao što su kut, energija i količina gibanja. Kombinacijom podataka iz različitih spektrometra, moguće je izvesti dodatne veličine (npr. nedostajuća masa), koje mogu poslužiti za dodatnu redukciju pozadinskih događaja.

8.4.1 Udarni presjek $p(e, e'\pi^+)n$ reakcije

Kako bi odredili udarni presjek $p(e, e'\pi^+)n$ reakcije, prvo iz svih događaja koje su detektori spektrometara registrirali trebamo izdvojiti one događaje koji pripadaju upravo ovoj reakciji. Takve "stvarne" događaje trebamo normalizirati s luminoznošću L (korigiranom za mrtvo vrijeme) i faznim prostorom Φ kojeg pokrivaju spektrometri, te ih korigirati s obzirom na raspad piona K_{decay}, mionsku kontaminaciju K_{muon} i ukupnu efikasnost ϵ_{total}, vidi jednadžbu 6.1.

8.4.2 Luminoznost

Integrirana luminoznost je definirana kao umnožak površinske gustoće jezgara mete N_T i broja elektrona N_e koji udaraju u metu u vremenu T. U sklopu programskog paketa "Cola" [42], nalazi se program Lumi++ koji pomoću izmjerene jakosti struje snopa, mrtvog vremena, materijala i gustoće mete računa integriranu luminoznost.

8.4.3 Fazni prostor

Fazni prostor reakcije definiran je s geometrijskom akceptancijom spektrometara i s različitim eksperimentalnim uvjetima pod kojima je dana reakcija mjerena. Ne može se izračunati analitički, nego se mora odrediti pomoću Monte Carlo simulacije specijaliziranim programom Simul++ [42]. U simulaciji faznog prostora produkti izabrane reakcije generiraju se izotropno u prostornom kutu u zadanom intervalu prijenosa četveroimpulsa i kuta (u sustavu centra mase) za danu kinematiku. Zadani intervali su obično veći od nominalnih akceptancija spektrometara, kako bi se osiguralo dobro ponašanje simuliranih podataka na rubovima. Kod simulacije koincidencijskog eksperimenta, svaka čestica iz određenog para mora proći kroz kolimator svojeg spektrometra, a količina gibanja pojedinne čestice mora biti unutar intervala kojeg njihov

spektrometar prihvaća. Ako je to sve zadovoljeno događaj se prihvaća, pa se može odrediti i pripadna nedostajuća masa.

8.4.4 Koincidencijsko vrijeme

Razlika između vremena proleta čestica u jednom i u drugom spektrometru može se koristiti za separaciju stvarnih koincidencijskih događaja od slučajnih. Vremenska razlika mjeri se pomoću koincidencijskog TDC-a (od engl. Time-to-Digital Converter). Događaj u ToF scintilatorskoj ravnini spektrometra A definira start signal, dok događaj u drugom po redu scintilatoru SOS-a daje stop signal TDC jedinici. U principu, razlika vremena proleta trebala bi imati konstantni iznos ako se radi o elektronu i pionu koji pripadaju istoj $p(e, e'\pi^+)n$ reakciji. Za sve ostale nekorelirane događaje, vrijednosti razlike vremena proleta trebale bi biti jednoliko raspodijeljene unutar širine vremenskih vrata TDC-a. Korigirani vremenski spektar iz koincidencijskog TDC-a vidi se na slici 6.3 (kanali TDC-a su preračunati u nanosekunde). Tu se jasno raspoznaju uniformno raspodijeljena pozadina slučajnih događaja, te jedan koincidencijski vrh koji odgovara raspršenom elektronu i produciranom pozitivnom pionu iz $p(e, e'\pi^+)n$ reakcije.

8.4.5 Nedostajuća masa

Drugi način za identifikaciju stvarnih koincidencija je tzv. spektar nedostajuće mase. U reakciji $p(e, e'\pi^+)n$ mjerimo četveroimpuls raspršenog elektrona e' i produciranog nabijenog piona π^+, međutim četveroimpuls nastalog neutrona n ne mjerimo. Naziv "nedostajući" odnosi se na observable čestice koju ne detektiramo. Pomoću zakona očuvanja energije i količine gibanja možemo izračunati masu nedostajuće čestice m_{miss}. Dakle, ako smo zaista detektirali elektron u spektrometru A i pion u SOS-u onda izračunata nedostajuća masa m_{miss} mora biti jednaka masi neutrona.

Ako izračunamo nedostajuću masu za sve koincidencijske događaje (stvarne + slučajne koincidencije) dobivamo spektar nedostajućih masa. Iz praktičnih razloga od svake izračunate nedostajuće mase oduzeta je masa neutrona, tako da vrh koji odgovara masi neutrona bude centriran oko nule. Na slici 6.4 nalazi se spektar nedostajuće mase kinematike axialFF_591 bez ikakvih rezova. Vidimo da je omjer signala (vrha) i pozadine (slučajnih koincidencija) otprilike 13 : 4.

Sada napravimo rez na koincidencijski vrh, slika 6.5. Kako vidimo, pozadina ispod vrha nedostajuće mase otprilike se je smanjila za faktor 10 (slika 6.6) u odnosu na situaciju bez tog reza. Cilj daljnje analize je redukcija preostale pozadine (slučajnih koincidencija) tako da postavljamo odgovarajuće rezove na različite observable. Pri

tome je važno da ti rezovi ne uklanjaju stvarne koincidencije.

Međutim, treba imati na umu da postoje slučajne koincidencije koje zadovoljavaju sve rezove, a kombinacija njihovih observabli daje nedostajuću masu koja se nalazi ispod vrha stvarnih događaja. Takvu pozadinu jedino je moguće ukloniti oduzimanjem. Broj slučajnih događaja ispod vrha nedostajuće mase moguće je odrediti rezom na uniformni dio vremenskog histograma 6.5. Događaji koji su izolirani ovim rezom sigurno ne sadrže stvarne događaje, ali svejedno moraju zadovoljavati i sve ostale rezove. Rezultirajući histogram nedostajuće mase onda predstavlja raspodjelu slučajnih događaja ispod vrha stvarnih događaja 6.7. Na kraju histogram nedostajuće mase pozadine treba normalizirati s obzirom na širinu koincidencijskog vremenskog reza i širinu reza na uniformni dio vremenske raspodjele, te ga oduzeti od koincidencijskog histograma nedostajuće mase. Rezultati ovog postupka vide se za odabrane kinematike na slikama 6.8 i 6.9.

Na tim histogramima vidimo da vrh nedostajuće mase ima brzorastući lijevi rub i sporopadajući desni rub koji nastaje zbog radijativnih gubitaka nabijenih čestice. Naime, u blizini protona mete elektron može emitirati realni ili virtualni foton (unutarnje zakočno zračenje ili Schwingerovo zračenje). Kod $p(e,e'\pi^+)n$ reakcije to je dominantni proces radijativnih gubitaka. Tzv. vanjsko zakočno zračenje uključuje sve procese u kojima nabijene čestice emitiraju foton prije ili nakon reakcije u polju drugih jezgara. Kako fotone zakočnog zračenja ne mjerimo, nije moguće korigirati radijativne gubitke individualnih događaja. Stoga je u kompjuterskim simulacijama potrebno modelirati radijativne procese kako bi dobili dobro slaganje s eksperimentom. Modeli za najvažnije radijativne procese opisani su u [10] dodatak D.

Iako čestice većinu svog puta od mete do detektorskih paketa u spektrometrima prolaze kroz vakuum, ipak mali dio puta prolaze i kroz različite materijale (sama meta, različite folije, zrak i sl.) u kojima gube energiju. Ako taj gubitak energije ne bi korigirali vrh nedostajuće mase bio bi pomaknut prema pozitivnim vrijednostima, te ne bi bio centriran oko nule. Sve korekcije gubitka energije rade se pomoću kompjuterskog programa i većina se odvija automatski, osim korekcije zbog snijega na stijenkama kriogene mete. Naime, iako se komora s metama nalazi pod visokim vakuumom, u komori će ipak ostati neka mala količina rezidualnih atmosferskih plinova. Stjenke kriogene mete nalaze se na temperaturi tekućeg vodika, pa će se na njima formirati snijeg od rezidualnih plinova. Debljina snijega može se promijeniti tijekom vremena, pa se to treba ručno korigirati.

8.4.6 Korekcijski parametri

Korekcijski parametri opisuju različite eksperimentalne okolnosti koji mogu iskriviti rezultate samog mjerenja. Od ovih okolnosti neke se mijenjaju tijekom vremena, neke ovise o kinematici, a neke ostaju konstantne tijekom vremena.

a) **Gustoća tekuće mete** - ovisi o tlaku i o temperaturi u unutarnjem rashladnom krugu. Zbog toga se ove veličine mjere tijekom vremena trajanja eksperimenta. Najveće promjene tih veličina događaju se nakon što struju snopa uključimo ili isključimo, slika 6.10. Promjene su manje ako za vrijeme uključenog snopa promijenimo jakost struje. U analizi, svaki put kada se temperatura promijeni više od 0.03 K, a tlak više od 2 mbar, izračuna se novi iznos gustoće mete pomoću programa "liquidDensity" koji računa gustoću tekućeg vodika prema [43]. Manje fluktuacije temperature i tlaka se uprosječuju.

b) **Snijeg na meti** - nastaje smrzavanjem rezidualnih atmosferskih plinova na hladnoj ($\sim$ 22 K) površini mete. Sam snop elektron, u točki u kojoj udara u metu, još može otopiti snijeg, ali s bočnih strana mete tok raspršenih i nastalih čestica nije dovoljan da bi se snijeg otopio. U sloju snijega čestice gube energiju i pripadni vrh nedostajuće mase pomaknut je prema pozitivnim vrijednostima u odnosu na nulu. U analizi, debljinu snijega je moguće ručno dodavati ili oduzimati. Odabire se ona vrijednost debljine snijega za koju je vrh nedostajuće mase centriran oko nule, a oblici raspodjela nedostajućih masa mjerenja i faznog prostora se najbolje podudaraju.

c) **Položaj mete** - tijekom hlađenja mete može se dogoditi da se zbog termičkog naprezanja materijala meta malo pomakne i to nije moguće korigirati. Ali se može dogoditi i da se položaj mete ne poklapa sa centrom rotacije spektrometara oko mete, a to se može korigirati mijenjanjem određenih parametara prilikom analize.

d) **Rezolucija spektrometara** - tj. rezolucije količine gibanja i disperzivnog kuta mijenjaju se ovisno o kinematici. Njihove vrijednosti jedne su od ulaznih parametara simulacije faznog prostora. Ukoliko aktualne vrijednosti tih rezolucija nisu poznate, koriste se oni parametri kod kojih simulirani vrh nedostajuće mase najbolje odgovara obliku i širini eksperimentalnog vrha nedostajuće mase za danu kinematiku.

8.4.7 Ukupna efikasnost

Ukupna efikasnost je umnožak nekoliko individualnih efikasnosti. Na najvišoj razini je efikasnost koincidencije. To je vjerojatnost da dva korelirana događaja budu prepoznata kao takva. Možemo reći da je to mjera sposobnosti programa za pohranu događaja da sinkronizira i spoji podatke iz dva spektrometra u jedinstveni tok podataka. Efikasnost koincidencije iznosi 0.996 [8].

Na razini spektrometra, ukupna efikasnost je umnožak efikasnosti pojedinih detektora. Za ovaj eksperiment, kod spektrometra A, najvažnije su bile efikasnost ToF scintilatorskog sloja i efikasnost VDC-ova. Kako su scintilatorske ravnine segmentirane, na spojevima segmenata može doći do gubitka čestica, pa je efikasnost scintilatorskih ravnina malo manja od 100%. Kod ToF sloja ona je u ovom eksperimentu iznosila $98.04 \pm 0.03\%$. Za efikasnost VDC-ova opravdano da se uzme da iznosi 100%. Naime svaki sloj VDC-a sadrži velik broj signalnih žica koje i same imaju veliku efikasnost. Npr. za x1-ravninu, usrednjena efikasnost po žici iznosila oko 99.26%, slika 6.13. Slojevi VDC-ova (x1, x2, s1, s2) ne rade kao individualni detektori nego rade u parovima (x1 i x2, s1 i s2). Za uspješnu rekonstrukciju putanje čestica u određenoj koordinati (disperzivna ili nedisperzivna) potrebna je informacija iz minimalno tri signalne žice odgovarajućeg VDC para. Čak i u slučaju pokvarene ili neefikasne žice, velika je vjerojatnost (prosječno 99.26%) da će susjedna žica dati potrebnu informaciju.

Efikasnost scintilatora u SOS istražena je u sklopu [12]. U analizi ovog eksperimenta koriste se samo informacije iz drugog i trećeg scintilatora po redu. Za razliku od velikih spektrometara, ti scintilatori nisu segmentirani, stoga je i za očekivati da je njihova efikasnost veća. Prilikom analize bilo je moguće provjeriti samo efikasnost trećeg scintilatora. Provjera je izvedena tako da se analiza jednom provede s informacijama iz trećeg scintilatora, a zatim bez tih informacija. Dobiveno je da se u ta dva slučaja udarni presjeci razlikuju za svega 0.1%, što znači da efikasnost trećeg scintilatora iznosi 99.9%. Kako je taj efekt jako mali (oko 10 puta manji od statističke greške), aproksimativno je uzeto da je efikasnosti trećeg scintilatora jednaka 100%. Drugi scintilator je davao signal okidač, pa njegovu efikasnost nije bilo moguće provjeriti. No kako su oba scintilatora napravljena od istog materijala i imaju istu geometriju, pretpostavljeno je da i drugi scintilator ima efikasnost 100%. Driftne komore u SOS-u nemaju stopostotnu efikasnost kao VDC-ovi. SOS-ove driftne komore (X i Y) imaju driftne ćelije koje se sastoje od osam signalnih žica. Signalne žice su poredane vertikalno, a njihov položaj alternira lijevo-desno za 100 μm u odnosu na sredinu ćelije, slika 4.5. Takav raspored žica omogućava programu za rekonstrukciju putanje da odredi da li je čestica prošla s lijeve ili s desne strane pojedine žice. Nadalje, usrednjena efikasnost po žicama iznosila je oko 89.89% za X-komoru i 97.26% za Y-komoru. Kod SOS-a, pro-

gram za rekonstrukciju putanje zahtjeva da minimalno četiri žice proizvedu signal u danoj komori, pa će u slučaju X-komore efikasnost biti nešto slabija. Također, isti tok čestica prolazi u X-komori kroz osam driftnih ćelija, dok u Y-komori prolazi kroz samo dvije driftne ćelije. Zbog toga je mrtvo vrijeme Y-komore veće od X-komore, a to negativno utječe na efikasnost Y-komore. Kako tok čestica kroz komore ovisi o kinematici i struji snopa, efikasnosti SOS-vih driftnih komora određene su za svaku kinematiku posebno, vidi tablicu 6.4.

8.4.8 Korekcija zbog raspada piona

Pozitivni pion je nestabilna čestica s vremenom života $\tau = 26.033$ ns [13]. Zbog toga će broj piona koji prežive do detektora N_π^{det} biti manji od broja piona koji je produciran u meti N_π^{tg}. Korekcija zbog raspada pion K_{decay} jednaka je omjeru N_π^{tg} i N_π^{det}. Prema 6.9 i 6.10 možemo izračunati K_{decay}. Za to je potrebno znati duljinu putanje čestice s i količina gibanja čestice p_π. Zadnja veličina nije problem, jer količinu gibanja mjerimo. Međutim, duljina putanje s ne može se mjeriti direktno, već je za potrebe analize podataka ovog eksperimenta, napravljena procedura koja iz direktno mjerenih (koordinate driftnih komora) i izvedenih observabli (koordinate mete) računa tu duljinu. Na taj način za svaku česticu detektiranu u SOS-u možemo izračunati pripadni korekcijski faktor raspada, čiju raspodjelu za kinematiku axialFF_591 vidimo na slici 6.17.

U starijim eksperimentima broj detektiranih piona u nekoj kinematici korigiran je zbog raspada piona s jednim usrednjenim korekcijskim faktorom. U ovoj smo analizi, korekciji zbog raspada piona pristupili na dva načina. Kod prvog načina puna širina akceptancije količine gibanja SOS-a (od -13% do $+16\%$) podijeljena je na 1 MeV/c široke intervale, ukupno 29. U svakom intervalu definirana su sljedeća tri histograma: histogram nedostajuće mase s rezom na koincidencijski vrh i pripadni K_{decay} histogram (plus svi ostali rezovi), te histogram nedostajuće mase s rezom na uniformnu vremensku pozadinu. U svakom intervalu izračuna se usrednjeni K_{decay}, a od histograma nedostajuće mase oduzme se odgovarajuća pozadina. Broj događaja u preostalom histogramu nedostajuće mase korigira se s usrednjenim K_{decay}. Na kraju trebamo još zbrojiti doprinose po svim intervalima i taj zbroj onda predstavlja broj stvarnih događaja. U drugom pristupu ideja je da se raspodjela duljina putanje podijeli na intervale široke 10 mm, a zatim se dalje slijedi ista procedura koja je opisana malo prije.

8.4.9 Mionska kontaminacija

Sama korekcija zbog raspada piona je ispravna ukoliko u podacima nemamo mionske kontaminacije. No kako uvijek postoje mioni koje ćemo krivo identificirati kao pione,

naši podaci sadržavati će neki udio mionske kontaminacije. Ako bi kontaminirane podatke korigirali za raspad piona, još bi više iskrivili konačni rezultat, jer bi ti podaci bili prekorigirani. Stoga je važno da za svaku kinematiku odredimo udio mionske kontaminacije.

U sklopu svojeg diplomskog rada [46], Miha Mihovilovič je proširio mogućnost programa Simul++ da u spektrometrima A i B može pratiti česticu od mete do detektorskog paketa u spektrometru i na tom putu simulirati raspad nestabilne čestice. Za potrebe analize podataka ovog eksperimenta programu Simul++ dodana je mogućnost da simulira raspad nestabilne čestice (piona) i u SOS-u. Sam SOS je u simulaciji izveden vrlo jednostavno. Simulira se samo homogeno dipolno polje SOS-ovog magneta, rubna polja na završecima polova nisu uzeta u obzir. Isto tako, u obzir nije uzeto raspršenje čestica od unutarnjih zidova SOS-a. Simulacija prati pion na putu od mete, kroz kolimator i dipolni magnet SOS-a, pa sve do posljednjeg scintilatora. Ako se pion raspadne na tom putu, dalje se prati mion. Iz observabli simuliranih elektrona i piona, odnosno miona i elektrona moguće je izračunati pripadne nedostajuće mase. Raspodjele "pionske", odnosno "mionske" nedostajuće mase prikazane su na slici 6.19. Te dvije raspodjele se djelomično preklapaju. Lijevi rub pionske raspodjele završava na $-3\,\mathrm{MeV/c^2}$, dok se lijevi rub mionske raspodjele nastavlja dalje prema negativnim vrijednostima. Dakle, rezom na nedostajuću masu moguće je odstraniti dio miona, a ostatak kojeg nije moguće odstraniti nikakvim rezom može se izračunati iz rezultata simulacije.

U tablici 6.5 prikazani su udjeli mionske kontaminacije u intervalu nedostajuće mase od -3 do $11\,\mathrm{MeV/c^2}$ za sve kinematike. Ako pogledamo kinematiku axialFF_591 ispada da je srednji korekcijski faktor zbog raspada piona 1.333, slika 6.17, što znači da se oko 25% piona raspadne u mion i mionski neutrino. Prema rezultatima u tablici 6.5, otprilike 30% tih miona, u intervalu od -3 do $11\,\mathrm{MeV/c^2}$, biti će krivo identificirani kao pioni. Ostali mioni (oko 70% njih) ili neće biti u tom intervalu nedostajuće mase, ili će njihove putanje promašiti detektorski paket i neće biti detektirani.

8.4.10 Rezovi

Opća uloga rezova na različitim observablama je smanjenje pozadine, bez gubitaka stvarnih događaja. Neki rezovi su univerzalni, dok neki ovise o danoj kinematici. Jedini rezovi, kod kojih je mali gubitak stvarnih događaja dopušten, su rezovi na akceptancije spektrometara. Zato jer rez na akceptanciju ne odstranjuje samo stvarne događaje, nego i odgovarajući dio faznog prostora koji daje simulacija. Za ostale rezove, kada se stavi rez na neku varijablu, gleda se također i histogram nedostajuće mase događaja koje taj rez isključuje. Ukoliko se u takvom histogramu pojavi vrh na

mjestu mase neutrona, to znači da je rez preagresivan. Vrijednost reza moramo mijenjati dok u histogramu nedostajuće mase vrh ne nestane. Specijalni rez je rez na nedostajuću masu. On definira iznos veličina koje se koriste u računu udarnog presjeka.

Do sada smo već spomenuli vremenski rez na koincidencijski vrh i vremenski rez na slučajne koincidencije, slika 6.5. Kod spektrometra A imamo dva reza. Jedan rez odnosi se na interval količine gibanja raspršenog elektrona čije observable tvore vrh nedostajuće mase i taj rez ovisi o kinematici. Drugi rez odnosi se na Z-koordinatu rekonstruiranog verteksa u spektrometru A, slika 6.12. Naime, elektroni se mogu raspršiti na različitim plinovima i folijama, zbog čega će se njihova putanja promijeniti, a rekonstruirana količina gibanja neće odgovarati količini gibanja originalnoga elektrona. Sretna okolnost je, da obično i verteks takvih elektrona bude rekonstruiran izvan dimenzija mete. Rezom -50 mm $< Z_v < 50$ mm možemo smanjiti pozadinu koju stvaraju takvi elektroni. Kako spektrometar rekonstruira položaj verteksa s konačnom rezolucijom, interval je puno širi od same dimenzije mete.

Kod SOS-a imamo tri reza. Najkompliciraniji je rez na akceptanciju SOS-a, koja ima oblik trapezoida s odrezanim kutovima što se najbolje vidi na 2D histogramu δp_0 vs. θ_0 SOS-ovih koordinata mete, slika 6.21. Iako SOS ima kolimator u obliku trapeza, očito je da detektorski ustav na neki način odreže dio akceptancije, što je primijećeno i u simulaciji. Zbog kompliciranog oblika SOS-ove akceptancije, primijenili smo rezove u formi linearne funkcije $\theta_0 = a \cdot \delta p_0 + b$. Drugi rez odnosi se na koordinate SOS-ovih driftnih komora. Matthias Ding je još u svojem doktoratu [16] primijetio da ako čestica prođe vrlo blizu signalne žice, odluka je li prošla s lijeve ili s desne strane žice može ispasti krivo. Umjesto stvarne putanje rekonstruira se zrcalna putanja koja ima kut s pogrešnim predznakom. Ovaj efekt se najbolje vidi na 2D histogramu koordinata X-komore x_{ch} vs. θ_{ch}, lijeva slika 6.22. Vidimo da u centralnoj raspodjeli u obliku paralelograma nedostaju uske trake, koje su zrcaljene s obzirom na predznak kuta u područje gdje ne bi trebale biti. Korekcija ovog efekta izvedena je unutar programa za rekonstrukciju putanje "pdcD.cc" na način da su trake u zabranjenom području izolirane, a za te događaje odluka o predznaku kuta napravljena je namjerno. Nakon korekcije, desna slika 6.22, praznine u centralnoj raspodijeli su popunjene. Ova korekcija je vrlo bitna, jer se u histogram nedostajuće mase korigiranih događaja isto pojavljuje vrh na položaju mase neutrona, tj. i korigirani događaji sadrže stvarne koincidencije. Posljednji rezovi, vezani uz SOS, odnose se na energiju koju čestice deponiraju u SOS-ovim scintilatorima. Rezovi su postavljeni tako da odstranjuju minimalno ionizirajuće čestice iz podataka. Prihvaćaju se događaji koji u drugom scintilatoru deponiraju energiju veću od 260-tog ADC kanala i u trećem scintilatoru veću od 280-tog ADC kanala.

Rez na nedostajuću masu odnosi se na interval nedostajuće mase iz kojeg uzimamo događaje za računanje udarnog presjeka. Isti interval moramo koristiti i kod veličina

koje dobivamo iz simulacija, a to su fazni prostor i mionska kontaminacija. Zato je važno da se raspodjele vrhova simuliranih i eksperimentalnih nedostajućih masa poklapaju u obliku i položaju. Obično, na početku analize bez podešenih parametara, poklapanje postoji, ali nije zadovoljavajuće. Položaj i oblik eksperimentalnog vrha kontrolira se finim podešavanjem centralne količine gibanja spektrometra i debljinom snijega na meti. Kod simulacija širina i oblik vrha mijenja se podešavanjem kutne rezolucije i rezolucije količine gibanja za svaki spektrometar. Kako ordinate eksperimentalnog i simuliranog histograma nedostajuće mase nisu u istim jedinicama, te dvije raspodjele potrebno je na neki način normalizirati kako bi mogli uspoređivati njihove oblike. Za normalizacijski faktor izabran je omjer najviših binova u obje raspodjele. Kod takvog pristupa najviši binovi u obje distribucije će se poklapati [12].

Na slici 6.24 primjer je rezultata prilagođavanja položaja i oblika vrhova za kinematiku axialFF_591. Što se tiče samog vrha poklapanje je više-manje u redu. Međutim, na uvećanoj slici vidimo da se radijativni repovi ne poklapaju najbolje. Isto tako s lijeve strane (prema negativnim vrijednostima) kod eksperimentalnog vrha još uvijek imamo neke događaje. Uzroci ovih efekata mogu biti razni. Ili je simulacija radijativnog repa nedovoljno precizna, ili postoji neka vrsta pozadine koju nismo odstranili oduzimanjem, a nismo ju uzeli u obzir kod simulacije. Kandidati za ovaj oblik pozadine su mioni. Ako sad usporedimo mionsku raspodjelu nedostajuće mase s eksperimentom, slika 6.25, vidimo da se lijevi rub mionske i eksperimentalne nedostajuće mase dobro poklapaju, a dok je desni (radijativni) rub eksperimentalne nedostajuće mase malo podignut zbog miona. Ako od eksperimentalne raspodjele nedostajuće mase oduzmemo mionsku raspodjelu, slaganje vrha faznog prostora i mjerenja će se poboljšati, slika 6.26. Poklapanje na lijevom rubu je mnogo bolje, čak je na nekim mjestima i prekorigirano. S desne strane vrha, poklapanje radijativnih repova također je puno bolje, male diskrepancije dolaze od male statistike u tom djelu raspodjele ili od postupka normalizacije simuliranih histograma. Da bi se u izračunu udarnog presjeka izbjegla potreba za normalizacijom, mionska kontaminacija se ne uklanja oduzimanjem histograma, nego se u danom intervalu izračuna udio miona i onda se za taj udio umanji broj eksperimentalnih događaja u tom intervalu.

8.4.11 Procjena sistematske greške

Ukupna sistematska greška ima nekoliko različitih doprinosa. Iznos svakog doprinosa procijenjen je posebno, a ukupna greška se onda dobiva kao drugi korijen zbroja kvadrata pojedini doprinosa, jednadžba 6.15.

Sistematskoj greški luminoznosti doprinose: nepouzdanost struje snopa $\Delta I = 0.3/n$ μA (n broj recirkulacija u trećem RTM-u), nepouzdanost gustoće mete $\Delta \rho$ (zbog fluk-

tuacija temperature i tlaka mete), nepouzdanost prosječne duljine mete $\Delta \bar{x}^{rel}$ (iznosi oko 0.5% [10]). Koristeći jednadžbu 6.11, odnosno jednadžbu 6.12 možemo izračunati sistematsku grešku luminoznosti.

Kod korekcije zbog raspada piona sistematska greška ovisi o nepouzdanosti količine gibanja piona Δp_π (u [16] određeno je da iznos oko 1.3 MeV/c) i nepouzdanosti u izračunu duljine putanje piona Δs za koju je uzeta procjena od 2 cm. Izabrana je ovako velika vrijednost jer neke dimenzije u detektorskom paketu nisu poznate sa željenom preciznošću, a uz to kod Y-komore SOS-a korekcija za odluku lijevo-desno nije implementirana jer trake koje sadrže događaje nisu bile jasno odvojene od centralne distribucije, slika 6.29. Sam iznos sistematske greške možemo događaj po događaj izračunati u apsolutnom (jednadžba 6.13) ili relativnom iznosu (jednadžba 6.14). Na slici 6.30 prikazana je raspodjela relativne sistematske greške zbog raspada piona za axialFF_897a kinematiku. Za račun ukupne sistematske greške uzima se maksimalna vrijednost koja iznosi otprilike 0.54%.

Sistematska greška mionske kontaminacije određena je pomoću statističke fluktuacije rezultata. Vrijednost kontaminacije izračuna se iz rezultata simulacije 10^8 događaja i promatra se kako se vrijednost mionske kontaminacije mijenja u simulaciji s $1.1 \cdot 10^8$, odnosno $0.9 \cdot 10^8$ događaja. Za sve kinematike dobivena je relativna greška od 0.23%. Na isti je način procijenjena i sistematska greška faznog prostora od 0.12%.

Korekcijom na odluku lijevo-desno kod X-komore SOS-a spašeno je oko 2.04% stvarnih koincidencija. Sama korekcija obuhvaća samo tri driftne ćelije zdesna, a za ostale ćelije nije bilo moguće implementirati korekciju, slika 6.22. Ili tog efekta na lijevoj strani nema, ili je toliko mali da ga je teško uočiti, a i sami krivo rekonstruirani događaji bili bi unutar središnje 2D raspodjele. Ovdje smo za procijenjenu grešku uzeli jednu trećinu od ukupno spašenih događaja, dakle 0.68%.

U slučaju korekcije zbog snijega na meti, sistematska greška procijenjena je na temelju ponovljene analize s -0.2 mm i $+0.2$ mm u odnosu na optimalnu vrijednost debljine snijega, a dobiveno je da iznosi 0.09%.

Najveći doprinos sistematskoj grešci dolazi od reza na nedostajuću masu (ovdje se misli na desni kraj intervala u radijativnom repu raspodjele). Ako smo dobro odradili kompletnu analizu konačni udarni presjek ne bi trebao ovisiti o položaju reza u radijativnom repu raspodjele nedostajuće mase. Kao što je ranije primijećeno u [11] i [12], ali i kod ovog eksperimenta, ako povećavamo desni rub reza iznos udarnog presjeka lagano raste, slika 6.31. Na pitanje što uzrokuje ovu pojavu nema jednoznačnog odgovora. Jedno od mogućih objašnjenja je svakako nesavršeno poklapanje radijativnih repova raspodjela mjerenja i simuliranog faznog prostora, zbog sve lošije i lošije statistike u radijativnom repu eksperimentalnih podataka. Za Rosenbluthovu separaciju i

određivanje TL interferencijskog člana korišteni su udarni presjeci kod kojih je gornja granica reza bila je na 11 MeV/c^2. Uz to su određeni i udarni presjeci s gornjom granicom reza na 6 MeV/c^2 i na 16 MeV/c^2. Pripadna standardna devijacija korištena je za procjenu sistematske greške. Ovisno o kinematici relativna sistematska greška reza na nedostajuću masu iznosi između 2.4% i 3.2%.

8.4.12 Elastični udarni presjek

Na kraju mjerenja prve tri kinematike iz tablice 5.1, sa spektrometrom A izmjeren je i udarni presjek elastičnog raspršenja elektrona na protonu $p(e, e')$ za kinematike koje su sažete u tablici 5.2. Elastični udarni presjek elektrona na protonu vrlo dobro je poznat i eksperimentalno i teorijski, pa su ova mjerenja napravljena sa ciljem da se prati stanje spektrometra A kroz vrijeme trajanja eksperimenta.

U ovom slučaju vrh nedostajuće mase odgovara masi protona. Luminoznost možemo izračunati pomoću programa Lumi++, a fazni prostor Φ pomoću Simul++. Od ranije znamo efikasnosti detektora spektrometra A, pa elastični udarni presjek možemo izračunati pomoću jednadžbe 6.16. Teorijski udarni presjek dan je jednadžbom 2.32, a za vrijednosti električnog i magnetskog form-faktora korištena je spline parametrizacija iz [36]. Na slici 6.32 nalaze se teorijski (crvena linija) i eksperimentalni (plave točke) rezultati elastičnog udarnog presjeka u ovisnosti o kutu raspršenja elektrona θ_e. Greške po binovima određene su samo iz statističkih grešaka podataka i faznog prostora. Rubni binovi s obje strane raspodjela odgovaraju rubovima akceptancije spektrometra. Kako je tamo statistika događaje mala, pripadna greška će biti velika.

Za najveću energiju struje snopa od 855 MeV imamo odlično slaganje teorije i eksperimenta, a kako struja snopa pada (450 i 345 MeV) dolazi do male diskrepancije. Naime, zbog konačne učestalosti događaja koju detektorski paket spektrometra A može podnijeti, prilikom mjerenje elastičnog raspršenja mora se koristiti relativno mala struja snopa (oko 1 μA). To povećava grešku mjerenja struje snopa s Förster-ovom probom, koja se pogoršava kako smanjujemo energiju snopa, a samim time i broj recirkulacija u trećem RTM-u MAMI akceleratora. No sve u svemu, možemo zaključiti da je spektrometar A dobro funkcionirao tijekom cijelog trajanja eksperimenta.

8.5 Rezultati

Koristeći sve navedene korekcijske metode i rezove, za svih pet kinematika određen je udarni presjek reakcije $p(e, e'\pi^+)n$, koja je mjerena na invarijantnoj masi od 1094 MeV i prijenosu četveroimpulsa od 0.078 (GeV/c)^2. Rezultati su prikazani zajedno s

ukupnom greškom, te izdvojenom statističkom i sistematskom greškom, u tablici 7.2.

Kao što smo i očekivali, ovisnost tri udarna presjeka, mjerenih u paralelnoj kinematici, o polarizaciji virtualnog fotona ϵ je linearna, slika 7.1. Iz te ovisnosti Rosenbluthovom metodom separirani su L i T članovi udarnog presjeka, tablica 7.3. Ako ne uzmemo u obzir greške (ukupne ili sistematske ili statističke), linearna regresija za L član daje relativnu grešku od 6.3%, a za T član 3.4%. No ukupne greške tih članova su relativno velike, jer sadrže još i doprinose od statističke i sistematske greške, tablica 7.3.

Modeli, koji će biti prezentirani u daljnjem tekstu, faktoriziraju ukupni udarni presjek malo drugačije nego što je navedeno u jednadžbama 1.1 i 2.19. U definiciji faktorizacije modeli ne koriste longitudinalnu polarizaciju virtualnog fotona $\epsilon_L^\star$ [47]! Stoga je TL član udarnog presjeka (tablica 7.3) izračunat pomoću jednadžbe 7.1.

8.5.1 Usporedba teorijskih i eksperimentalnih rezultata

Rezultati L, T i TL članova udarnog presjeka uspoređeni su s predviđanjima teorijskih modela, kojima je moguće pristupiti putem mrežnog sučelja [47].

Prvi model je Dubna-Mainz-Taipei model ili jednostavnije DMT2001. Izračuni se provode unutar dinamičkog modela izmjene mezona, koji opisuje većinu postojećih podataka elektromagnetske produkcije piona sve do drugog rezonantnog područja. Model koristi potencijale koji su izvedeni iz efektivnog kiralnog lagranžijana [48]. Više detalja o modelu može se naći u [48–50].

Drugi model je baziran na analizi parcijalnih valova pomoću unitarnog izobarnog modela MAID. Model je konstruiran od nerezonantne pozadine i nukleonskih rezonanci. Prva verzija modela napravljena je 1998 godine, a od onda je model poboljšavan nekoliko puta. Aktualna verzija, MAID2007 [51], koristi svih 13 rezonanci na energijama do 2 GeV, s transverzalnim električni, transverzalnim magnetskim i Coulombskim vezanjima. Rezonance su opisane pomoću aproksimativno unitariziranih Breit-Wigner forma. Nerezonantna pozadina opisana je potencijalom elektroprodukcije piona koji sadrži doprinose Born-ovih članova opisanih s energijsko ovisnim miješanjem pseudoskalarnih i pseudovektorskih πNN vezanja i izmjenom vektorskih mezona u t-kanalu. Q^2 ovisnost pozadine nukleonskih polova s- i u-kanala opisana je form-faktorima iz [52]. Kod elektromagnetskog verteksa pionskog pola koristi se monopolni oblik pionskog form-faktora, na verteksu kontaktnog člana dipolni oblik za aksijalni form-faktor i na kraju standardni dipolni form-faktor za izmjenu vektorskih mezona. Pozadina se unitarizira pomoću postupka K-matrice. Parametri su dobiveni i iz monoenergijskih i globalnih prilagodbi na svjetsku bazu podataka pionske foto- i elektro-

produkcije. Detaljniji opis ovog modela dan je u [51].

Treći model je tzv. kiralni MAID (χMAID) [53]. Radi se o računu pionske foto- i elektroprodukcije u Lorentz-invarijantnoj barionskoj kiralnoj perturbacijskoj teoriji do i uključujući red q^4. Niskoenergijske konstante su fiksirane prilagodbom na eksperimentalne podatke u svim dostupnim reakcijskim kanalima. Izračun kompletne amplitude je izbjegnut u mrežnoj aplikaciji, jer je za to potrebno mnogo vremena. Ulaz χMAID-a je ograničen do i uključujući $l = 4$ multipole (G valovi). Sve observable su izvedene iz multipola koji su prethodno izračunati za sve kanale reakcije. Izračun multipola provodi se za raspon energija $W = 1073.3 - 1190$ MeV i za elektroprodukciju kroz $Q^2 = 0.3$ (GeV/c)^2. Doprinosi petlji i njihovi parametri imaju fiksne vrijednosti i ne mogu se mijenjati putem mrežnog sučelja. Kontaktni dijagrami na $O(q^3)$ i $O(q^4)$ ulaze analitički, a pripadne niskoenergijske konstante mogu se mijenjati po volji. Više detalja o ovom modelu može se pročitati u [53].

Predviđanja teorijskih modela za T, L i TL članove udarnog presjeka elektroprodukcije nabijenog piona na protonu na $Q^2 = 0.078$ (GeV/c)^2 i $W = 1094$ MeV predstavljeni su u tablici 7.4. Ovdje je potrebno napomenuti da su rezultati χMAID modela dobiveni pomoću niskoenergijskih konstanti koje su prilagođene na rezultate prošlih eksperimenata elektroprodukcije nabijenih piona [53].

Zbog lakše usporedbe eksperimentalni T, L i TL članovi i pripadna teorijska predviđanja prikazani su na istom grafu 7.2. U slučaju T člana sva tri modela predviđaju nešto veće vrijednosti od eksperimentalne, DMT2001 i Maid2007 oko 10.7%, a χMAID oko 17.3%. Nadalje, u slučaju L člana predviđanja χMAID i DMT2001 su vrlo blizu eksperimentalne vrijednosti, dok Maid2007 predviđa nešto veću vrijednost. Kod TL člana, predviđanje DMT2001 nalazi se unutar raspona greške, MAID2007 je vrlo blizu raspona, dok je χMAID malo više izvan raspona greške.

8.5.2 Zaključak i perspektiva

Za pet različitih kinematika, izmjereni su udarni presjeci elektroprodukcije nabijenog piona na protonu. Invarijantna masa iznosila je $W = 1094$ MeV, a transfer četvero-impulsa $Q^2 = 0.078$ (GeV/c)^2. Raspršeni elektron detektiran je u spektrometru A u koincidenciji s proizvedenim nabijenim pionom, koji je detektiran u SOS-u. Po prvi puta napravljena je kompletna analiza podataka mjerenja elektroprodukcije nabijenih piona sa SOS-om. Analiza je uključivala uvođenje različitih korekcija specifičnih za SOS, kao i proširivanje mogućnosti programa Simul++ da može simulirati raspad piona u SOS-u. Ovisno o kinematici, statističke greške mjerenih udarnih presjeka bile su između 0.8% i 1.2%, a sistematske između 2.9% i 3.5%.

Rosenbluthovom metodom ukupni udarni presjek elektroprodukcije piona separiran je na longitudinalni i transverzalni udarni presjek, s ukupnim greškama od 14.7% i 6.7%. Također je određen i transverzalno-longitudinalni interferencijski udarni presjek, s ukupnom greškom od 10.5%. Eksperimentalne vrijednosti članova udarnog presjeka uspoređene su s predviđanjima izabranih teorijskih modela. Iako su korištene niskoenergijske konstante χMAID modela dobivene prilagodbom na prijašnje eksperimente elektroprodukcije piona [53], u slučaju longitudinalnog udarnog presjeka χMAID model daje dobro slaganje s eksperimentom. DMT2001 također daje dobro slaganje, dok Maid2007 daje oko 24.2% veću vrijednost. Sva tri modela predviđaju veće vrijednosti transverzalnog člana, ali ne više od 17.3%. Predviđanja modela MAID2007 i DMT2001 vrlo su blizu eksperimentalnoj vrijednosti transverzalno-longitudinalnog interferencijskog člana, s time da je predviđanje DMT2001 malo bolje. Ovdje, χMAID predviđa 22.5% veću vrijednost po iznosu.

Uvođenjem određenih poboljšanja u budućnosti, poprilično velike sistematske greške mogle bi se dodatno smanjiti. Jedno od mogućih poboljšanja bile bi nove transfer matrice koje bi bolje rekonstruirale nedisperzivne koordinate u odnosu na postojeće. Drugo poboljšanje bila bi izrada detaljne karte magnetskog polja SOS-ovog dipolnog magneta, koja obuhvaća i rubna polja. To bi omogućilo vjerniju simulaciju ponašanja čestica unutar SOS-a.

Nadalje, dobiveni transverzalni udarni presjek predstavlja podatak koji definira ponašanje aksijalnog form-faktora na niskom prijenosu četveroimpulsa ($Q^2 = 0.078$ $(\text{GeV}/\text{c})^2$). Kako SOS može detektirati pione s količinom gibanja mnogo nižom od 113 MeV/c, on nam pruža mogućnost, da u budućim eksperimentima istražimo ponašanje aksijalnog form-faktora na još nižim prijenosima četveroimpulsa.

Na pragu $p(e, e'\pi^+)n$ reakcije longitudinalni član udarnog presjeka ima dominantan doprinos od induciranog pseudoskalarnog form-faktora, koji se može izdvojiti iz eksperimentalne ovisnosti longitudinalnog člana o Q^2. Kako smo ovdje longitudinalni član odredili otprilike 15 MeV iznad praga reakcije, taj podatak bi se već mogao iskoristiti kao jedna od Q^2-točki za ekstrakciju induciranog pseudoskalaranog form-faktora.

Preciznije poznavanje slabih form-faktora omogućilo bi detaljniji opis slabe aksijalne struje nukleona. Elektromagnetski form-faktori, koji opisuju slabu vektorsku struju nukleona, poznati su s visokom preciznošću. Sve zajedno će doprinijeti boljem opisu elektroslabe strukture nukleona i svojstava koja slijede iz te strukture.

Bibliography

[1] T. de Forest Jr., J. D. Walecka, Adv. Phys. 15, 57 (1966)

[2] W. E. Kleppinger, J. D. Walecka, Ann. Phys. 146, 349-394 (1983)

[3] A. W. Thomas, W. Weise: The structure of the nucleon, Wiley-VCH Verlag Berlin 2001

[4] V. Bernard, L. Elouadrhiri, U.-G. Meißner, J. Phys. G 28, R1 (2002)

[5] E. Amaldi, S. Fubini, G. Furlan, Pion-electroproduction, Springer Tracts in Modern Physics 83, Springer Verlag, Berlin 1979

[6] D. Drechsel, L. Tiator, J. Phys. G: Nucl. Part. Phys. 18 (1992) 449.

[7] M. N. Rosenbluth, Phys. Rev. 79(4), 615-619 (1950)

[8] A. Richter, Trennung des longitudinalen, transversalen und longitudinal-transversal interferierenden Anteils des Wirkungsquerschnitts der Reaktion $H(e, e'\pi^+)$ in der Nähe der Pionschwelle, Dissertation, KPH, Universität Mainz, 1994

[9] K. I. Blomqvist et al. (A1 Collaboaration), Z. Phys. A 353 (1996) 415.

[10] S. Širca, The axial form factor of the nucleon from coincident pion electroproduction at low Q^2, Dissertation, Univ. of Ljubljana, 1999

[11] A. Liesenfeld et al., Phys. Lett. B 468 (1999) 20.

[12] D. Baumann, π^+-Elektroproduktion an der Schwelle, Dissertation, KPH, Universität Mainz, 2005

[13] J. Beringer et al., (Particle Data Group) (2012)

[14] D. Baumann, Entwurf eines Spetrometer kurzer Banlänge zum Nachweis niederenergetischer Pionen, Diplomarbeit, Institut für Kernphysik, Univ. of Mainz, 1997

[15] M. Ding, Entwicklung einer Fokalebenen-Driftkammer für niederenergetische Pionen, Diplomarbeit, Institut für Kernphysik, Univ. of Mainz, 1997

[16] M. Ding, Entwicklung einer Fokalebenen-Driftkammer für niederenergetische Pionen und experimentelle Bestimmung einer inversen Transfermatrix für das Short-Orbit-Spektrometer, Dissertation, Institut für Kernphysik, Univ. of Mainz, 2004

[17] T. Fuchs, Formfaktoren des Nukleons in relativistischer chiraler Störungstheorie. Dissertation, KPH, Universität Mainz, 2002.

[18] T. Ericson, W. Weise, Pions and Nuclei. Clarendon Press, Oxford, 1988

[19] F. Close, S. Donnachie, G. Shaw, Electromagnetic interactions and hadronic strucuture, Cambridge University Press 2007

[20] D. Drechsel, http://arxiv.org/abs/nucl-th/0003061

[21] S. Choi et al. Phys. Rev. Lett. 71 (1993) 3927.

[22] M. L. Goldberger und S. B. Treiman, Phys. Rev. 111 (1958) 354.

[23] T. E. O. Ericson, B. Loiseau and A. W. Thomas, Phys. Rev. C 66 (2002) 014005

[24] T. Fuchs and S. Scherer, Phys. Rev. C 68 (2003) 055501

[25] C. Juszczak, et al., Phys. Rev. C 82, 045502 (2010)

[26] G. P. Zeller, 2008 J. Phys.: Conf. Ser. 136 022028

[27] R. Gran, E.J. Jeon et al [K2K collaboration], Phys. Rev. D 74 (2006) 052002.

[28] X. Espinal and F. Sanchez, AIP Conf. Proc. 967 (2007) 117.

[29] M. Dorman [MINOS collaboration], AIP Conf. Proc. 1189 (2009) 133.

[30] A.A. Aguilar-Arevalo [MiniBooNE collaboration], Phys. Rev. D81 (2010) 092005.

[31] V. Lyubushkin [NOMAD collaboration], AIP Conf. Proc. 1189 (2009) 157.

[32] K. H. Kaiser et al., Nucl. Inst. and Meth. A 593, 159 (2008)

[33] K. H. Kaiser et al., Eur. Phys. J. Special Topics 198, 19–47 (2011)

[34] K. I. Blomqvist et al., The three-spectrometer facility at the Mainz microtron MAMI, Nucl. Instr. Meth. A 403 (1998) 263.

[35] M. Korn, Entwicklung des Bahnrückverfolgungsverfahrens für die Drei-Spektrometer-Anlage und experimentelle Bestimmung der Abbildungseigenschaften der Spektrometer A und B mit elastischer Elektronenstreuun,Dissertation, KPH, Universität Mainz, 1994

[36] J. C. Bernauer, Measurement of the elastic electron-proton cross section and separation of the electric and magnetic form factor in the Q^2 range from 0.004 to 1 $(GeV/c)^2$, Dissertation, Univ. of Mainz, 2010

[37] M. O. Distler, Aufbau und Test einer vertikalen Driftkammer, Diplom thesis, Institut für Kernphysik, Univ. of Mainz, 1990

[38] P. Merle, Entwicklung des programmierbaren koinzidenztriggersystems und messung von A_Y^0 in der reaktion $^3\overrightarrow{He}(e, e'n)$, Dissertation, Institut für Kernphysik, Univ. of Mainz, 2002

[39] C. P. Browne, W. W. Buechner, Rev. Sci. Inst. 27 (1956) 899

[40] http://wwwa1.kph.uni-mainz.de/A1/publications/proposals/piplus1-98.ps.gz

[41] W. R. Leo, Techniques for nuclear and particle physics experiments, Springer-Veralg, Berlin Heidelberg 1987

[42] M. O. Distler, H. Merkel, M. Weis, Proceedings of the 12th IEEE Real Time Congress on Nuclear and Plasma Sciences, Valencia, June 2001

[43] NIST Scientific and Technical Databases, Chemistry WebBook, NIST Standard Reference Database Number 69 - March, 2003 Release, Thermophysical Properties of Fluid Systems, http://webbook.nist.gov/chemistry/fluid/

[44] I. Ewald, Kohärente Elektroproduktion von neutralen Pionen am Deuteron nahe der Schwelle, Dissertation, Institut für Kernphysik, Univ. of Mainz, 2000

[45] A. P. Liesenfeld, Konstruktionsunterlagen zu den Čerenkov-Detektoren, Institut für Kernphysik , Univ. of Mainz

[46] M. Mihovilovič, Sledenje nestablinih delcev v magnetnih spektrometrih, Dipolmsko delo, Ljubljana 2007

[47] http://wwwkph.kph.uni-mainz.de/MAID//maid.html

[48] S. S. Kamalov, G.-Y. Chen, S. N. Yang, D. Drechsel, L. Tiator, Phys. Lett. B 522, 27-36 (2001)

[49] S. S. Kamalov, S. N. Yang, D. Drechsel, L. Tiator, Phys. Rev C 64, 032201(R)

[50] S. S. Kamalov and S. N. Yang, Phys. Rev. Lett. 83, 22 (1999)

[51] D. Drechsel, S. S. Kamalov, L. Tiator, Eur. Phys. J. A 34, 69–97 (2007)

[52] J.J. Kelly et al., Phys. Rev. Lett. 95, 102001 (2005); Phys. Rev. C 75, 025201 (2007)

[53] M. Hilt, B. C. Lehnhart, S. Scherer, L. Tiator, http::/arxiv.org/abs/1309.3385v1

Životopis

Ivica Friščić je rođen 08. veljače 1985. godine u Varaždinu. Do 1999. godine pohađa osnovnu školu Ivana Kukuljevića Sakcinskog u Ivancu, a do 2003. godine Srednju školu Ivanec, smjer opća gimnazija. Iste godine upisuje diplomski studij diplomiranog inženjera fizike na Prirodoslovno-matematičkom fakultetu Sveučilišta u Zagrebu. Zajedno sa kolegom Milivojem Plodincem, dobitnik je rektorove nagrade 2007. godine za studentski rad iz fizike, koji je izrađen pod mentorstvom dr. sc. Andreje Gajović u Zavodu za fiziku materijala na Institutu Ruđer Bošković. Diplomirao je 2008. godine sa temom: "Izgradnja modela pozitronskog emisijskog tomografa", pod mentorstvom prof. dr. sc. Damira Bosnara sa Fizičkog odsjeka Prirodoslovno-matematičkog fakulteta u Zagrebu. Od 2009. godine zaposlen je kao asistent – znanstveni novak na Fizičkom odsjeku Prirodoslovno-matematičkog fakulteta u Zagrebu. Iste godine upisuje poslijediplomski doktorski studij nuklearne fizike. Tri puta je dobio jednomjesečnu stipendiju za znanstveno usavršavanje Međunarodne agencije za atomsku energiju (IAEA): 2009. na Fizičkom odsjeku, Fakulteta znanosti, Sveučilišta u Coimbri, Portugal; 2011. na Fizičkom fakultetu, Sveučilišta St. Kliment Ohridski, Sofija, Bugarska i 2014. na Nacionalnom laboratoriju u Frascati-u, Nacionalni institut za nuklearnu fiziku (INFN), Italija. Od 2009. član je A1 kolaboracije Instituta za nuklearnu fiziku Johannes Gutenberg Sveučilišta u Mainzu (Njemačka), gdje sudjeluje na eksperimentima s elektronskim ubrzivačem MAMI.

Popis CC radova:

1. Achenbach, P.; Ayerbe Gayoso, C.; Böhm, R.; Borodina, O.; Bosnar, D.; Bozkurt, V.; Debenjak, L.; Distler, M. O.; Esser, A.; Friščić Ivica; Fujii, Y.; Gogami, T.; Gómez Rodríguez, M.; Hashimoto, O.; Hirose, S.; Kanda, H.; Kaneta, M.; Kim, E.; Kusaka, J.; Margaryan, A.; Merkel, H.; Müller, U.; Nagao, S.; Nakamura, S. N.; Pochodzalla, J.; Rappold, C.; Reinhold, J.; Saito, T. R.; Sanchez Lorente, A.; Sánchez Majos, S.; Schlimme, B.S.; Schoth, M.; Schulz, F.; Sfienti, C.; Širca, S; Tang, L.; Thiel, M.; Tsukada, K.; "Recent Studies of Hypernuclei Formation with Electron Beams at MAMI", Few-body systems 55 (2014) , 8-10; 887-892

2. Merkel, H.; Achenbach, P.; Ayerbe Gayoso, C.; Beranek, T.; Beričič, J.; Bernauer, J. C.; Böhm, R.; Bosnar, D.; Correa, L.; Debenjak, L.; Denig, A.; Distler, M. O.; Esser, A.; Fonvieille, H.; Friščić, Ivica; Gómez Rodríguez de la Paz, M.; Hoek, M.; Kegel, S.; Kohl, Y.; Middleton, D. G.; Mihovilovič, M.; Müller, U.; Nungesser, L.;

Pochodzalla, J.; Rohrbeck, M.; Ron, G.; Sánchez Majos, S.; Schlimme, B. S.; Schoth, M.; Schulz, F.; Sfienti, C.; Širca, S; Thiel, M.; Tyukin, A.; Weber, A.; Weinriefer, M.; "Search at the Mainz Microtron for Light Massive Gauge Bosons Relevant for the Muon g - 2 Anomaly", Physical Review Letters. 112 (2014), 22; 221802-1-221802-5

3. Achenbach, P.; Gómez Rodríguez, M.; Tsukada, K.; Ayerbe Gayoso, C.; Böhm, R.; Borodina, O.; Bosnar, D.; Bozkurt, V.; Bydžovský, P.; Debenjak, L.; Distler, M.O.; Esser, A.; Friščić Ivica; Fujii, Y.; Gogami, T.; Hashimoto, O.; Hirose, S.; Kanda, H.; Kaneta, M.; Kim, E.; Margaryan, A.; Merkel, H.; Müller, U.; Nagao, S.; Nakamura, S.N.; Pochodzalla, J.; Rappold, C.; Reinhold, J.; Saito, T.R.; Sanchez Lorente, A.; Sánchez Majos, S.; Schlimme, B.S.; Schoth, M.; Sfienti, C.; Širca, S.; Tang, L.; Thiel, M.; "Overview of the electromagnetic production of strange mesons at MAMI", Nuclear Physics A. 914 (2013); 41-50

4. Esser, A.; Nagao, S.; Schulz, F.; Bleser, S.; Steinen, M.; Achenbach, P.; Ayerbe Gayoso, C.; Böhm, R.; Borodina, O.; Bosnar, D.; Botvina, A.; Bozkurt, V.; Debenjak, L.; Distler, M.O.; Friščić Ivica; Fujii, Y.; Gogami, T.; Gómez Rodríguez, M.; Hashimoto, O.; Hirose, S.; Kanda, H.; Kaneta, M.; Kim, E.; Kohl, Y.; Kusaka, J.; Margaryan, A.; Merkel, H.; Mihovilovič, M.; Müller, U.; Nakamura, S.N.; Pochodzalla, J.; Rappold, C.; Reinhold, J.; Saito, T.R.; Sanchez Lorente, A.; Sánchez Majos, S.; Schlimme, B.S.; Schoth, M.; Sfienti, C.; Širca, S.; Tang, L.; Thiel, M.; Tsukada, K.; Weber, A.; Yoshida, K.; "Prospects for hypernuclear physics at Mainz: From KAOS@MAMI to PANDA@FAIR", Nuclear Physics A. 914 (2013); 519-529

5. Tsukada, K; Achenbach, P.; Ayerbe Gayoso C.; Böhm, R.; Borodina, O.; Bosnar, D.; Bozkurt V.; Debenjak, L.; Distler M.; Esser D.; Friščić Ivica; Fujii, Y.; Gogami T.; Gomez M.; Hashimoto O.; Hirose, S.; Kim E.; Margaryan A.; Merkel H.; Müller, U.; Nagao, S.; Nakamura S.N.; Pochodzalla, J.; Rappold, C.; Reinhold J.; Sanchez Lorente, A.; Saito, T.; Schlimme, B.S.; Schoth, M.; Schulz, F.; Sfienti, C.; Širca, S.; Tang, L.; "Decay Pion Spectroscopy of Electro-Produced Hypernuclei", Few-body systems. 54 (2013); 375-379

6. Achenbach, P.; Esser, A.; Ayerbe Gayoso, C.; Böhm, R.; Borodina, O.; Bosnar, D.; Bozkurt, V.; Bydžovský, P.; Debenjak, L.; Distler, M.O.; Friščić Ivica; Fujii, Y.; Gogami, T.; Gómez Rodríguez, M.; Hashimoto, O.; Hirose, S.; Kim, E.; Margaryan, A.; Merkel, H.; Müller, U.; Nagao, S.; Nakamura, S.N.; Pochodzalla, J.; Rappold, C.; Reinhold, J.; Saitoa, T.R.; Sanchez Lorente, A.; Sánchez Majos, S.; Schlimme, B.S.; Schoth, M.; Schulz, M.; Sfienti, C.; Širca, S.; Tang, L.; Thiel, M.; Tsukada, K.; "Strange hadronic physics in electroproduction experiments at the Mainz Microtron", Nuclear physics. A. 881 (2012); 187-198

7. Makek, M.; Achenbach, P.; Ayerbe Gayosoa, C.; Baumann, D.; Bernauer, J.C.; Bohm, R.; Bosnar, D.; Deniga, A.; Ding, M.; Distlera, M.O.; Doria, L.; Friedrich, J.; Friščić Ivica; Gomez, M.; Merkela, H.; Muller, U.; Nungesser, L.; Pochodzallaa, J.; Potokar, M.; Seimetz, M.; Sanchez Majosa, S.; Schlimme, B.S.; Sirca, S.; Walcher, th.; Weinriefer M.; "Silicon Detector Telescope for Proton Detection in Electron Scattering Reactions at MAMI", Nuclear instruments and methods in physics research section A., 673 (2012); 82-88

8. Achenbach, P.; Ayerbe Gayoso, C.; Bernauer, J.C.; Bianchin, S.; Bohm, R.; Borodina, O.; Bosnar, D.; Bosz, M.; Bozkurt, V.; Bydsovsky, P.; Debenjak, L.; Distler, M.O.; Esser, A.; Friščić Ivica; , Gomez Rodriguez, M.; Gokuzum, B.; Griessinger, K.; Jennewein, P.; Kim, E.; Makek, M.; Merkel, H.; Minami, S.; Muller, U.; Nakajima, D.; Nungesser, L.; Ozel-Tashenov, B.; Pochodzalla, J.; Rappold, Ch.; Saito, T.R.; Sanchez Majos, S.; Schlimme, B.S.; Sirca, S.; Weinriefer, M.; Yoon, C.J.; "Exclusive electroproduction of K+ Lambda and K+ Sigma(0) final states at Q(2) = 0.030-0.055 (GeV/c)(2)"; European physical journal A: hadrons and nuclei, 14 (2012); 14-28

9. Achenbach P., Ayerbe Gayoso, C.; Bernauer, J.C.; Bohm, R.; Bosnar, D.; Bosz, M.; Debenjak, L.; Distler, M.O.; Esser, A.; Friščić Ivica; , Gomez Rodrıguez dela Paz, M.; Makek, M.; Merkel, H.; Muller, U.; Nungesser, L.; Pochodzalla, J.; Potokar, M.; Sanchez Majos, S.; Schlimme, B.S.; Širca, S.; Weinriefer M.; "Particle tracking in kaon electroproduction with cathode-charge sampling in multi-wire proportional chambers", Nuclear Instruments and Methods in Physics Research A. 641 (2011); 105-113

10. Achenbach, P.; Gayoso, C.A.; Bernauer, J.C.; Bohm, R.; Bosnar, D.; Debenjak, L.; Distler, M.O.; Esser, A.; Friščić Ivica; Gomez Rodriguez de la Paz, M.; Hoffmann, J.; Makek, M.; Merkel, H.; Minami, S.; Muller, U.; Nungesser, L.; Ott, W.; Pochodzalla, J.; Potokar, M.; Rusanov, I.; Saito, T.R.; Sanchez Majos, S.; Schlimme, B.S.; Sirca, S.; Voltz, S.; Weindel, K.; Weinriefer, M.; "A Large-Scale FPGA-Based Trigger and Dead-Time Free DAQ System for the Kaos Spectrometer at MAMI", IEEE transactions on nuclear science. 58 (2011), 4; 1677-1684

11. Merkel, H.; Achenbach, P.; Ayerbe Gayoso, C.; Bernauer, J.C.; Bohm, R.; Bosnar, D.; Debenjak, L.; Denig, A.; Distler, M.O.; Esser, A.; Fonvieille, H.; Friščić Ivica; Middleton, D.G.; Muller, U.; Nungesser, L.; Pochodzalla, J.; Rohrbeck, M.; Sánchez Majos, S.; Schlimme, B.S.; Schoth, M.; Sirca, S.; Weinriefer M.; "Search for Light Gauge Bosons of the Dark Sector at the Mainz Microtron", Physical Review Letters 106 (2011); 251802-1-251802-4

12. Achenbach P.; Ayerbe Gayosoa, C.; Bernauera, J.C.; Bianchin, S.; Bohm, R.; Boro-

din, O.; Bosnar, Damir; Bozkurt, V.; Debenjak, L.; Denig, A.; Distler, M.O.; Esser, A.; Fonvieillee, H.; Friščić, Ivica; Gokuzumb, B.; Grießinger, K.; Kim, E.; Maas, F.E.; Makek, Mihael; Merkel, H.; Minami, S.; Muller, U.; Nakajima, D.; Nungesser, L.; Ozeltashenov, B.; Pochodzalla, J.; Potokar, M.; Rappold, Ch.; Saito, T.R.; Sánchez Majos, S.; Schlimme, B.S.; Sirca, S.; Weinriefer, M.; "First measurements of Λ and Σ^0 hyperons in elementary electroproduction at MAMI", Nuclear physics A, 835 (2010) , 1; 313-316

13. Plodinec, M.; Friščić Ivica; Iveković, D.; Tomašić, N.; Su, D.; Zhang, J.; Gajović, A.; "Mechanochemical stability of hydrogen titanate nanostructures", Journal of alloys and compounds, 499 (2010), 1; 113-120

14. Gajović, A.; Friščić Ivica; Plodinec, M.; Iveković, D., "High temperature Raman spectroscopy of titanate nanotubes", Journal of molecular structure, 924/926 (2009); 183-191